Development of a 3-D upper crustal velocity model for the Goldstream Valley, central Alaska

Author: Sara L. Dougherty

Boston College

The Graduate School of Arts of Sciences

Department of Geology and Geophysics

DEVELOPMENT OF A 3-D UPPER CRUSTAL VELOCITY MODEL OF THE GOLDSTREAM VALLEY, CENTRAL ALASKA

a thesis

by

SARA L. DOUGHERTY

submitted in partial fulfillment of the requirements

for the degree of

Master of Science

August 2008

Development of a 3-D upper crustal velocity model for the Goldstream Valley, central Alaska

Sara L. Dougherty with John E. Ebel

The uppermost crustal velocity structure of the Goldstream Valley, central Alaska is investigated using a series of five explosions that were detonated in schist bedrock and recorded at >120 local stations to develop 1-D and 3-D models of the upper crust. Simple refraction analyses reveal that both P- and S-wave arrival times are azimuth dependent, with the fastest velocities in the southeast and northeast directions. The S-wave velocity structure of the upper crust is also determined through multiple filter analysis and a damped, least squares inversion of 0.2-2 sec period Rg waves. The shear wave velocity model from the surface-wave analysis is combined with the refraction analysis results to develop 1-D P- and S-wave models to a depth of 2 km. In order to better constrain P- and S-wave velocity variations both laterally and with depth throughout the Goldstream Valley, 3-D velocity models are produced using a numerical simulation model.

Table of Contents

List of Figures

List of Tables

Acknowledgements

Foremost, I would like to thank my thesis advisor, Dr. John Ebel, for his continued support, guidance, and thoughtful insight throughout this endeavor. Thanks to Dr. Alan Kafka for his critical review of this thesis. I would also like to thank Dr. Geoffrey Abers for introducing me to James Lewkowicz, the president of Weston Geophysical Corporation (WGC), who afforded me the invaluable opportunity to gain seismic data processing experience under his employ. This thesis would not have been possible without the valuable seismic data provided to me by WGC and my continued collaboration with the WGC staff, especially Dr. Jessie Bonner and Mark Leidig. I am grateful to Dr. Jessie Bonner for all of the insightful comments, data processing support, and careful interpretations he shared with me throughout the research, analysis, and writing phases of this thesis. I am also thankful for Mark Leidig's assistance in executing the 3-D numerical simulation code, without which my 3-D velocity models would not have been possible.

I am eternally grateful for the constant support and encouragement that I received from my family and friends throughout the time that I worked on this thesis. I would especially like to thank Walter Stelz for his continued emotional support and companionship.

The Frozen Rock Experiment conducted by WGC was funded by the Air Force Research Laboratory under contract no. FA8718-04-C-0026.

I. Introduction

The interior structure of the Earth can be determined from the analysis of seismic waves and is often characterized in terms of variations in P- and S-wave velocities. In order to obtain the most accurate image of Earth structure, including both lateral and depth variations in seismic velocities, a high density spatial distribution of sources and receivers is needed. This study utilizes such a high density data set from central Alaska where six explosive shots were recorded by more than one hundred sensors distributed across the study area. The data from five of these explosions are analyzed to determine the 3-D upper crustal structure of the region.

Weston Geophysical Corporation (WGC) and the University of Alaska, Fairbanks (UAF) conducted the Frozen Rock Experiment (FRE) in the Goldstream Valley of central Alaska in August 2006. The objective of this experiment was to characterize the differences in ground motion scaling and coupling for explosions in frozen versus unfrozen rocks in order to quantify variations in estimated seismic yield of explosions in frozen rock (*Leidig et al.,* 2006a). Laboratory experiments have shown that frozen rock is significantly stronger than unfrozen rock, and it is thought that this increased strength can alter the seismically estimated yield by varying the seismic coupling (*Leidig et al.,* 2006b; *Sammis and Biegel*, 2005). Increased strength could result in reduced seismic amplitudes in the far-field for explosions in frozen rock, possibly leading to an underestimated seismic yield (*Leidig et al.,* 2006b; *Sammis and Biegel*, 2005). The accurate estimation of seismic yield is especially important in determining the size and location (e.g., depth) of nuclear explosions.

The FRE was conducted in a region of discontinuous permafrost ~20 km north of Fairbanks, AK near Polar Mining Incorporated's (PMI) gold mine in Fox, AK. A series of six small explosions were detonated in boreholes and recorded on >120 local sensors consisting of broadband (Figure 1a), "Texan" (Figure 1b), and near source (Figure 1c) instruments. The "Texan" instruments use 4.5 Hz geophones and were designed by the University of Texas at El Paso. Three of the explosions were detonated in frozen rock (shots 1-3) and three were detonated in unfrozen rock (shots 4-6). Note that shots 1 and 2 were co-located, as were shots 4-6 (Figure 1). The frozen rock test sites were located in the working pit of the PMI placer gold mine, while the unfrozen rock test site was located on a south-facing hill 1.1 km north of the frozen test sites. Shot 6 was a small, 100 lb explosion that did not have adequate signal-to-noise ratio and was not used to develop velocity models.

In their determination of an initial refraction velocity model for the crust from data recorded on Texan instruments, *Leidig et al.* (2006a) observed that the stations in each geographic region yielded a different P-wave velocity, indicating large lateral variations in the velocity structure and/or anisotropy. Thus, *Leidig et al.* (2006a) analyzed the Texan data in four groups consisting of the northwest (NW), southeast (SE), northeast (NE), and north (N) stations (see Figure 1b for the definition of these regions). Based on their compilation of the velocities determined for the specific areas covered by each of these station groups, *Leidig et al.* (2006a) proposed that it should be possible to develop a 3-D velocity model of the study area.

Preliminary investigation of the FRE seismic data by WGC suggests that the velocity model for the Goldstream Valley has large lateral variations in the velocity structure and/or anisotropy that cause the preliminary 1-D velocity model developed in the explosion test region to predict a later arrival for the surface waves than was observed at some stations (*Leidig et al.,* 2007). In order to better illustrate the variations in P- and S-wave velocity both laterally and with depth throughout the Goldstream Valley, a detailed 3-D upper crustal velocity model of the region is developed in this study using the well-located explosions and numerical simulations.

This study examines seismic data recorded by WGC and UAF in the Goldstream Valley region of central Alaska during the FRE in order to develop a 3-D seismic velocity model of the upper crust in this area. Initially, a 1-D velocity model is developed through a refraction analysis of P- and S-wave arrival times. Anisotropy is explored as a possible explanation for the large lateral variations in seismic velocity, while the time-term method is employed to better understand the velocity and thickness of the uppermost crustal seismic layer beneath each station. The upper crustal structure imaged by the P- and S-waves is also analyzed in terms of Poisson's ratios. In order to obtain a complete picture of the velocity structure with depth in the upper crust, Rg dispersion curves are generated using the multiple filter analysis technique (*Dziewonski et al.*, 1969), and then inverted for shear wave velocity. A complete 3-D velocity model is then produced using the Wave Propagation Program developed by *Appelö et al.* (2007).

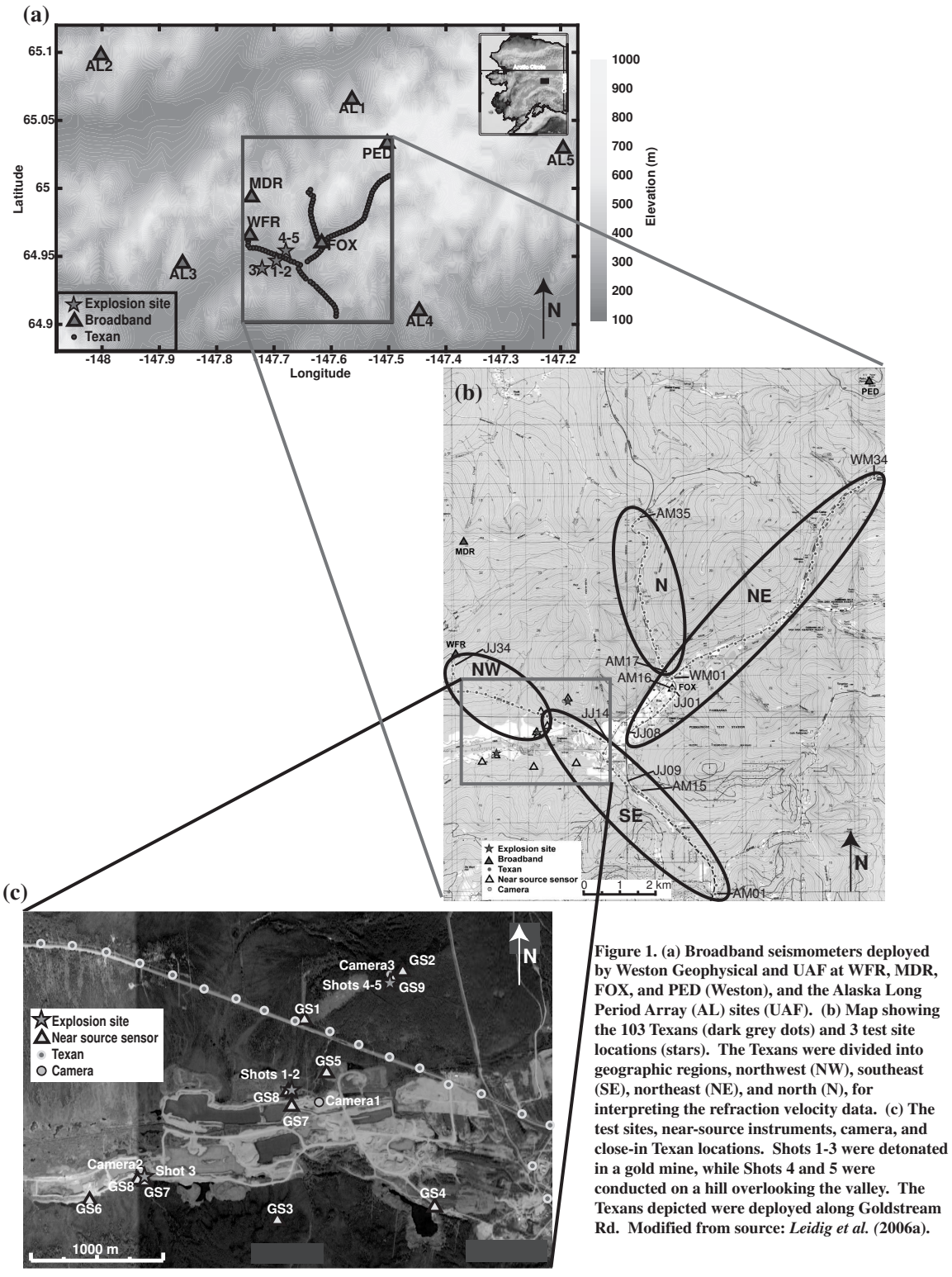

Figure 1. (a) Broadband seismometers deployed by Weston Geophysical and UAF at WFR, MDR, FOX, and PED (Weston), and the Alaska Long Period Array (AL) sites (UAF). (b) Map showing the 103 Texans (dark grey dots) and 3 test site locations (stars). The Texans were divided into geographic regions, northwest (NW), southeast (SE), northeast (NE), and north (N), for interpreting the refraction velocity data. (c) The test sites, near-source instruments, camera, and close-in Texan locations. Shots 1-3 were detonated in a gold mine, while Shots 4 and 5 were conducted on a hill overlooking the valley. The Texans depicted were deployed along Goldstream Rd. Modified from source: *Leidig et al.* (2006a).

.

II. Geologic Setting

The Goldstream Valley is part of the lucrative Fairbanks Mining District, which has undergone extensive placer mining since the first discovery of gold there in 1902 (*Robinson et al.,* 1990). This region is located within the northwestern Yukon-Tanana Upland, a metamorphic terrane of continental origins bounded on the northeast and southwest by the Tintina and Denali dextral strike-slip faults, respectively (Figure 2a). The Yukon-Tanana is transected by several northeast trending high angle faults (Figure 2b), many of which show left-lateral offsets and appear to be dislocations related to a shear couple between the locked or slow-moving Tintina fault and the more active Denali fault (*Newberry et al.,* 1996; *Robinson et al.,* 1990). The regional structural evolution of the terrane is dominated by at least two major episodes of folding. The first episode resulted in synmetamorphic, overturned to recumbent, subisoclinal, northeast-verging folds with wavelengths up to 300 m and northwest-trending axes (*Robinson et al.,* 1990). The second episode folded the previously metamorphosed rock units into a series of broad northeast-trending open folds (*Foster et al.*, 1994; *Robinson et al.,* 1990). Locally, structures include small-scale folds, faults, joints, and shear zones (*Robinson et al.,* 1990).

The dominant rock unit of the Yukon-Tanana Upland is the metasedimentary Fairbanks schist unit (*Foster et al.,* 1994; *Robinson et al.,* 1990). The Goldstream Valley, in which the town of Fox is located, is contained within this greenschist to amphibolite facies metamorphic grade rock unit, which is comprised mainly of interlensing pelitic schist, mica-quartz schist, micaceous quartzite, and large gneiss dome

complexes (*Foster et al.,* 1994; *Robinson et al.,* 1990; *Wilson et al.,* 1998). The Paleozoic to Pre-Cambrian quartz-pelitic schist dominates the higher elevations surrounding the valley, while the valley itself is covered by Quaternary surficial deposits of unconsolidated sand and gravel overlain by glacial loess (Figure 2b; *Foster et al.,* 1994; *Wilson et al.,* 1998). Figure 2b shows the locations of the Texan stations and all five explosive shots of the FRE, four of which were detonated within metamorphic bedrock (shots 1, 2, 4, and 5) and one of which was detonated in frozen Quaternary gravels (shot 3). *Bonner and Leidig* (2007) and *Bonner et al.* (2007) note that a metamorphic facies change occurs between the frozen (shots 1-3) and unfrozen (shots 4-5) test sites from gneiss and schist in the valley (not depicted here) to pelitic schist on the hill top.

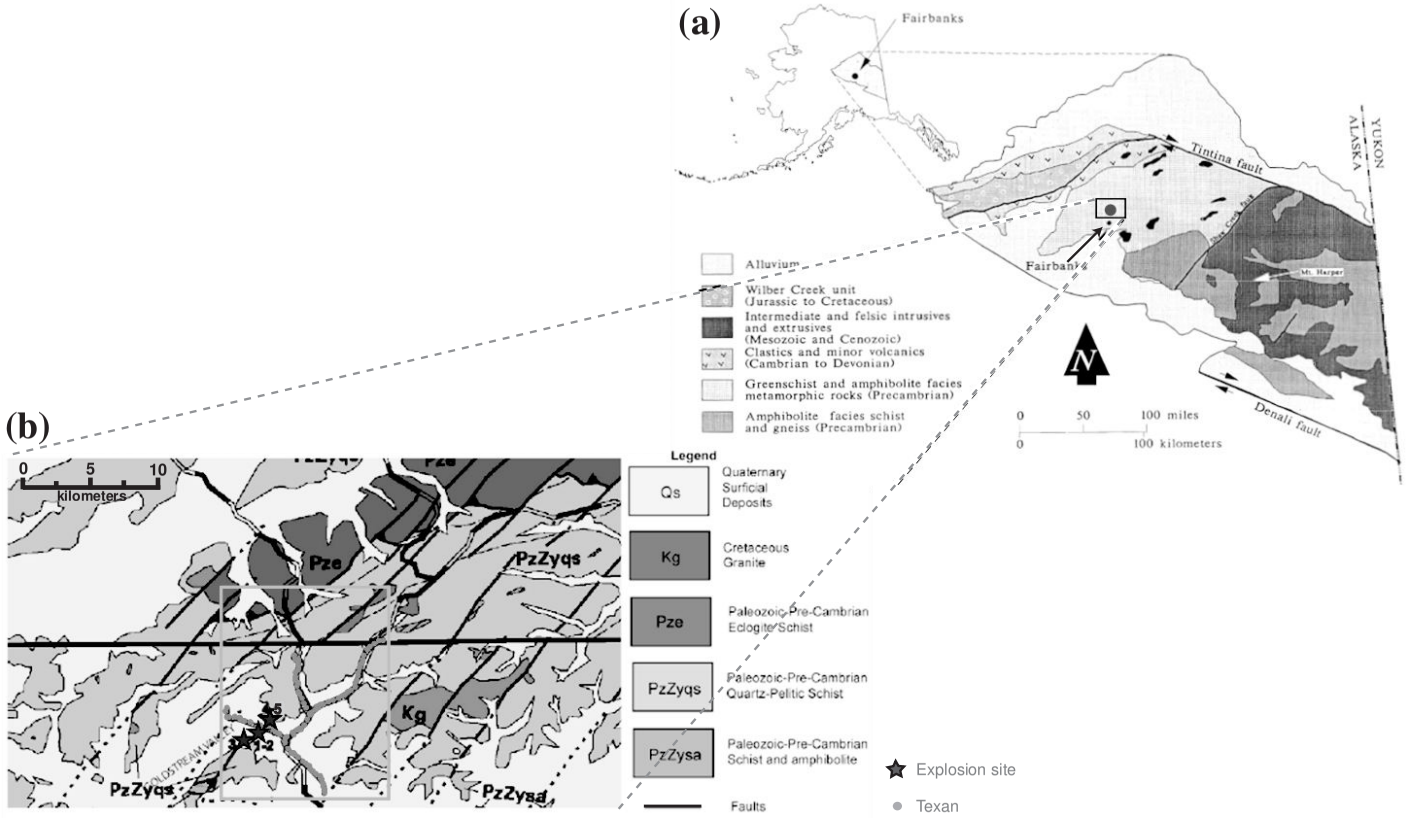

Figure 2. (a) Regional geologic map of the Yukon-Tanana Upland. The approximate location of the town of Fox is indicated by the black dot. Modified from *Robinson et al.* (1990). (b) Geologic map of the Goldstream Valley region of central Alaska showing northeast-trending faults. The locations of the FRE shots (black stars) and Texan stations (gray dots) are also shown. The stations were located in either Quaternary surficial deposits or Paleozoic/Pre-Cambrian quartz-pelitic schist. The gray box outlines the boundary of Figure 1b. Figure modified from *Bonner and Leidig* (2007). Original map source: *Wilson et al.* (1998).

III. Refraction Analysis

The arrival times of the P-wave at each of the broadband, near-source, and Texan stations for each of the five shots are manually identified using the Seismic Analysis Code (SAC) software package (*Goldstein et al.,* 2003). Arrival times are not picked on waveforms lacking a clear arrival onset. The S-waves are only picked for Texan stations located at distances ≥ 2 km from the source. At shorter distances, discernment of the S-wave is difficult since the S-wave arrives at the station immediately after the P-wave, with no clear distinction between the two waves, so no picks are made for close-in Texans or the near source instruments. Due to the small number of broadband instruments (9) that were deployed over a large range of source-receiver distances (3 km – 22 km), any velocities determined using the data from these stations alone cannot be well constrained, and so broadband data are not used for the development of the 1-D velocity models in this study. Future velocity analyses could combine data from broadband stations located within a distance of 13 km from the source (maximum Texan source-receiver distance) with the Texan data to further constrain velocities in both S- and P-wave models.

In order to correct for the surface topography in the Goldstream Valley, a simple elevation statics correction is applied to all the receiver times at the Texan and near-source stations used in the travel time analyses. This static correction adjusts the elevation of all of the receivers in a particular shot group (i.e. shots 1 & 2, shot 3, or shots 4 & 5) to a common reference datum, which in this study is selected to correspond with the elevation of the middle of the explosive column for the lowest elevation shot in the

group. For example, in the case of the shots 1 & 2 group, the middle of the explosive column is at an elevation of 196 m for shot 1 and 184 m for shot 2. Thus, all of the shots 1 & 2 recordings are corrected to a datum of 184 m (the shallowest shot point). The time correction, ΔT, is then determined from the following equation:

$$\Delta T = \frac{E_S - E_D}{V} \qquad (1)$$

where E_S is the elevation of the receiver station, E_D is the elevation of the datum, and V is the velocity of the direct wave as determined from the uncorrected data. To obtain the corrected travel time of the P- and S-waves at each station, the corresponding ΔT is subtracted from the original travel time.

The statically corrected P- and S-wave arrival picks are plotted on several distance vs. travel time plots in order to observe any changes in velocity indicated by a varying slope of data points. Least squares trendlines are fit to the data in these different plots in an effort to generate starting P- and S-wave velocity models for the study area. The broadband data are not included in these analyses due to an insufficient number of data points to constrain any trendline slopes at stations ≥ 13 km from the source.

Simple refraction analyses reveal that both P- and S-wave arrival times are azimuth dependent, with the fastest velocities seen in the southeast (SE) and northeast (NE) for both P- and S-waves (Figure 3). The resultant two layer over a half-space velocity models for each region and shot group are shown in Table 1. Recalling that S-wave arrivals could only be selected for stations located at distances ≥ 2 km from the source, the S-wave velocity (β) of only the half-space (taken to be layer 3) was modeled in the refraction analysis. For some cases (e.g. shots 1 & 2 N), a two layer over a half-

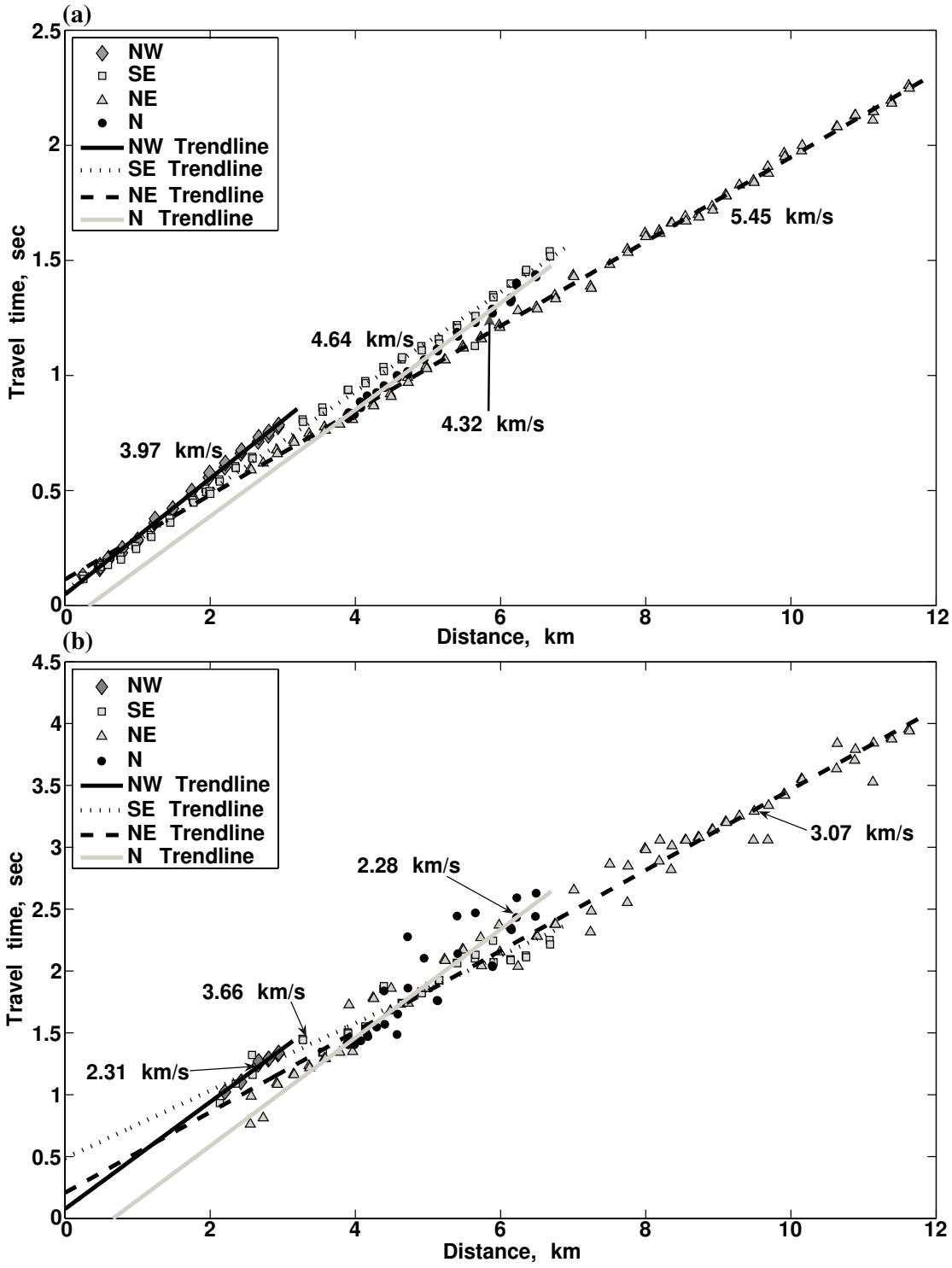

Figure 3. Uncorrected Texan travel time plots using shots 1 & 2 data. (a) P-wave travel times for all four regions with velocities for each region indicated. (b) S-wave travel times for all regions. For both wave types, the fastest velocities in these plots are seen in the SE and NE regions.

Table 1. Three Layer Velocity Models from Refraction Analysis

Shots 1 & 2

Layer	NW			SE			NE			N		
	Depth to Top, km	α, km/s	β, km/s	Depth to Top, km	α, km/s	β, km/s	Depth to Top, km	α, km/s	β, km/s	Depth to Top, km	α, km/s	β, km/s
1	0	2.92	--	0	2.92	--	0	3.09	--	0	--	--
2	0.06	3.98	--	0.04	4.03	--	0.05	3.76	--	--	--	--
3	0.4	5.01	2.54	0.3	4.91	3.77	0.3	5.57	3.11	--	--	2.44

Shot 3

Layer	NW			SE			NE			N		
	Depth to Top, km	α, km/s	β, km/s	Depth to Top, km	α, km/s	β, km/s	Depth to Top, km	α, km/s	β, km/s	Depth to Top, km	α, km/s	β, km/s
1	0	2.75	--	0	--	--	0	--	--	0	--	--
2	0.06	3.81	--	--	--	--	--	--	--	--	--	--
3	0.4	5.08	2.19	--	--	2.54	--	--	3.28	--	--	2.55

Shots 4 & 5

Layer	NW			SE			NE			N		
	Depth to Top, km	α, km/s	β, km/s	Depth to Top, km	α, km/s	β, km/s	Depth to Top, km	α, km/s	β, km/s	Depth to Top, km	α, km/s	β, km/s
1	0	--	--	0	3.31	--	0	3.17	--	0	3.18	--
2	--	--	--	0.2	4.19	--	0.07	3.68	--	0.1	3.86	--
3	--	--	2.67	0.5	5.22	2.77	0.3	5.51	2.98	0.3	4.55	2.31

space P-wave velocity (α) model could not be discerned from the data, so there are no depth or α values indicated in Table 1 for those cases. Overall, these refraction results provide velocity models of the uppermost crust to depths of at least 0.3-0.5 km, with layer 1 and 2 thicknesses of 0.04-0.2 km and 0.2-0.34 km, respectively.

Once the P- and S-wave velocity models are developed, Poisson's ratio calculations are performed to investigate the crustal composition in the Goldstream

Valley region. Poisson's ratio, σ, is the ratio of radial contraction to axial elongation and can be expressed in terms of seismic velocities as follows

$$\sigma = \frac{\alpha^2 - 2\beta^2}{2(\alpha^2 - \beta^2)} \qquad (2)$$

where α is the P-wave velocity and β is the S-wave velocity. Values of σ range from 0 to 0.5 for solids, with very hard, rigid rocks having low Poisson's ratios and soft, poorly consolidated rocks having high Poisson's ratios. A typical average σ value for continental crust is 0.25 (*Stein and Wysession*, 2003).

Poisson ratios for the statically-corrected travel times are calculated at each Texan station for shots 1-5. The α and β values in these calculations are direct P- and S-wave velocities, respectively, determined from the arrival times of the seismic waves and the source/station distance. A different P- and S-wave velocity is determined for each shot at each station.

In order to determine the accuracy of the calculated Poisson ratio values, errors in picking the P and S arrivals at each station for each shot are determined. The corresponding error in Poisson's ratio, $\Delta\sigma$, for each shot is calculated using the derived equation

$$\Delta\sigma = \frac{\frac{1}{t_P}\left[-4\frac{\alpha^2}{\beta^2}(\Delta t_P) + 4\frac{\alpha}{\beta}(\Delta t_S)\right]}{\left(2\frac{\alpha^2}{\beta^2} - 2\right)^2} \qquad (3)$$

where Δt_P is the average error in P-wave arrival time picks, Δt_S is the average error in S-wave arrival time picks, and t_P is the P-wave arrival time. Using equation (3), the upper

and lower error bounds on the Poisson values can be determined, permitting a more complete structural analysis of the upper crust in the Goldstream Valley.

The calculated Poisson ratios and errors for each shot group as a function of source-receiver distance are shown in Figure 4. Poisson values at distances of < 7 km are highly scattered among the stations in all shot groups, particularly for shots 1 & 2 data, likely due to the uncertain S-wave measurements. At distances ≥ 7 km, the variance in Poisson ratio (σ) values is reduced. The average and standard deviation σ values for all distances, distances < 7 km, and distances ≥ 7 km are shown in Table 2 for each shot group and for shots 1-5 as a whole. From Figure 4 and Table 2 it can be clearly seen that

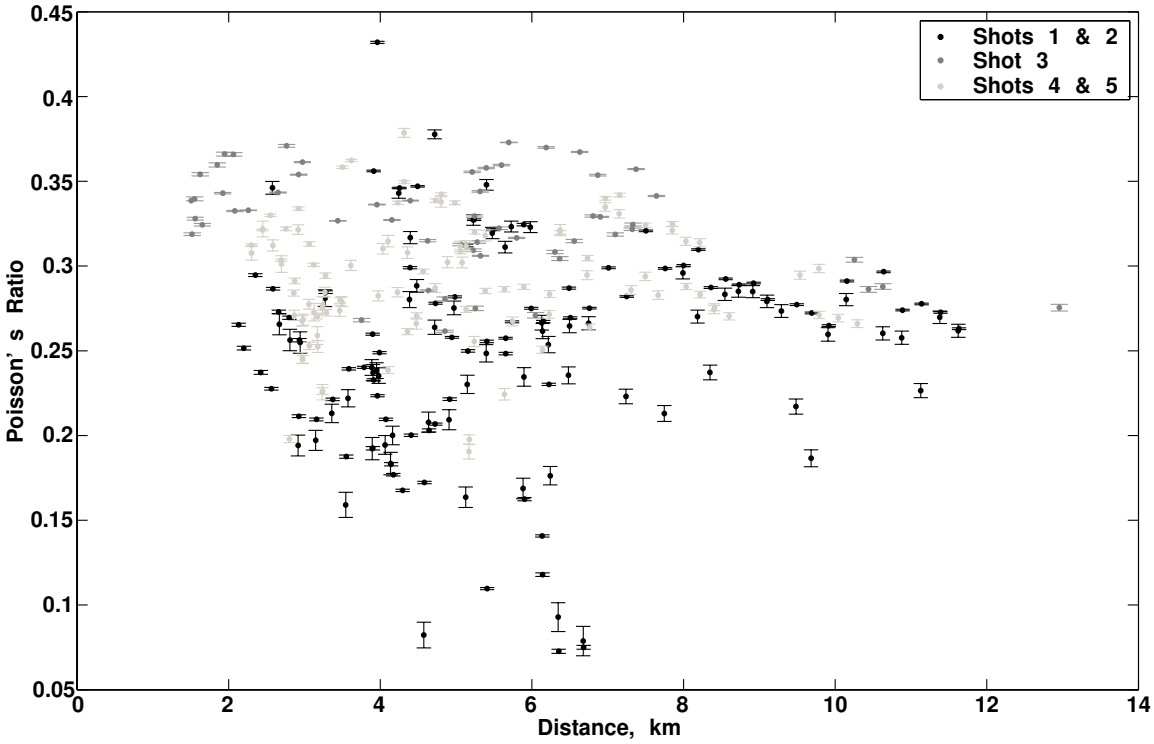

Figure 4. Poisson's ratio values and error bounds for each shot group. Shots 1 & 2 Poisson values are especially highly scattered at distances < 7 km, while values for all shot groups are less scattered at distances ≥ 7 km. Note that shot 3 data tend to give higher Poisson ratios than the other two shot groups.

Table 2. Average and Standard Deviation Poisson's Ratio Values

	All Distances		Distances < 7 km		Distances ≥ 7 km	
Data	σ_{avg}	σ_{std}	σ_{avg}	σ_{std}	σ_{avg}	σ_{std}
Shots 1-2	0.250	0.060	0.242	0.067	0.272	0.028
Shot 3	0.327	0.029	0.330	0.029	0.313	0.027
Shots 4-5	0.292	0.035	0.291	0.037	0.296	0.024
All shots	0.279	0.056	0.276	0.062	0.284	0.031

shot 3 data tend to yield the highest σ values at all distances, with an overall average of 0.33 ± 0.03. The disparity between shot 3 σ values and those of the other two shot groups is especially large for the close-in distance range.

In comparing the σ values found for the two distance ranges, it is important to note a few interesting patterns. For all shot groups, the standard deviation in the Poisson ratios is smaller for distances ≥ 7 km than for distances < 7 km. This is especially notable for the shots 1 & 2 data, which experience a nearly 60% reduction in standard deviation. The shot 3 data only show a 7% reduction in standard deviation, but these data also yield the most well constrained σ values at distances < 7 km, with a standard deviation of only 0.03. Additionally, the average σ values for shots 1 & 2 and shots 4 & 5 increase for the far distance range, while the mean shot 3 σ decreases. The increase in the mean shots 1 & 2 σ value is likely the result of a large reduction in the number of Poisson's ratios with low values.

IV. Time-term Analysis

The P- and S-wave arrival data are further analyzed using the time-term method, which determines the time needed for the seismic wave to travel from either the source to a refractor or from a refractor to the receiver. In the time-term approach, the travel time of the wave propagating between the i^{th} and j^{th} site (source and/or receiver locations) can be written as

$$t_{ij} = \frac{\Delta_{ij}}{V} + a_i + a_j \qquad (4)$$

where t_{ij} is the theoretical travel time, Δ_{ij} is the distance separating the i^{th} and j^{th} site measured along the surface, V is the velocity of the refractor, and a_i and a_j are the time-terms at the i^{th} and j^{th} site, respectively (*Berry and West,* 1966). For a source at site i and a receiver at site j, the time-terms a_i and a_j are the time for the wave to travel from the source to the refractor and the time for the wave to travel from the refractor to the receiver, respectively. These time-terms are solved for simultaneously using the set of linear algebraic equations formed from all possible t_{ij}. For each site (i or j), only one time-term is determined.

The application of the time-term method is based on several assumptions, including the following:

1) velocity varies only with depth (perpendicular to the refractor) within the critically refracted ray cone under the shot or station;
2) velocity of the refractor is constant;
3) slope and curvature of the refracting surface is small (*Berry and West*, 1966).

In order for the source time-terms to be solved for simultaneously with the station time-terms, receivers and shot points must be co-located. In the FRE setup, this situation did not occur, so a simplified time-term analysis is conducted in which the source time-terms are solved for separately from the station time-terms. The source time-terms are determined using the statically corrected P- and S-wave velocity model results to calculate the travel time of the P- and S-wave, respectively, from each shot location to the deepest refractor seen in refraction analysis.

The simplified source time-term, a_i, for the P-wave is calculated using the following equation

$$a_i = \frac{h_1}{V_1 \cos\theta_1} + \frac{h_2}{V_2 \cos\theta_c} \qquad (5)$$

where h_1 is the mean layer 1 thickness (in km), V_1 is the mean layer 1 velocity, θ_1 is $\sin^{-1}(V_1/V_3)$, with V_3 as the mean layer 3 velocity, h_2 is the mean layer 2 thickness (in km), V_2 is the mean layer 2 velocity, and θ_c (the critical angle) is $\sin^{-1}(V_2/V_3)$ (Figure 5a). A source time-term is calculated for each of the three shots being analyzed with this method (i.e. shots 2, 3, and 5).

The S-wave time-term analysis is performed using a different source time-term calculation than that used for the P-wave analysis since only 2 layers (at most) are seen in the statically corrected S-wave velocity models. The simplified source time-term, a_i, in this calculation uses the following equation

$$a_i = \frac{h_1}{V_1 \cos\theta_c} \qquad (6)$$

where h_1 is the mean layer 1 thickness (in km), V_1 is the mean layer 1 velocity, and θ_c (the critical angle) is $\sin^{-1}(V_1/V_2)$, with V_2 as the mean layer 2 velocity (Figure 5b).

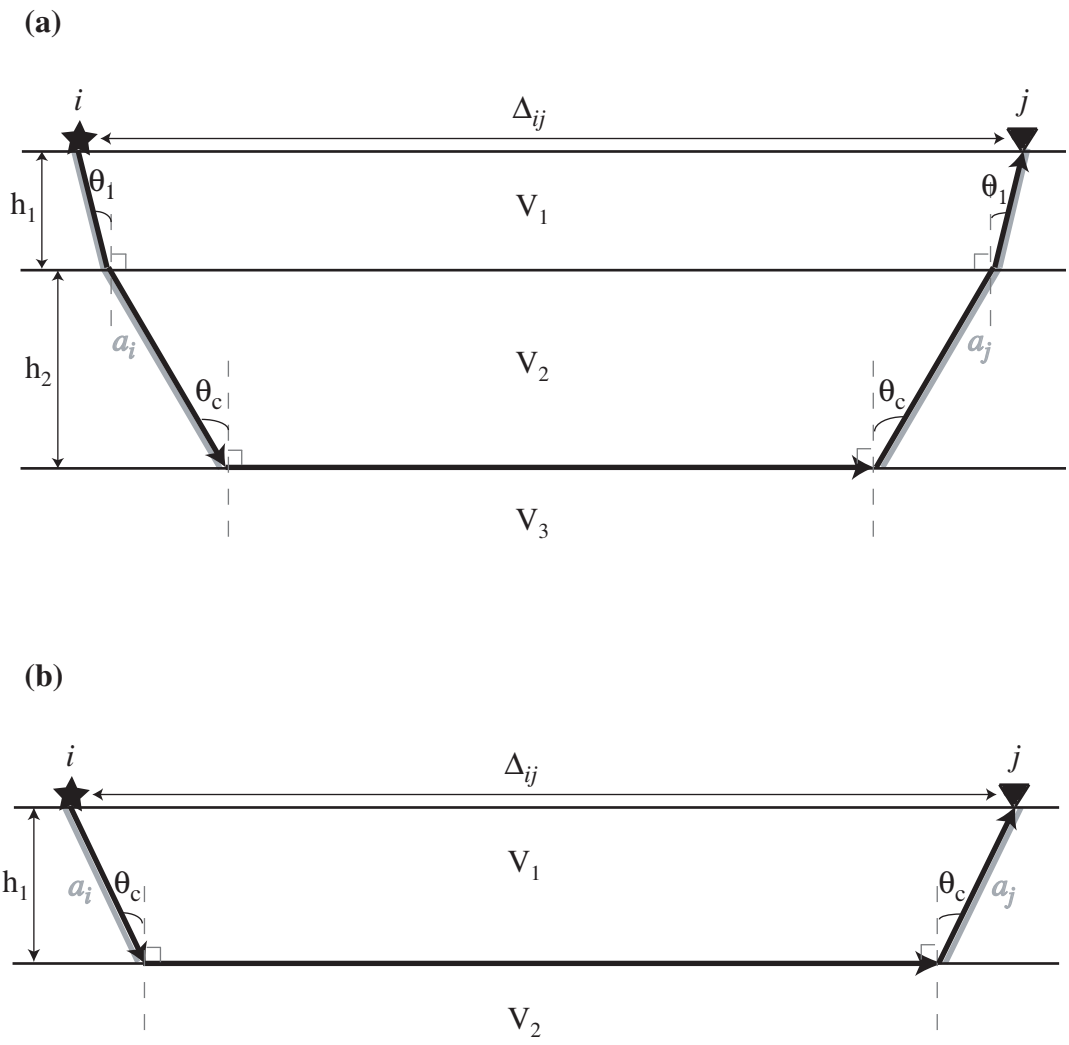

Figure 5. Time-term layout. (a) Three layer time-term analysis used for P-wave data, where heavy black line indicates wave path. (b) Two layer time-term analysis used for S-wave data. Grey lines indicate source (a_i) and station (a_j) time-term locations. The source and receiver locations are respectively marked by a star and inverted triangle. Δ_{ij} is the distance separating sites *i* and *j*, measured along the surface. The velocities (V_n) and thicknesses (h_n) of each layer are also shown.

Once the source time-terms are known, station time-terms are calculated for Texan stations that have arrival times picked for at least two of the shots of interest and

are located ≥ 2 km from the source. At these distances, the recorded body waves all refracted from the same layer, so we can be assured that time-terms calculated for each of these stations will be the time it takes the waves to travel to the surface from a common refractor. For the P-waves, time-terms for 86 stations are calculated, while only 69 stations could be used to calculate time-terms for the S-waves. This discrepancy in the number of stations reflects the difficulty in picking the S-wave arrivals.

Location maps of the calculated P- and S-wave time-terms for each station are shown in Figure 6, where the size of the circle indicates the duration of the time-term in seconds. The source time-terms calculated for each of the three shot locations are also shown (black dots). Note that the P-wave time-terms for the Texans located within the valley are smaller than those for the Texans located along the valley flanks at higher elevations, implying thinner overburden between the surface and the refractor in the valley (Figure 6a). This pattern can also be discerned from the S-wave time-term results (Figure 6b), although the distinction between valley and high elevation stations is less pronounced. For both the P- and S-wave results, the calculated source time-terms indicate the largest travel time for the shot 3 location. Based on the observed relation between P- and S-wave station time-terms and Texan elevation, it is thought that the shots 4 & 5 location would have the largest source time-term since it is at the highest elevation of the three test sites. This is based on the idea that for a horizontal refractor, it should take longer for the waves to travel from a higher elevation to the refractor than from a lower elevation. The fact that the calculated source time-terms do not support this

idea implies that the long travel time measured for the shot 3 location is the result of local lateral velocity variations, with slower velocity material beneath this test site.

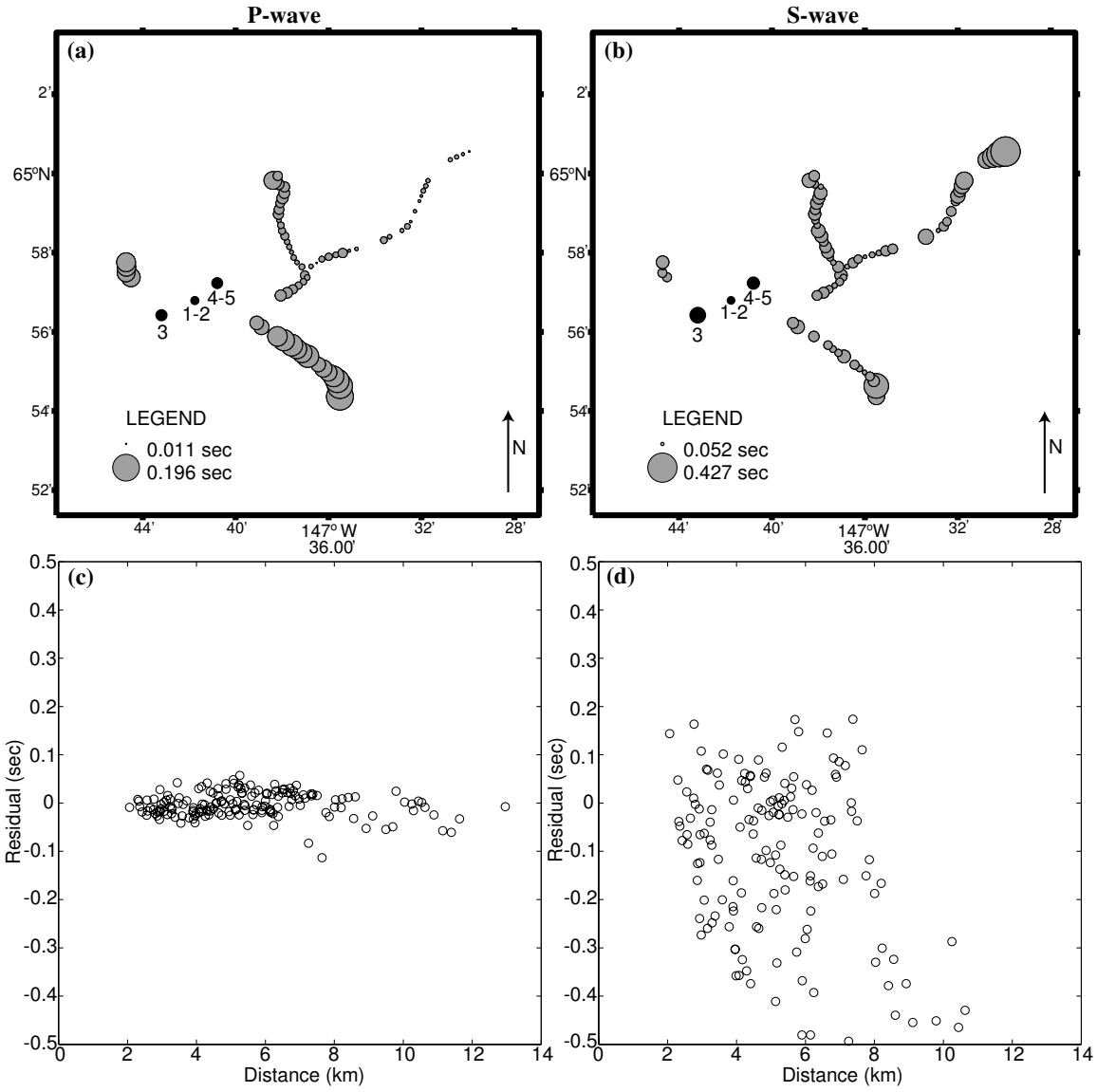

Figure 6. Time-terms for P- and S-waves and their residuals. (a) Location map of P-wave time-terms calculated for 86 Texan stations (grey dots) and three shot locations (black dots), where the radius of the dots indicate the length of the time-term in seconds. (b) Location map of S-wave time-terms calculated for 69 Texan stations and three shot locations. (c) Residuals of P-wave time-terms as a function of source-receiver distance. (d) Residuals of S-wave time-terms.

The magnitudes of the station P- and S-wave time-term residuals are calculated as the difference between the recorded travel time (T_{ij}) and the theoretical travel time (t_{ij}) at each Texan station (j) for each shot analyzed (i) as follows

$$residual_{ij} = T_{ij} - t_{ij} \qquad (7)$$

where t_{ij} is determined using the calculated source and station time-terms as described in equation (4). The values of these residuals with distance from the source are diagrammed in Figure 6c,d. Except for a few outliers, all of the P-wave residuals are within ± 0.1 s. The S-wave residuals, however, vary anywhere from +0.18 s to -0.5 s, with the majority having negative values. These negative residuals indicate that the calculated time-terms are too large and/or the calculated refractor velocity (V) is too slow. The large values of the residuals are possibly the result of uncertainties in the picking of the S-wave arrivals on the vertical-component Texan instruments. Alternatively, the large residuals may be the result of the inability to develop a two layer over a half-space S-wave velocity model using the refraction analysis.

V. Anisotropy

Based on the different P- and S-wave velocities found for each region in the refraction analyses (i.e. NW, SE, NE, and N), the possibility of azimuthal seismic velocity anisotropy in the upper crust is explored using the Texan data. Initial plots of apparent P- and S-wave velocity as a function of epicentral distance for each shot group are generated for both the original and the statically-corrected data, respectively. The velocities in these plots are calculated by dividing the station's distance from the source by the appropriate original or corrected P- or S-wave travel time. The P- and S-wave data for each shot group in these plots is fit with a curve, and the difference between the observed velocity and the velocity predicted for that distance from the curve fit through the data (dV) is computed. These dV values are plotted with respect to station azimuth for each shot group and body wave, and the resultant figures are examined to determine if there are any sinusoidal patterns which could be indicative of azimuthal anisotropy (with the fast azimuth direction(s) at the crest(s) of the curve) (Figure 7; *Beghoul and Barazangi,* 1990; *Herak et al.,* 2003; *Lokmer and Herak,* 1999). In order to account for the possible lateral variations in velocity from one Texan region to another, individual curves are also fit through the P- and S-wave velocity vs. distance data for each region in each shot group. Velocity differences (dV) are computed for each of these curves, and the resultant dV values for all four regions of each shot group are plotted with respect to station azimuth for each body wave. These figures are then examined for any sinusoidal patterns which could be indicative of azimuthal anisotropy.

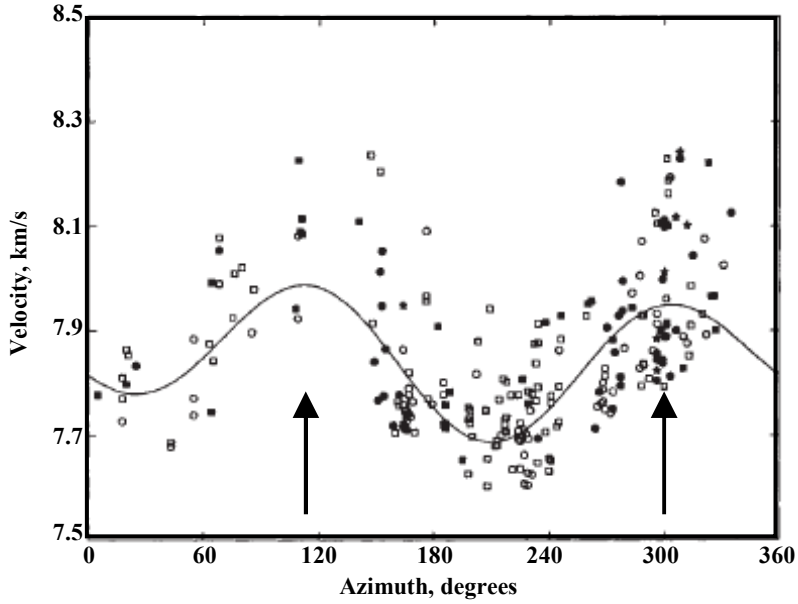

Figure 7. Sample azimuthal anisotropy plot. This figure illustrates the sinusoidal pattern indicative of azimuthal anisotropy for P-waves refracted off the top of the mantle beneath the Basin and Range province. The arrows indicate the fast azimuth directions (~120° and ~300°) at the crests of the curve. Modified from *Beghoul and Barazangi* (1990).

Initial plots of apparent P- and S-wave velocity with respect to epicentral distance for each shot group using statically-corrected data for Texans located at source-receiver distances ≥ 2 km are shown in Figure 8. For both body waves and all shot groups, the velocities increase gradually with distance out to ~7 km, beyond which they remain approximately constant (Figure 8). The dV values computed from fitting quadratic polynomial least-squares curves (Figure 8) to the velocity vs. distance data for each shot group for P- and S-waves are plotted as a function of station azimuth in Figures 9 and 10, respectively. Sinusoidal patterns are observed in the P-wave data for all three shots groups (Figure 9) and in the S-wave data for shot 3 (Figure 10b). Sample sinusoids are plotted in these figures to illustrate the observed sinusoidal patterns. These sinusoidal

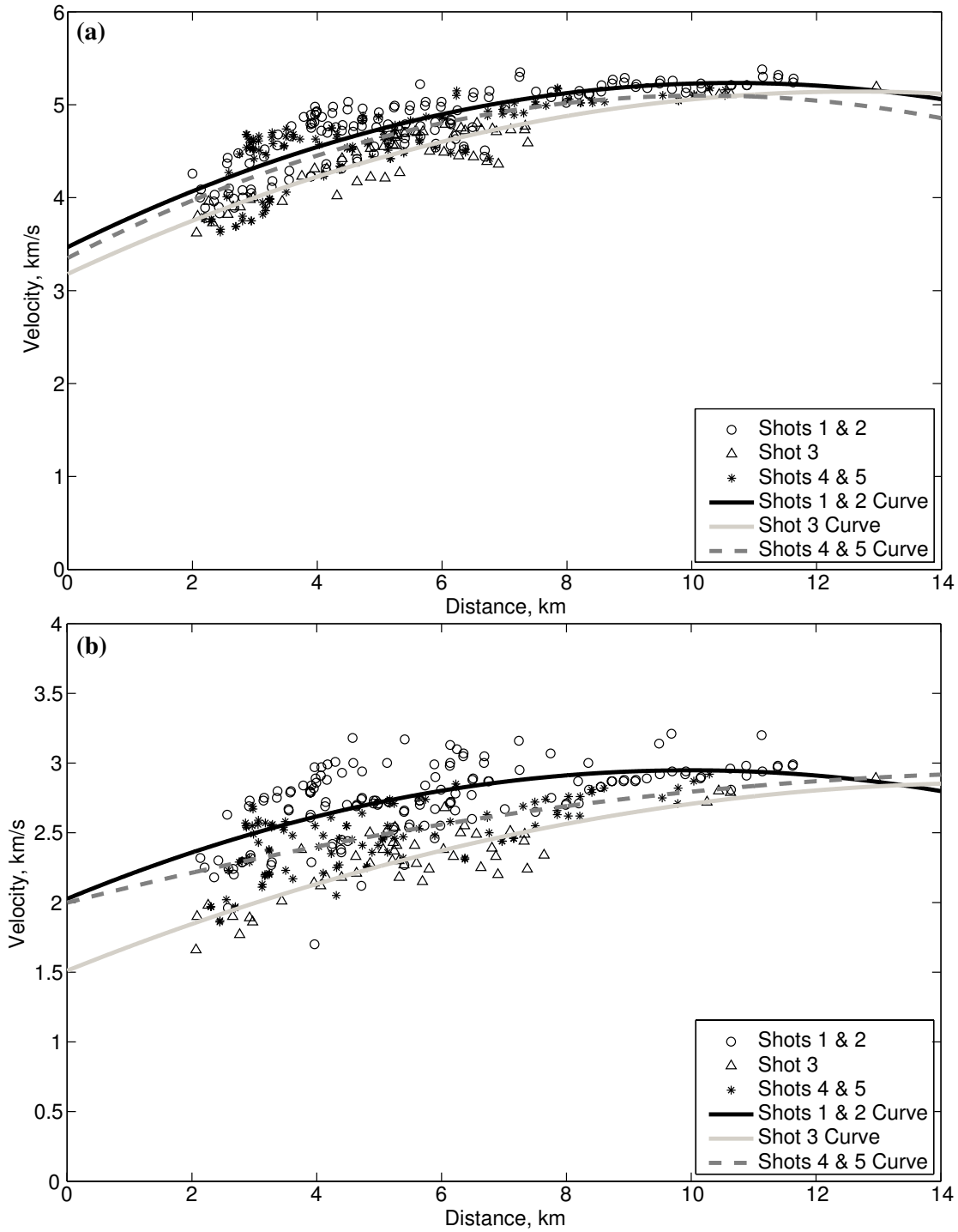

Figure 8. Apparent velocity with epicentral distance for statically-corrected P-wave (a) and S-wave (b) data from Texans located at source-receiver distances ≥ 2 km. For both waves, note that velocities increase gradually with distance out to ~7 km, beyond which velocities remain approximately constant. This trend in the data is illustrated with quadratic polynomial least-squares curves fit to the data for each shot group (black, grey, and dashed lines).

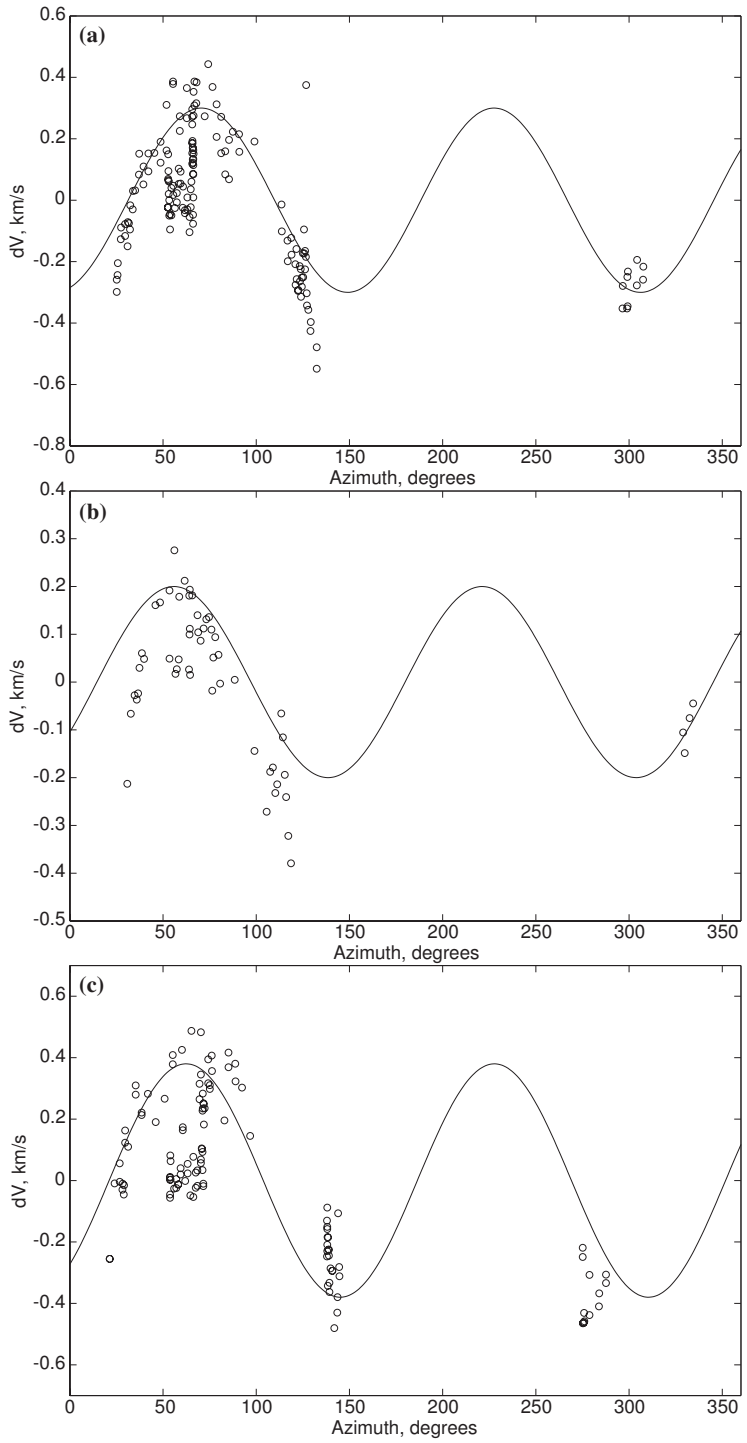

Figure 9. P-wave velocity differences (dV) with station azimuth for statically-corrected shots 1 & 2 (a), shot 3 (b), and shots 4 & 5 (c) data. These dV values are calculated as the difference between the observed velocity and the velocity predicted for that distance from a curve fit through the data in Figure 8a for each shot group. Sinusoidal patterns are indicated by sample sinusoid curves (black line).

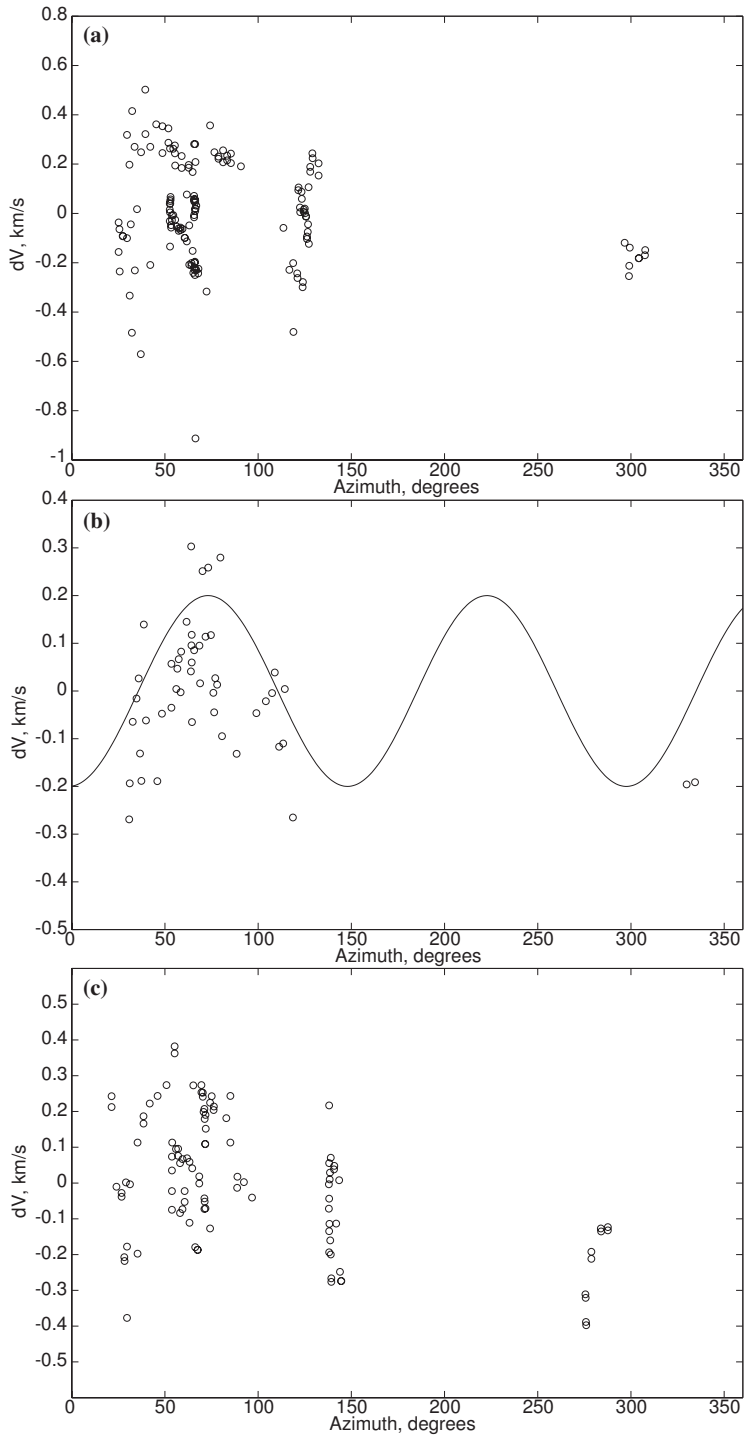

Figure 10. S-wave velocity differences (dV) with station azimuth for statically-corrected shots 1 & 2 (a), shot 3 (b), and shots 4 & 5 (c) data. These dV values are calculated as the difference between the observed velocity and the velocity predicted for that distance from a curve fit through the data in Figure 8b for each shot group. A sinusoidal pattern is only observed for shot 3 data and is indicated by a sample sinusoid (black line).

patterns could be indicative of azimuthal anisotropy, with fast directions of ~55˚-70˚ for P-waves and ~73˚ for S-waves. The dV values calculated from fitting least-squares quadratic polynomial curves to the P- and S-wave velocity vs. distance data for each region in each shot group (Figures 11 and 12) are plotted with respect to station azimuth in Figures 13 and 14. From these figures it can clearly be seen that no sinusoidal patterns are indicated by either the P- or S-wave data for any shot group. This lack of a sinusoidal pattern indicates that the sinusoids observed in Figures 9 and 10b probably are the result of laterally varying P- and S-wave velocities, which are mimicking the appearance of azimuthal anisotropy. If azimuthal anisotropy was actually present in the Goldstream Valley, then some evidence of a sinusoidal pattern should be resolvable in plots of regional dV values as a function of azimuth (Figures 13 and 14).

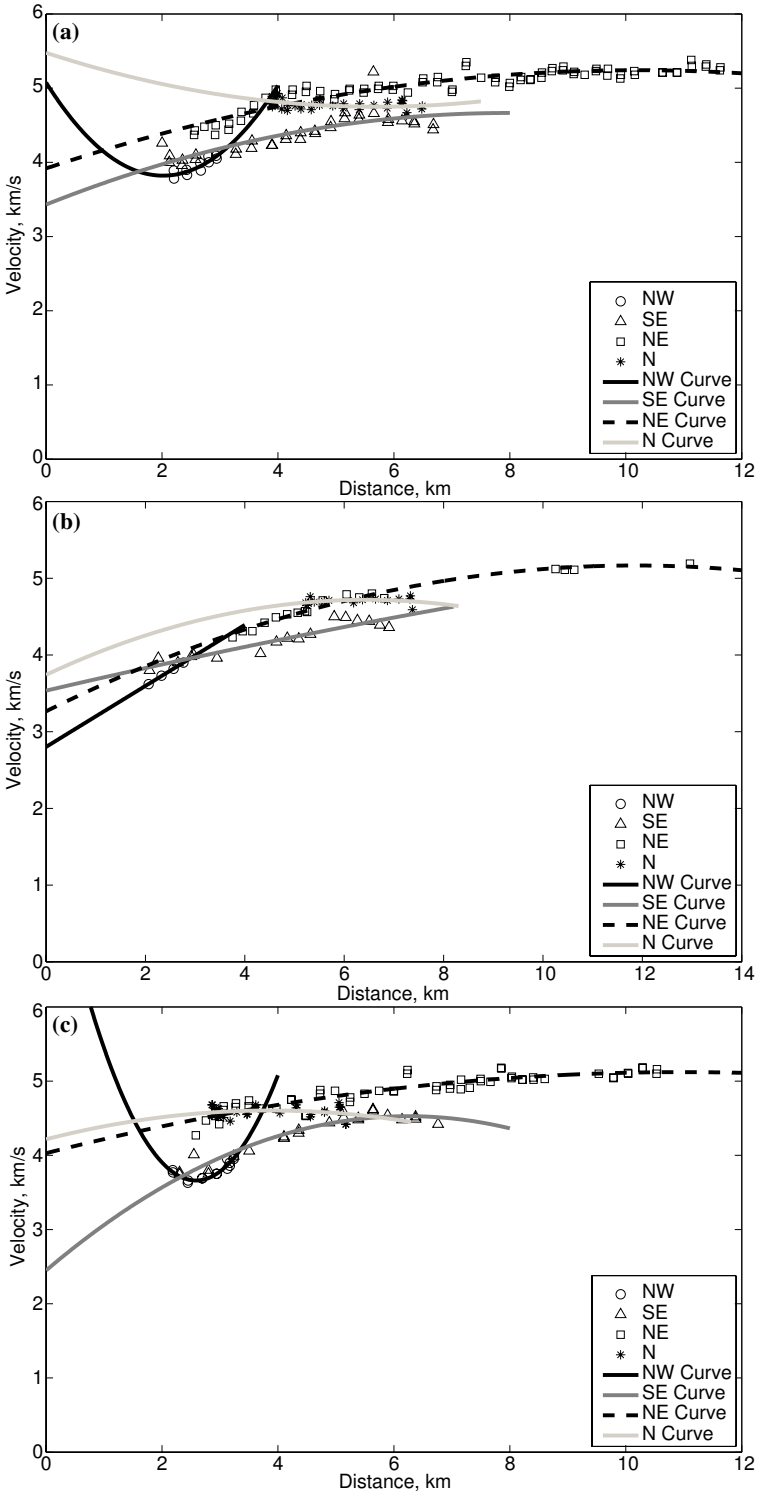

Figure 11. Regional apparent velocity with epicentral distance for statically-corrected P-wave data for shots 1 & 2 (a), shot 3 (b), and shots 4 & 5 (c). Quadratic polynomial least-squares curves fit to the data for each Texan region in each shot group are shown.

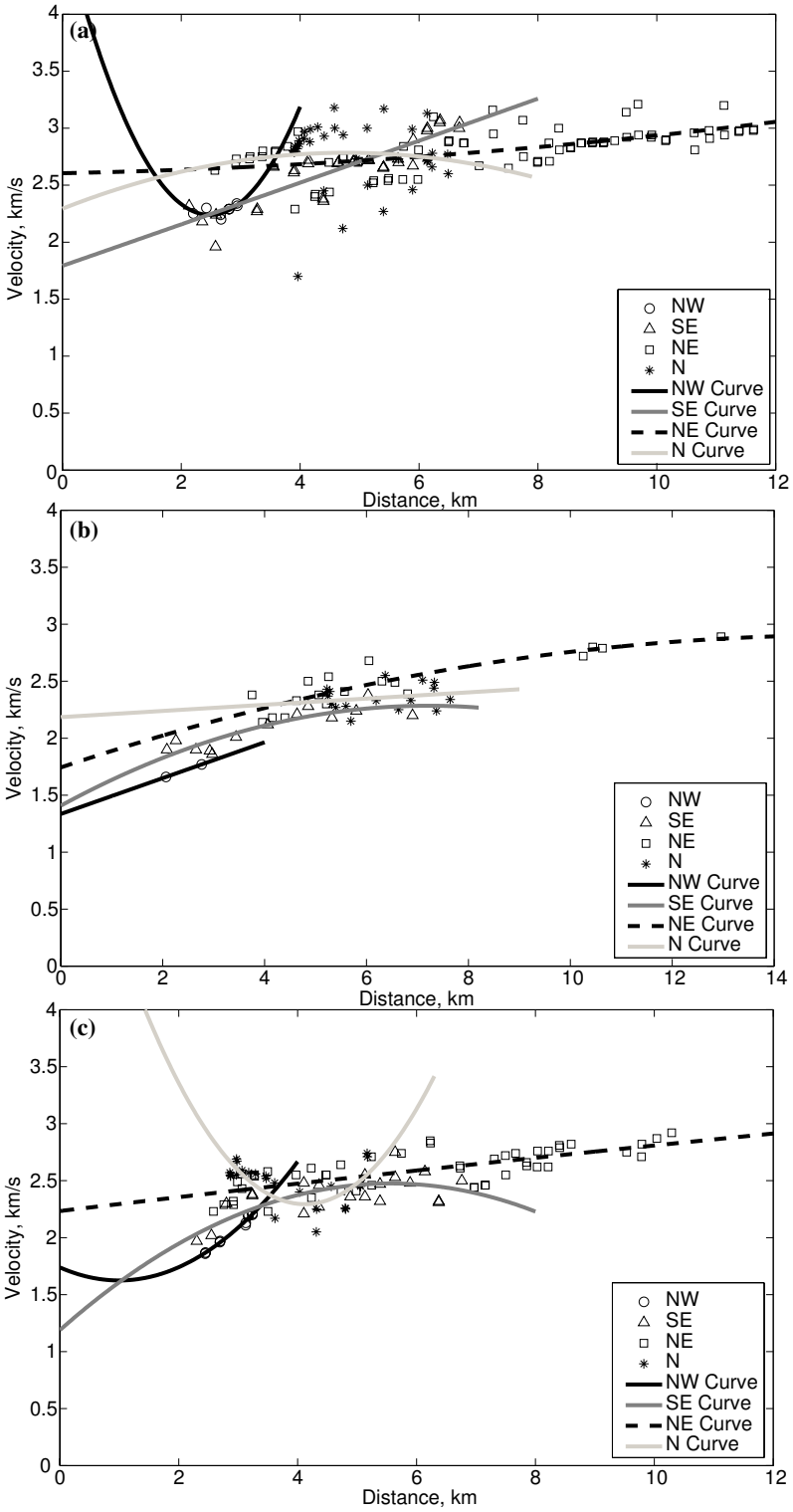

Figure 12. Regional apparent velocity with epicentral distance for statically-corrected S-wave data for shots 1 & 2 (a), shot 3 (b), and shots 4 & 5 (c). Quadratic polynomial least-squares curves fit to the data for each Texan region in each shot group are shown.

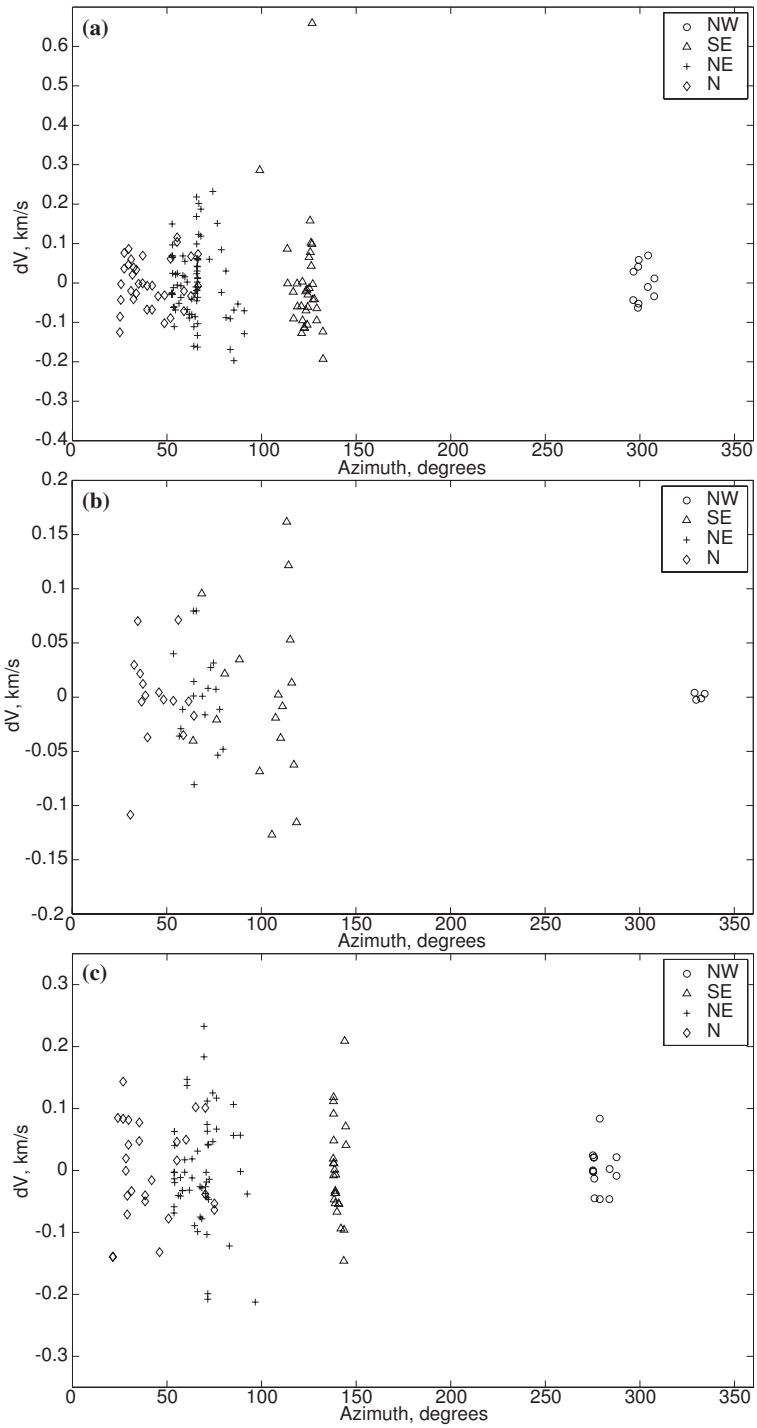

Figure 13. Regional P-wave velocity differences (dV) with station azimuth for statically-corrected shots 1 & 2 (a), shot 3 (b), and shots 4 & 5 (c) data. These dV values are calculated as the difference between the observed velocity and the velocity predicted for that distance from a curve fit through the velocity vs. distance data for each Texan region in each shot group (Figure 11). No sinusoidal patterns are observed.

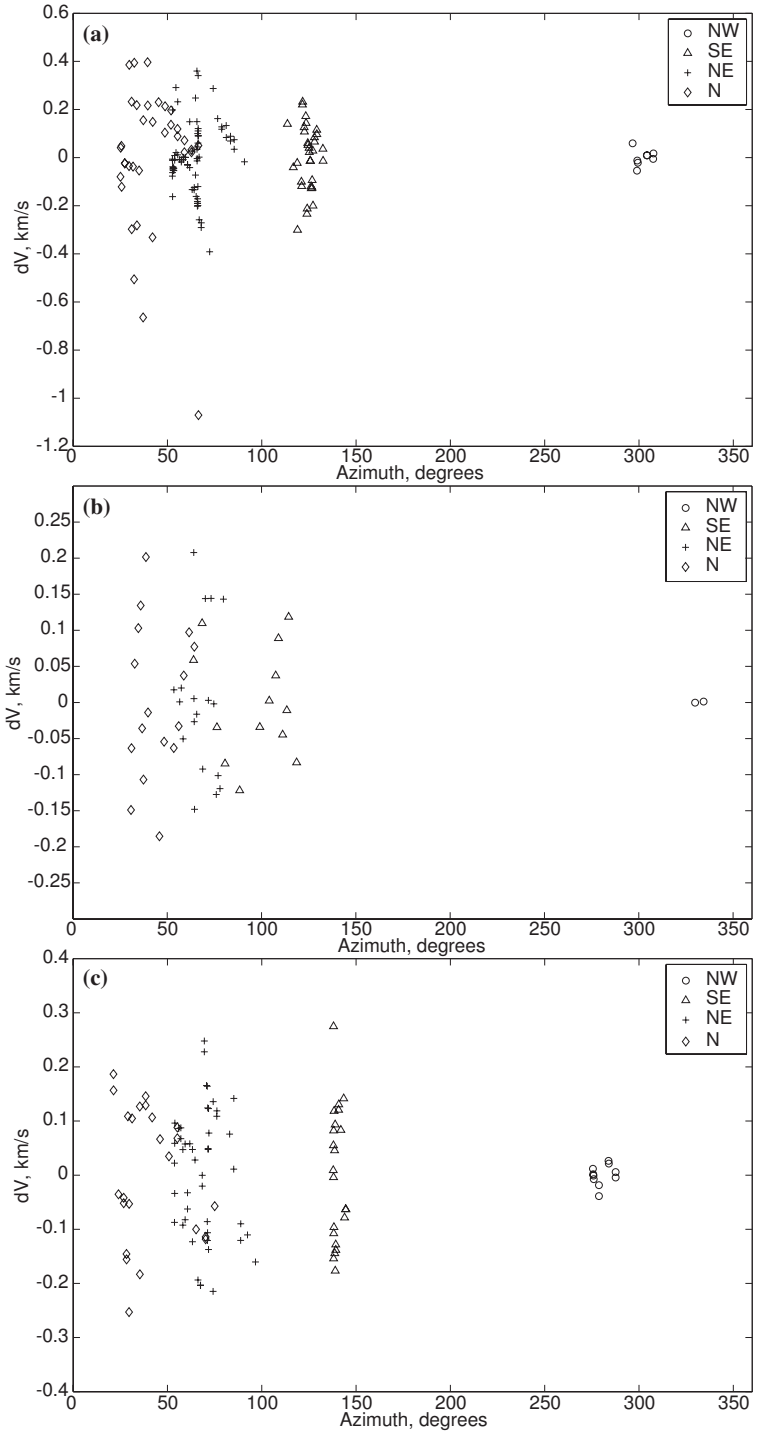

Figure 14. Regional S-wave velocity differences (dV) with station azimuth for statically-corrected shots 1 & 2 (a), shot 3 (b), and shots 4 & 5 (c) data. These dV values are calculated as the difference between the observed velocity and the velocity predicted for that distance from a curve fit through the velocity vs. distance data for each Texan region in each shot group (Figure 12). No sinusoidal patterns are observed.

VI. Surface Waves

In addition to the simple refraction analysis, the S-wave velocity structure of the upper crust is determined through dispersion curve analysis and inversion of 0.2-2 sec period fundamental mode Rayleigh (Rg) waves. The Rg signals are extracted using the multiple filter analysis technique of *Dziewonski et al.* (1969). This technique is executed using a Matlab program developed by Jessie Bonner (WGC) which involves narrow-band Butterworth filters, but compares favorably to *Herrmann's* (2004) version that considers Gaussian filters. This method filters the vertical component waveforms for all shots at all Texan stations at regular periods between 0.2 and 2 seconds and then maps the maximum amplitudes as a function of group velocity to determine Rg dispersion curves. The calculated dispersion curves for shot 1 data are shown in Figure 15. These dispersion data indicate the fastest group velocities for the NE Texans, while the slowest group velocities are seen in the NW. This result is consistent among all five shots.

Once they have been determined, the surface wave dispersion curves for each station are averaged together by shot group, and these average dispersion curves are inverted to determine the shear-wave velocity structure in the upper crust along the line where the dispersion data were collected. These damped, least squares inversions are carried out using *Herrmann's* (2004) surface wave inversion program (surf96) and starting P-wave velocity models developed from the refraction analyses conducted in this study. For depths below the deepest levels for which velocity information was obtained from the refraction analysis (~1-2 km), P-wave velocities (V_P) are taken from the CRUST 2.0 reference earth model (*Laske et al.,* 2001). Since the refraction results do not contain

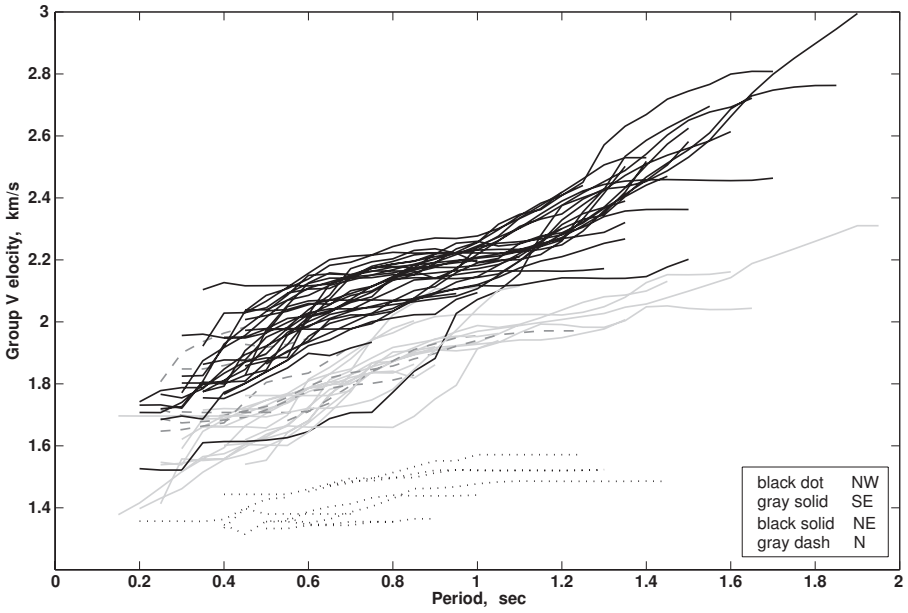

Figure 15. Rg dispersion curves for shot 1. Results are shown by region: NW (black dotted lines), SE (gray solid lines), NE (black solid lines), and N (gray dashed lines). The fastest group velocities are found for the NE data, while the slowest group velocities are seen in the NW data.

a complete S-wave model from the surface down to 2 km depth, but instead only include a velocity value for the halfspace at a depth of 0.3-0.5 km, the S-wave velocities (V_S) used in the starting models are all calculated using a standard V_P/V_S ratio of 1.73 and the P-wave velocities from refraction and CRUST 2.0 noted above. Densities (ρ) for each layer in the starting models are determined using Gardner's rule, which calculates ρ (in g/cm^3) using the following equation

$$\rho = 0.32 V_P^{0.25} \qquad (8)$$

where V_P is in units of meters/sec (*Gardner et al.,*1974).

The resultant individual inversion models for each source-receiver pair in a region are averaged to generate a different S-wave velocity model for each of the four regions in each shot group. These shear-wave velocity models are then paired with the P-wave

refraction analysis results (and CRUST 2.0 values) to create a complete set of regional 1-D models of P- and S-wave velocities in the upper 2 km of the crust. Synthetic seismograms are generated for each of these models using a waveform-integration program (*Herrmann,* 2004). These waveforms are then compared to the recorded data to determine any differences between observed and theoretical wave arrivals.

The average regional 1-D P- and S-wave velocity models of the upper crust for each shot group are illustrated in Figure 16, with the detailed velocities of each layer listed in Tables 3-5. In all shot groups, the fastest S-wave velocities to a depth of 1.1 km are seen for the NE region. This region also yields the fastest P-wave velocities at depths

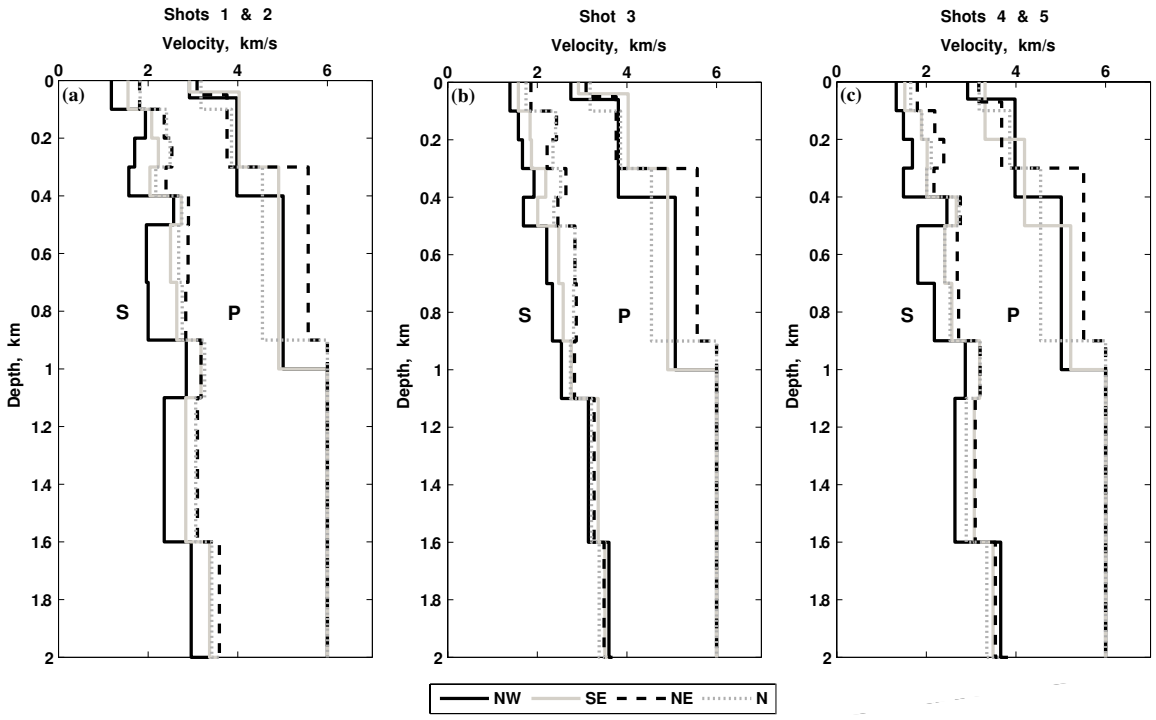

Figure 16. Average 1-D P- and S-wave velocity models for each region. Regional velocity models for shots 1 & 2 (a), shot 3 (b), and shots 4 & 5 (c) are shown. The fastest velocities are seen in the NE for each S-wave model to 1.1 km depth and for each P-wave model between 0.3 km and 1 km depth. Below 1 km depth, P-wave velocities for all regions are 6.0 km/s (taken from CRUST 2.0; *Laske et al.,* 2001).

between 0.3 km and 1 km. Below this depth range, the P-wave velocities for all regions are identically 6 km/s as these results are taken from CRUST 2.0, which only provides one velocity for the entire Goldstream Valley region of central Alaska. Above 3 km depth, the fastest P-wave velocities are found in the SE and NE for shots 1 & 2 and shot 3 data, while shots 4 & 5 data yield fastest velocities in the SE and NW. Overall, the slowest S-wave velocities are seen for the NW region, while the slowest regional P-wave velocities vary by depth and shot group.

Along with the velocity and density measurements, a calculated Poisson's ratio for each layer is also shown in the 1-D velocity model results in Tables 3-5. In comparing the models for each region, it is clear that the NW model yields the highest σ for all shot groups, especially in the shallow subsurface, with values ranging from 0.328 to 0.452 in the first 60 m of depth. Overall, the average σ for the entire depth range of the velocity models is highest for the NW region (Table 6). The lowest average σ value is found in the N model for both shots 1 & 2 and shot 3 data, while the NE model gives the lowest mean σ value for shots 4 & 5 data (Table 6). Recalling that a low Poisson's ratio indicates harder rock and a high Poisson's ratio indicates softer, less consolidated material, it is possible that these results are highlighting important geological variations among the different regions explored in this study. This concept will be explored further in the discussion section of this thesis.

Table 3. Average 1-D Velocity Models for Shots 1 & 2

NW					SE					NE					N				
Depth to Top, km	α, km/s	β, km/s	ρ, g/cm^3	σ	Depth to Top, km	α, km/s	β, km/s	ρ, g/cm^3	σ	Depth to Top, km	α, km/s	β, km/s	ρ, g/cm^3	σ	Depth to Top, km	α, km/s	β, km/s	ρ, g/cm^3	σ
0	2.92	1.18	2.35	0.402	0	2.92	1.55	2.35	0.304	0	3.09	1.81	2.39	0.239	0	3.18	1.82	2.40	0.256
0.01	2.92	1.18	2.35	0.402	0.04	4.03	1.55	2.55	0.413	0.01	3.09	1.81	2.39	0.239	0.01	3.18	1.82	2.40	0.256
0.06	3.98	1.18	2.54	0.452	0.1	4.03	2.08	2.55	0.318	0.05	3.76	1.81	2.51	0.349	0.05	3.18	1.82	2.40	0.256
0.1	3.98	1.94	2.54	0.344	0.2	4.03	2.23	2.55	0.279	0.1	3.76	2.36	2.51	0.175	0.1	3.86	2.41	2.52	0.181
0.2	3.98	1.70	2.54	0.388	0.3	4.91	2.04	2.68	0.396	0.2	3.76	2.53	2.51	0.086	0.2	3.86	2.49	2.52	0.144
0.3	3.98	1.57	2.54	0.408	0.4	4.91	2.74	2.68	0.274	0.3	5.57	2.40	2.76	0.386	0.3	4.55	2.17	2.63	0.353
0.4	5.01	2.57	2.69	0.321	0.5	4.91	2.50	2.68	0.325	0.4	5.57	2.90	2.76	0.314	0.4	4.55	2.75	2.63	0.212
0.5	5.01	1.96	2.69	0.410	0.7	4.91	2.64	2.68	0.297	0.5	5.57	2.89	2.76	0.316	0.5	4.55	2.68	2.63	0.234
0.7	5.01	2.00	2.69	0.405	0.9	4.91	3.18	2.68	0.139	0.7	5.57	2.84	2.76	0.324	0.7	4.55	2.76	2.63	0.209
0.9	5.01	2.85	2.69	0.261	1.0	6.00	3.18	2.82	0.305	0.9	6.00	3.18	2.82	0.305	0.9	6.00	3.26	2.82	0.291
1.0	6.00	2.85	2.82	0.354	1.1	6.00	2.84	2.82	0.356	1.1	6.00	3.10	2.82	0.318	1.1	6.00	3.06	2.82	0.324
1.1	6.00	2.36	2.82	0.408	1.6	6.00	3.37	2.82	0.270	1.6	6.00	3.59	2.82	0.221	1.6	6.00	3.42	2.82	0.259
1.6	6.00	2.96	2.82	0.339	2.0	6.00	3.55	2.82	0.231	2.0	6.00	3.50	2.82	0.242	2.0	6.00	3.58	2.82	0.224
2.0	6.00	3.38	2.82	0.268															

Table 4. Average 1-D Velocity Models for Shot 3

NW					SE					NE					N				
Depth to Top, km	α, km/s	β, km/s	ρ, g/cm^3	σ	Depth to Top, km	α, km/s	β, km/s	ρ, g/cm^3	σ	Depth to Top, km	α, km/s	β, km/s	ρ, g/cm^3	σ	Depth to Top, km	α, km/s	β, km/s	ρ, g/cm^3	σ
0	2.75	1.39	2.32	0.328	0	2.92	1.58	2.35	0.293	0	3.09	1.86	2.39	0.216	0	3.18	1.75	2.40	0.283
0.01	2.75	1.39	2.32	0.328	0.04	4.03	1.58	2.55	0.409	0.01	3.09	1.86	2.39	0.216	0.01	3.18	1.75	2.40	0.283
0.06	3.81	1.39	2.51	0.423	0.1	4.03	1.84	2.55	0.368	0.05	3.76	1.86	2.51	0.338	0.05	3.18	1.75	2.40	0.283
0.1	3.81	1.58	2.51	0.396	0.2	4.03	1.87	2.55	0.363	0.1	3.76	2.43	2.51	0.141	0.1	3.86	2.41	2.52	0.181
0.2	3.81	1.67	2.51	0.381	0.3	4.91	2.19	2.68	0.376	0.2	3.76	2.22	2.51	0.232	0.2	3.86	2.35	2.52	0.206
0.3	3.81	1.93	2.51	0.327	0.4	4.91	2.01	2.68	0.399	0.3	5.57	2.64	2.76	0.355	0.3	4.55	2.52	2.63	0.279
0.4	5.08	1.69	2.70	0.438	0.5	4.91	2.48	2.68	0.329	0.4	5.57	2.46	2.76	0.379	0.4	4.55	2.37	2.63	0.314
0.5	5.08	2.21	2.70	0.383	0.7	4.91	2.58	2.68	0.309	0.5	5.57	2.84	2.76	0.324	0.5	4.55	2.84	2.63	0.181
0.7	5.08	2.34	2.70	0.365	0.9	4.91	2.76	2.68	0.269	0.7	5.57	2.87	2.76	0.319	0.7	4.55	2.81	2.63	0.192
0.9	5.08	2.54	2.70	0.333	1.0	6.00	2.76	2.82	0.366	0.9	6.00	2.83	2.82	0.357	0.9	6.00	2.74	2.82	0.368
1.0	6.00	2.54	2.82	0.391	1.1	6.00	3.36	2.82	0.272	1.1	6.00	3.27	2.82	0.289	1.1	6.00	3.21	2.82	0.299
1.1	6.00	3.14	2.82	0.311	1.6	6.00	3.51	2.82	0.240	1.6	6.00	3.49	2.82	0.244	1.6	6.00	3.38	2.82	0.268
1.6	6.00	3.60	2.82	0.219	2.0	6.00	3.57	2.82	0.226	2.0	6.00	3.51	2.82	0.240	2.0	6.00	3.50	2.82	0.242
2.0	6.00	3.68	2.82	0.198															

Table 5. Average 1-D Velocity Models for Shots 4 & 5

NW					SE					NE					N				
Depth to Top, km	α, km/s	β, km/s	ρ, g/cm^3	σ	Depth to Top, km	α, km/s	β, km/s	ρ, g/cm^3	σ	Depth to Top, km	α, km/s	β, km/s	ρ, g/cm^3	σ	Depth to Top, km	α, km/s	β, km/s	ρ, g/cm^3	σ
0	2.92	1.33	2.35	0.369	0	3.31	1.52	2.43	0.366	0	3.17	1.80	2.40	0.262	0	3.18	1.65	2.40	0.316
0.01	2.92	1.33	2.35	0.369	0.05	3.31	1.52	2.43	0.366	0.01	3.17	1.80	2.40	0.262	0.01	3.18	1.65	2.40	0.316
0.06	3.98	1.33	2.54	0.437	0.1	3.31	1.89	2.43	0.258	0.07	3.68	1.80	2.49	0.343	0.05	3.18	1.65	2.40	0.316
0.1	3.98	1.49	2.54	0.419	0.2	4.19	2.02	2.57	0.349	0.1	3.68	2.19	2.49	0.226	0.1	3.86	1.90	2.52	0.340
0.2	3.98	1.69	2.54	0.390	0.3	4.19	2.01	2.57	0.351	0.2	3.68	2.39	2.49	0.135	0.2	3.86	2.11	2.52	0.287
0.3	3.98	1.49	2.54	0.419	0.4	4.19	2.67	2.57	0.158	0.3	5.51	2.17	2.76	0.408	0.3	4.55	2.01	2.63	0.379
0.4	5.01	2.46	2.69	0.341	0.5	5.22	2.41	2.72	0.365	0.4	5.51	2.76	2.76	0.333	0.4	4.55	2.73	2.63	0.219
0.5	5.01	1.81	2.69	0.425	0.7	5.22	2.57	2.72	0.340	0.5	5.51	2.69	2.76	0.344	0.5	4.55	2.41	2.63	0.305
0.7	5.01	2.18	2.69	0.383	0.9	5.22	3.19	2.72	0.202	0.7	5.51	2.72	2.76	0.339	0.7	4.55	2.53	2.63	0.276
0.9	5.01	2.87	2.69	0.256	1.0	6.00	3.19	2.82	0.303	0.9	6.00	3.20	2.82	0.301	0.9	6.00	3.20	2.82	0.301
1.0	6.00	2.87	2.82	0.352	1.1	6.00	3.07	2.82	0.323	1.1	6.00	3.09	2.82	0.320	1.1	6.00	2.89	2.82	0.349
1.1	6.00	2.64	2.82	0.380	1.6	6.00	3.49	2.82	0.244	1.6	6.00	3.54	2.82	0.233	1.6	6.00	3.35	2.82	0.274
1.6	6.00	3.66	2.82	0.204	2.0	6.00	3.51	2.82	0.240	2.0	6.00	3.60	2.82	0.219	2.0	6.00	3.62	2.82	0.214
2.0	6.00	3.82	2.82	0.159															

Table 6. Average Poisson's Ratio for 1-D Velocity Models

Data	Region	σ_{avg}	σ_{std}
Shots 1-2	NW	0.369	0.06
	SE	0.300	0.07
	NE	0.270	0.08
	N	0.246	0.06
Shot 3	NW	0.345	0.07
	SE	0.325	0.06
	NE	0.281	0.07
	N	0.260	0.06
Shots 4-5	NW	0.350	0.08
	SE	0.297	0.07
	NE	0.286	0.07
	N	0.299	0.05

For each of the 1-D velocity models found, synthetic seismograms are generated for a sample of Texan stations using *Herrmann's* (2004) waveform-integration program and regional attenuation models developed by Jessie Bonner and Mark Leidig for the Goldstream Valley (personal communication, 2008). These synthetic seismograms are produced in order to qualitatively estimate how well the 1-D models explain variations in the observed waveforms. Both the original and synthetic seismograms are bandpass filtered between 0.5 Hz and 2 Hz using a 6^{th} order zero-phase Butterworth filter to highlight the surface waves. Among all three shot groups, the velocity model generated for the NE region produces synthetic seismograms that most accurately replicate the major features of the observed waveforms (Figures 17c-19c). This result could indicate that the NE is the best modeled region in this study, which may be a consequence of the fact that the NE contained the highest number of Texan stations among the four regions, yielding a more constrained model.

Comparisons of the observed and synthetic waveforms for each shot group illustrate that the predicted surface wave is less dispersed than that which was recorded for most stations (Figures 17-19). The observed seismograms contain a dispersed surface wave packet with considerable ringing at the tail end of the waveform that is not predicted by the synthetics. In order to get the synthetic wave energy to spread out more and possibly reproduce the observed ringing, more low velocity layers need to be added near the surface in the 1-D models.

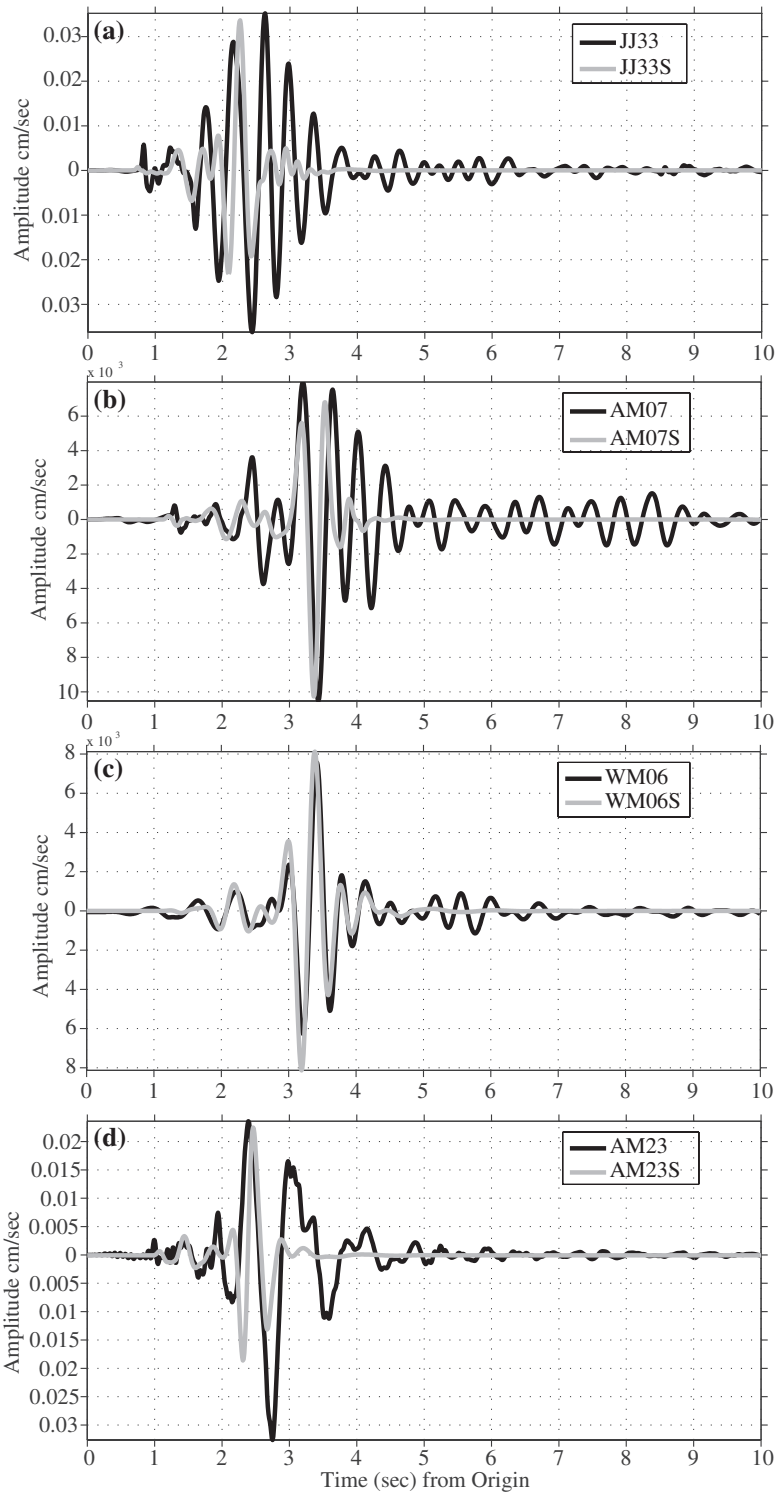

Figure 17. Observed vs. synthetic seismograms for shots 1 & 2 1-D models. Examples from the NW (a), SE (b), NE (c), and N (d) models are shown. The four digit letter/number combination is the name of the Texan station, and the "S" indicates synthetic.

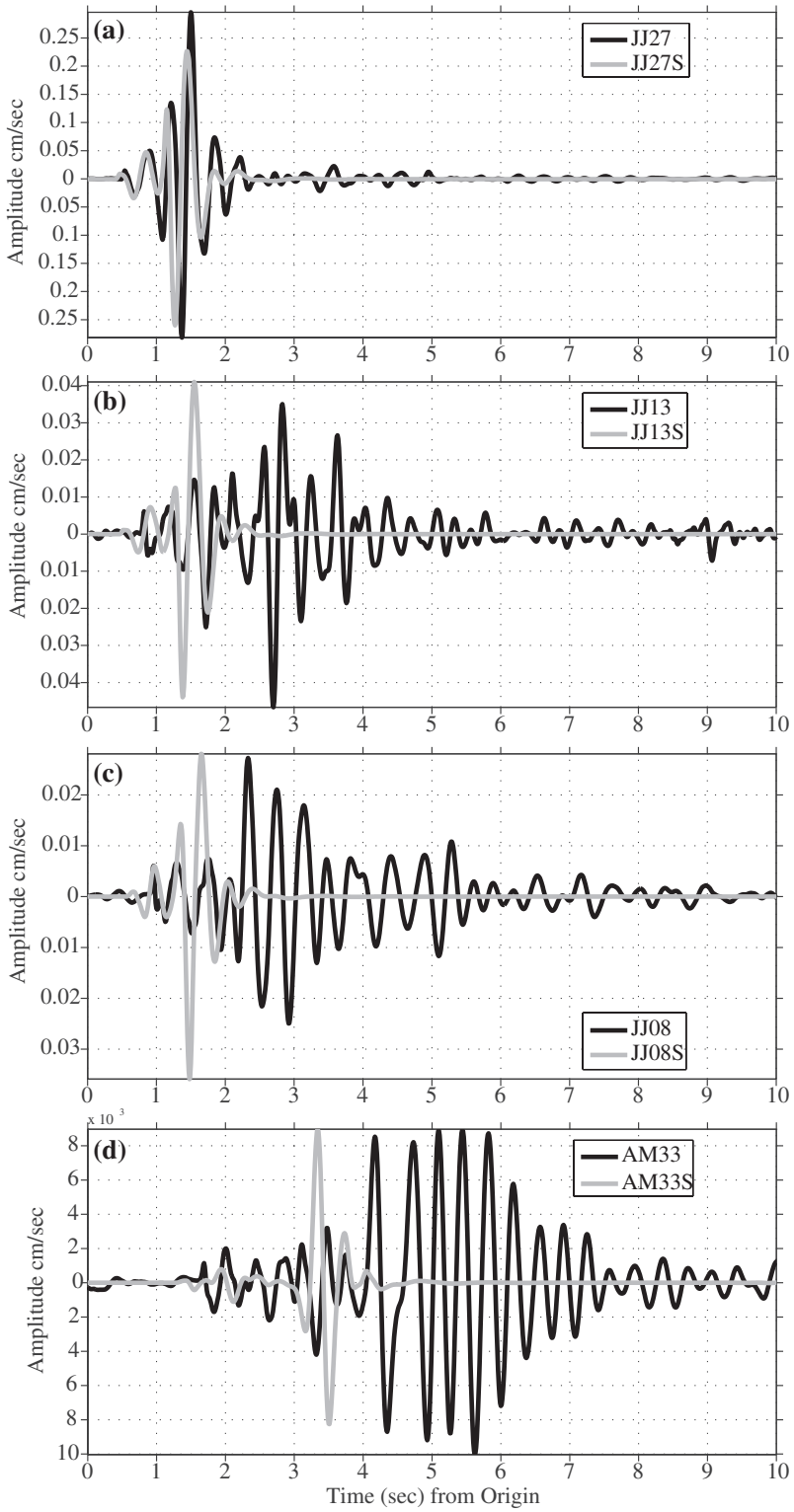

Figure 18. Observed vs. synthetic seismograms for shot 3 1-D models. Examples from the NW (a), SE (b), NE (c), and N (d) models are shown. The four digit letter/number combination is the name of the Texan station, and the "S" indicates synthetic.

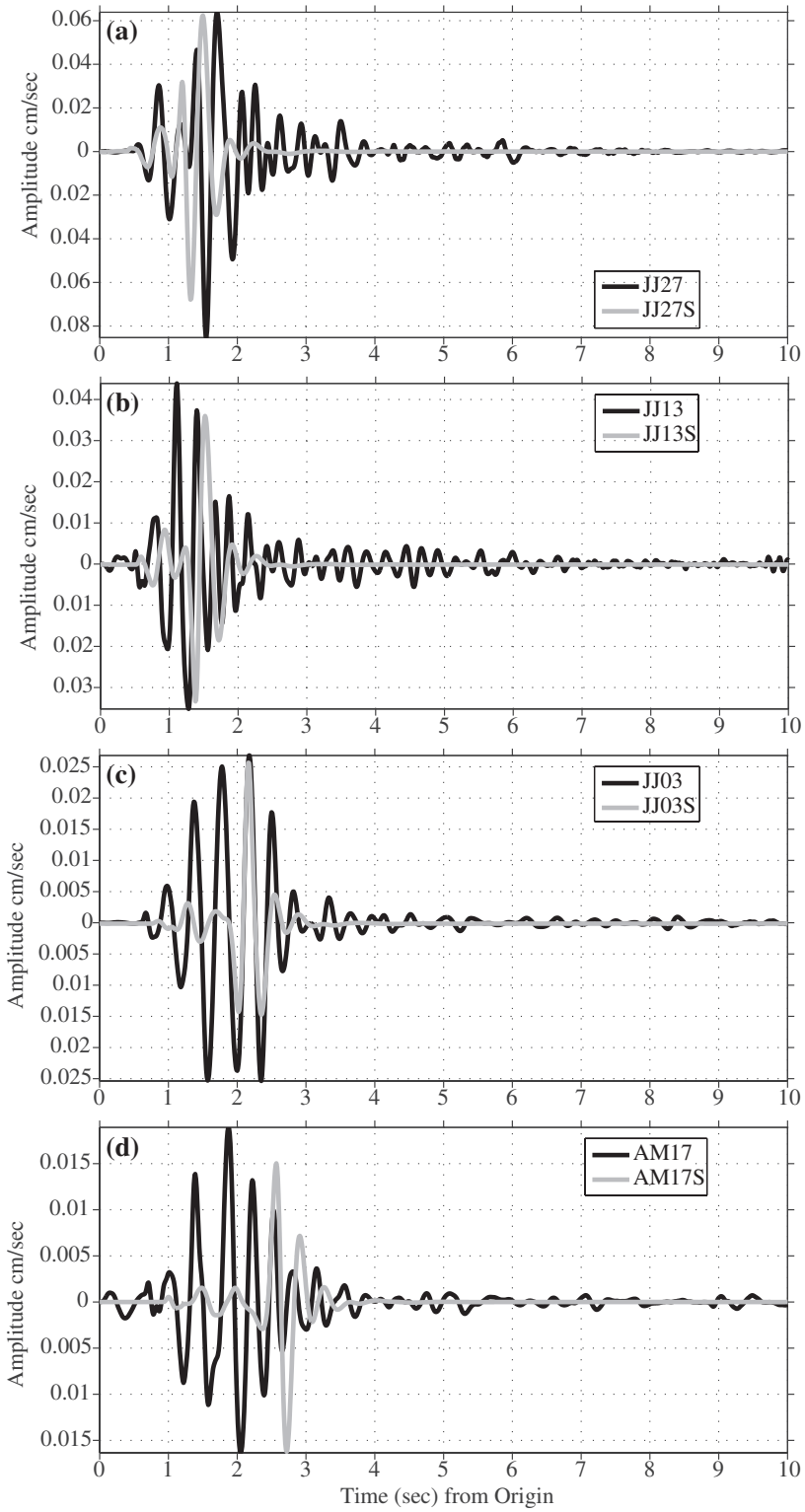

Figure 19. Observed vs. synthetic seismograms for shots 4 & 5 1-D models. Examples from the NW (a), SE (b), NE (c), and N (d) models are shown. The four digit letter/number combination is the name of the Texan station, and the "S" indicates synthetic.

VII. 3-D Velocity Model

In order to better illustrate the variations in P- and S-wave velocity both laterally and with depth throughout the Goldstream Valley, three 3-D velocity models of the upper crust are developed; one for each shot group. These 3-D velocity models are produced using the Wave Propagation Program (WPP) developed by *Appelö et al.* (2007), which runs on a WGC parallel computing cluster. This program simulates time-dependent viscoelastic wave propagation using a node-based finite difference approach on a Cartesian grid (*Appelö et al.*, 2007). The starting block model for each WPP simulation is developed with the 1-D refraction and inversion results for that shot group and consists of a base model overlain by four regional models. The base model is an average of the velocity model results for each region and covers the entire areal extent of the modeled area, which is a 17 km x 17 km region encompassing all of the Texan and near-source instruments, along with four of the broadband stations (FOX, MDR, PED, and WFR) (Figure 20). The regional models are the actual 1-D velocity models for each of the NW, SE, NE, and N regions. The location of each regional model is selected by eye and is based on the Texan station layout. WPP compiles the base model and the regional models to create a 3-D model.

The resultant 3-D velocity models extend to a depth of 2 km, with the greatest resolution in the upper 1 km of the crust. Two dimensional cross-sections of the P- and S-wave velocity models are taken through the center of the modeled area in the north-south (N-S) and east-west (E-W) directions to illustrate the general features of the 3-D models (Figures 21-23). These cross-sections show that in the immediate vicinity of the

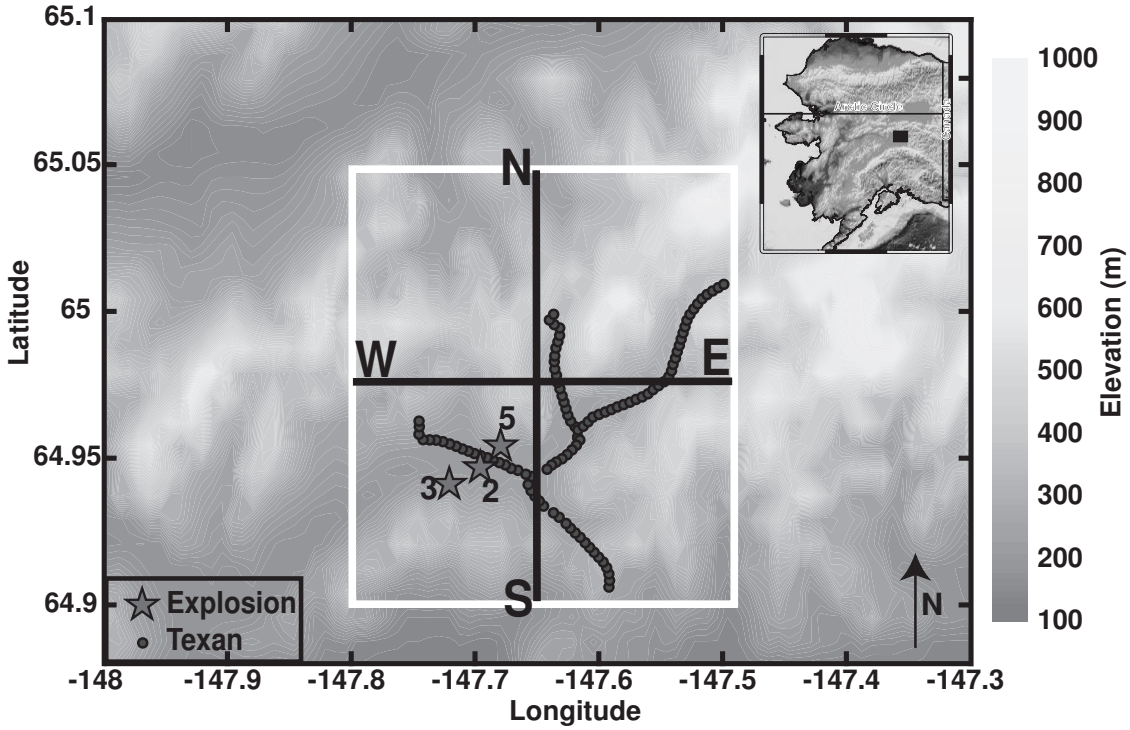

Figure 20. Map of WPP modeled area. The 17 km x 17 km modeled region (white box) includes all Texan (black dots) and near source stations, along with broadband stations FOX, MDR, WFR, and PED (not shown here; see Figures 1a,c). Three different source locations (grey stars) were used to generate three different 3-D models. The locations of the N-S and E-W 2-D cross-sections of the 3-D velocity models in Figures 21-23 are indicated. Modified from *Leidig et al.* (2006a).

source location, especially to the west of the source, both P- and S-wave velocities are slow compared to those found at other areas across the length of the model. These slow velocities are likely indicative of the glacial deposits and frozen gravels located in the vicinity of the PMI gold mine, where shots 1-3 were detonated. Additionally, the velocities found for each 3-D model below 1 km depth are nearly constant throughout the region, illustrating the low resolution of the models at these depths. P- and S-wave velocities at depths of 1-2 km in these models are ~6 km/s and ~3.5 km/s, respectively.

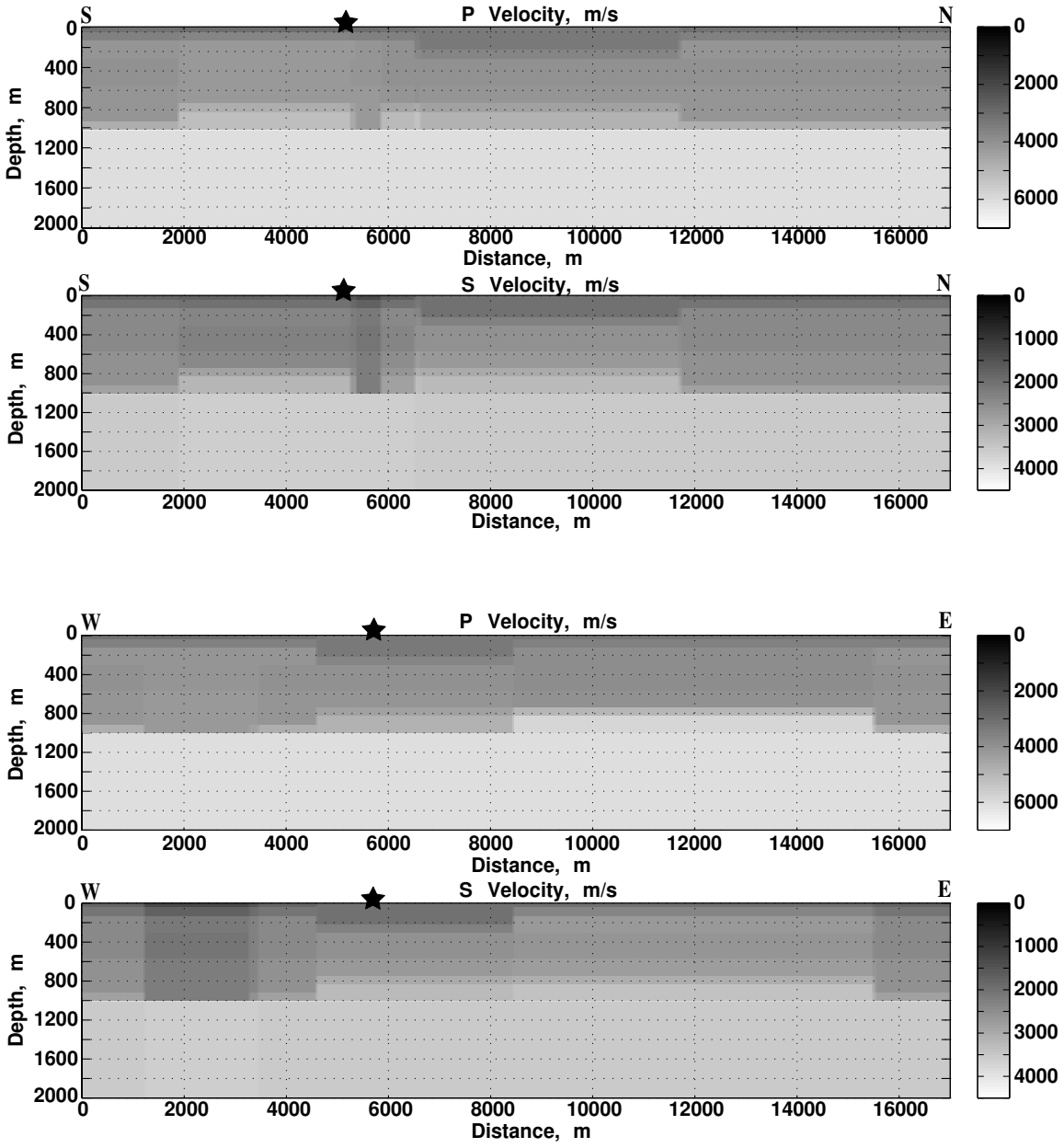

Figure 21. 2-D velocity model slices for shots 1 & 2 data. (Top) North-South P- and S-wave velocity cross-sections of 3-D WPP model. (Bottom) East-West P- and S-wave velocity cross-sections. Darker shading indicates lower velocity. Source location is indicated by star. See Figure 20 for locations of cross-sections.

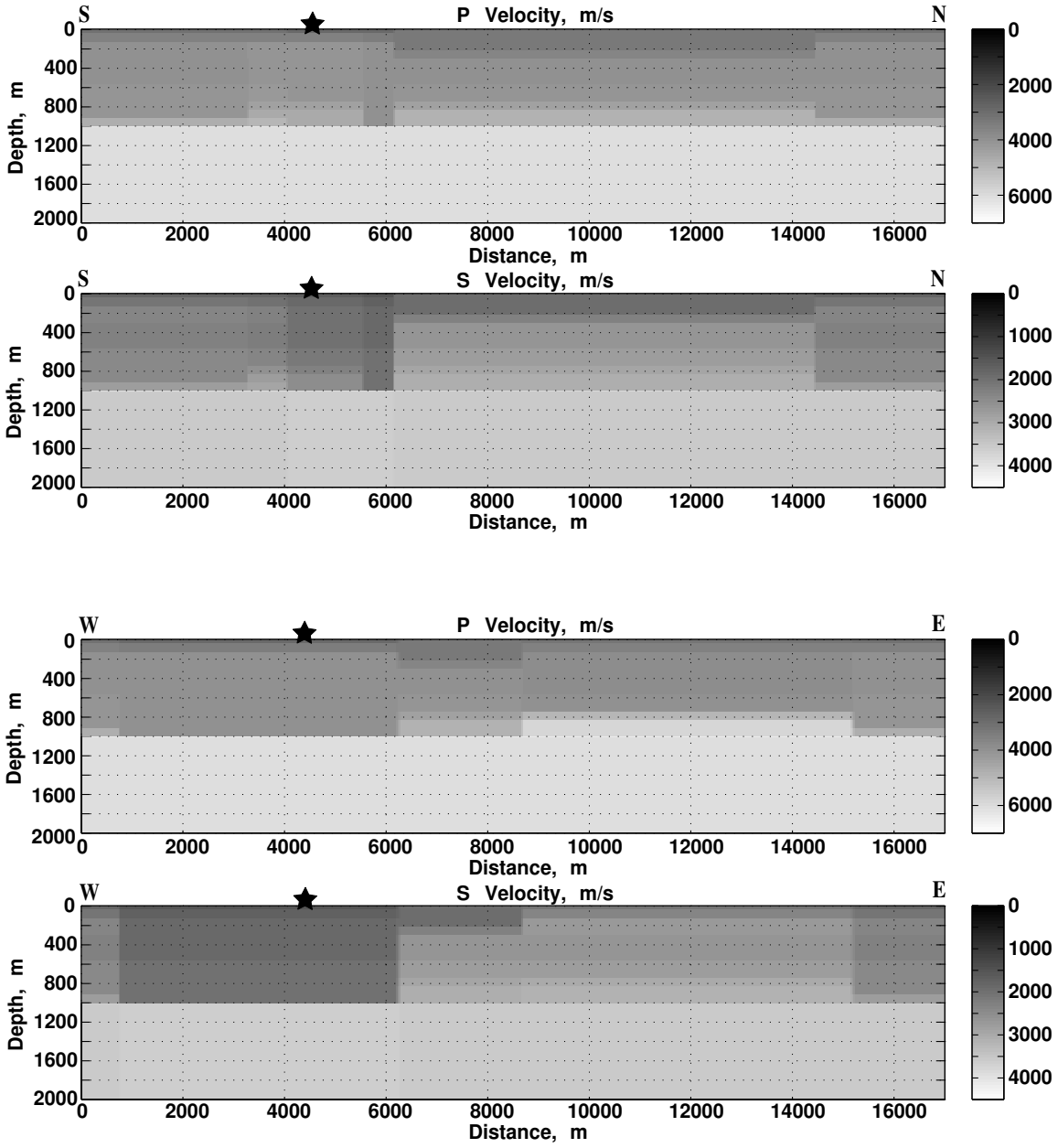

Figure 22. 2-D velocity model slices for shot 3 data. (Top) North-South P- and S-wave velocity cross-sections of 3-D WPP model. (Bottom) East-West P- and S-wave velocity cross-sections. Darker shading indicates lower velocity. Source location is indicated by star. See Figure 20 for locations of cross-sections.

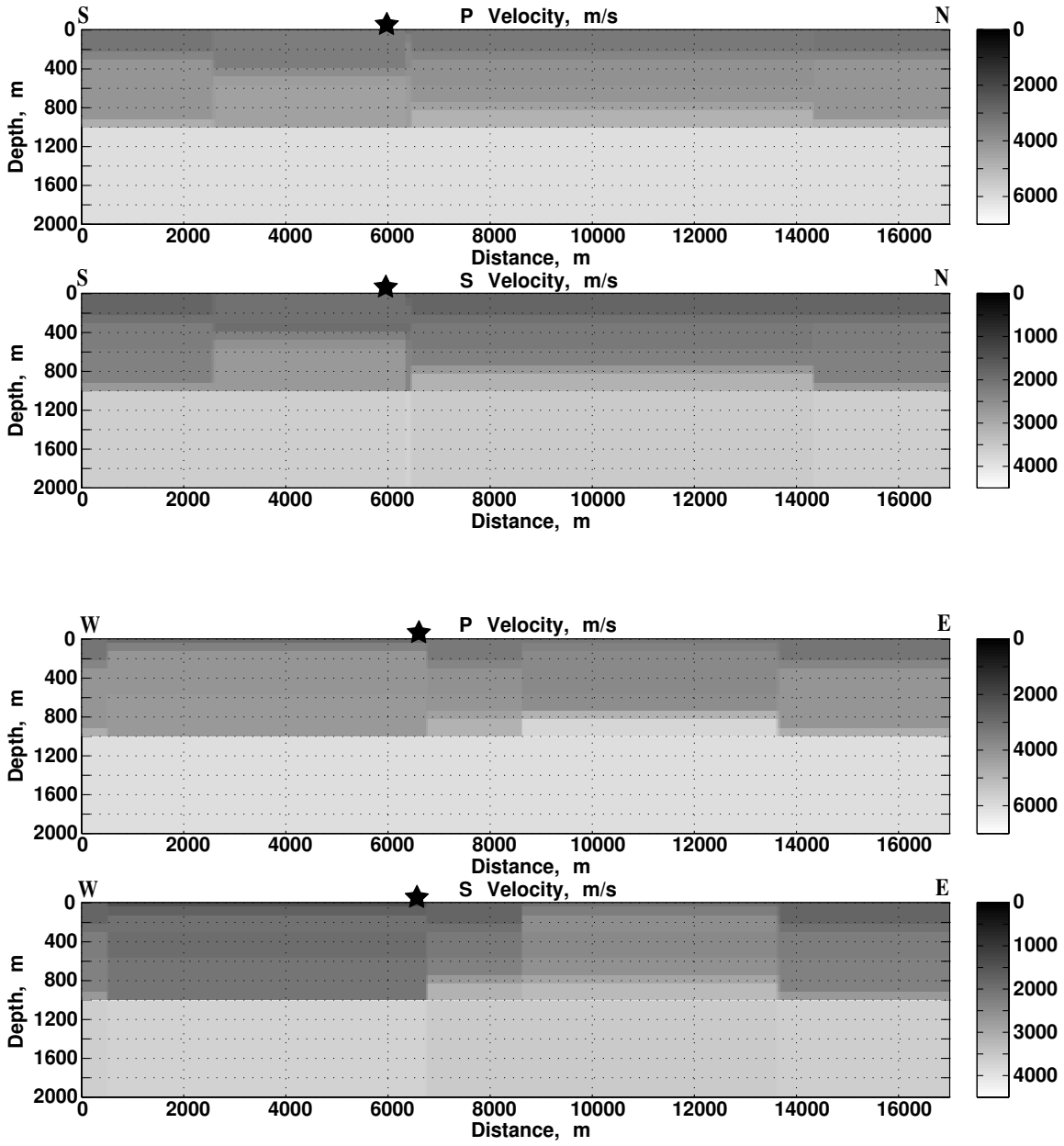

Figure 23. 2-D velocity model slices for shots 4 & 5 data. (Top) North-South P- and S-wave velocity cross-sections of 3-D WPP model. (Bottom) East-West P- and S-wave velocity cross-sections. Darker shading indicates lower velocity. Source location is indicated by star. See Figure 20 for locations of cross-sections.

Each WPP simulation uses the resultant 3-D upper crustal velocity model and an isotropic source whose geographic location and seismic moment is that of the largest shot

in that group (i.e. shots 2, 3, and 5) to generate synthetic seismograms for a sample of 31 of the seismic stations. This sample includes 6 near-source, 5 broadband, and 20 Texan stations. The selected Texans are distributed throughout all four geographic regions and give good areal coverage. Body and surface wave phases from these synthetic seismograms are compared with the observed data and differences are discussed.

Comparisons of observed and synthetic seismograms for each of the 3-D velocity models are shown in Figures 24 (shots 1 & 2), 25 (shot 3), and 26 (shots 4 & 5). Each of these figures presents a comparison for four different Texan stations, one from each of the regions analyzed in this study. All seismograms presented in these figures have been bandpass filtered between 0.5 Hz and 2 Hz using a 5^{th} order zero-phase Butterworth filter in order to highlight the surface waves. It is clear from these figures that the predicted surface waves at most stations are more dispersed than was recorded and do not contain the large amplitude ringing at the tail of the seismogram that is evident in the recorded data. As was noted in the discussion of the synthetics produced for the 1-D models, the addition of more low velocity layers near the surface of the 3-D models could result in the reproduction of the observed ringing in the synthetic waveforms. In terms of body waves, for all three models, the recorded P-wave arrives after it is predicted at all stations for which picks could be made, but the amplitude of the arrival is consistent between the observed and synthetic data. Since the synthetics are generated using an isotropic source, no S-wave arrivals are expected and none were clearly observed in the synthetic waveforms, so no comparison between recorded and predicted S-waves can be made.

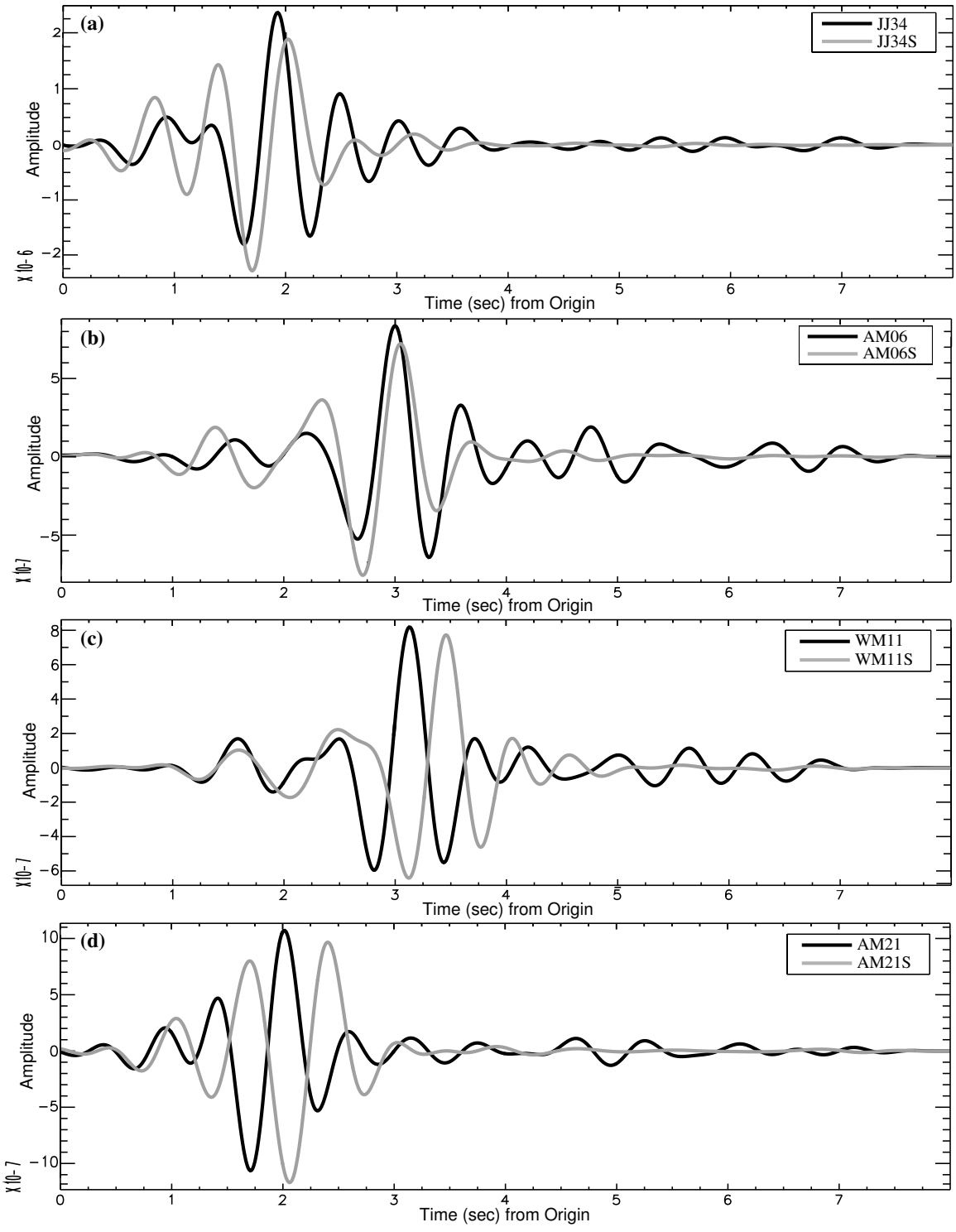

Figure 24. Observed vs. synthetic seismograms for shots 1 & 2 3-D velocity model. Comparison of shot 2 recordings (black) and synthetic waveforms (grey) for a NW (a), SE (b), NE (c), and N (d) Texan station are shown. All signals have been bandpass filtered between 0.5 and 2 Hz.

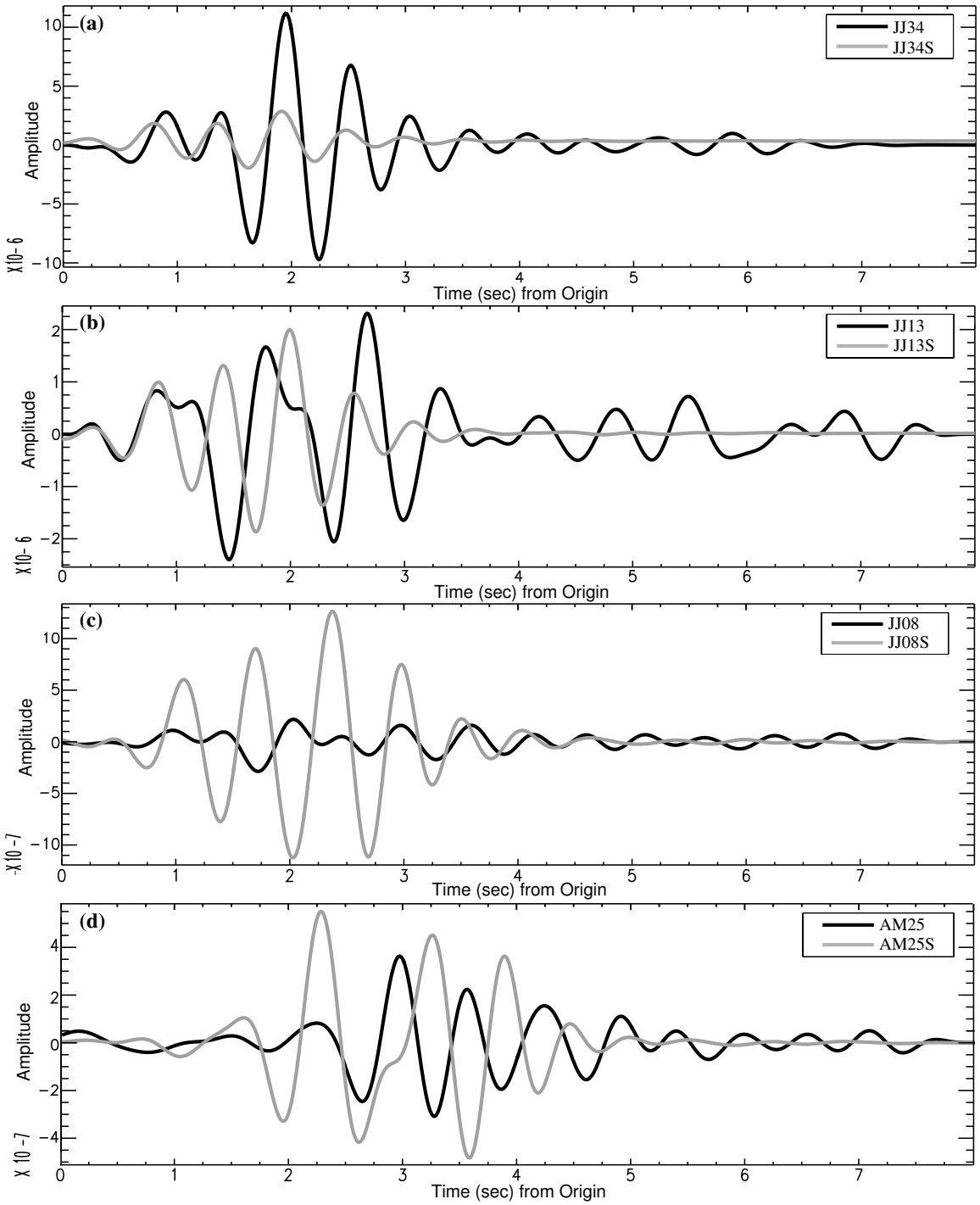

Figure 25. Observed vs. synthetic seismograms for shot 3 3-D velocity model. Comparison of shot 3 recordings (black) and synthetic waveforms (grey) for a NW (a), SE (b), NE (c), and N (d) Texan station are shown. All signals have been bandpass filtered between 0.5 and 2 Hz.

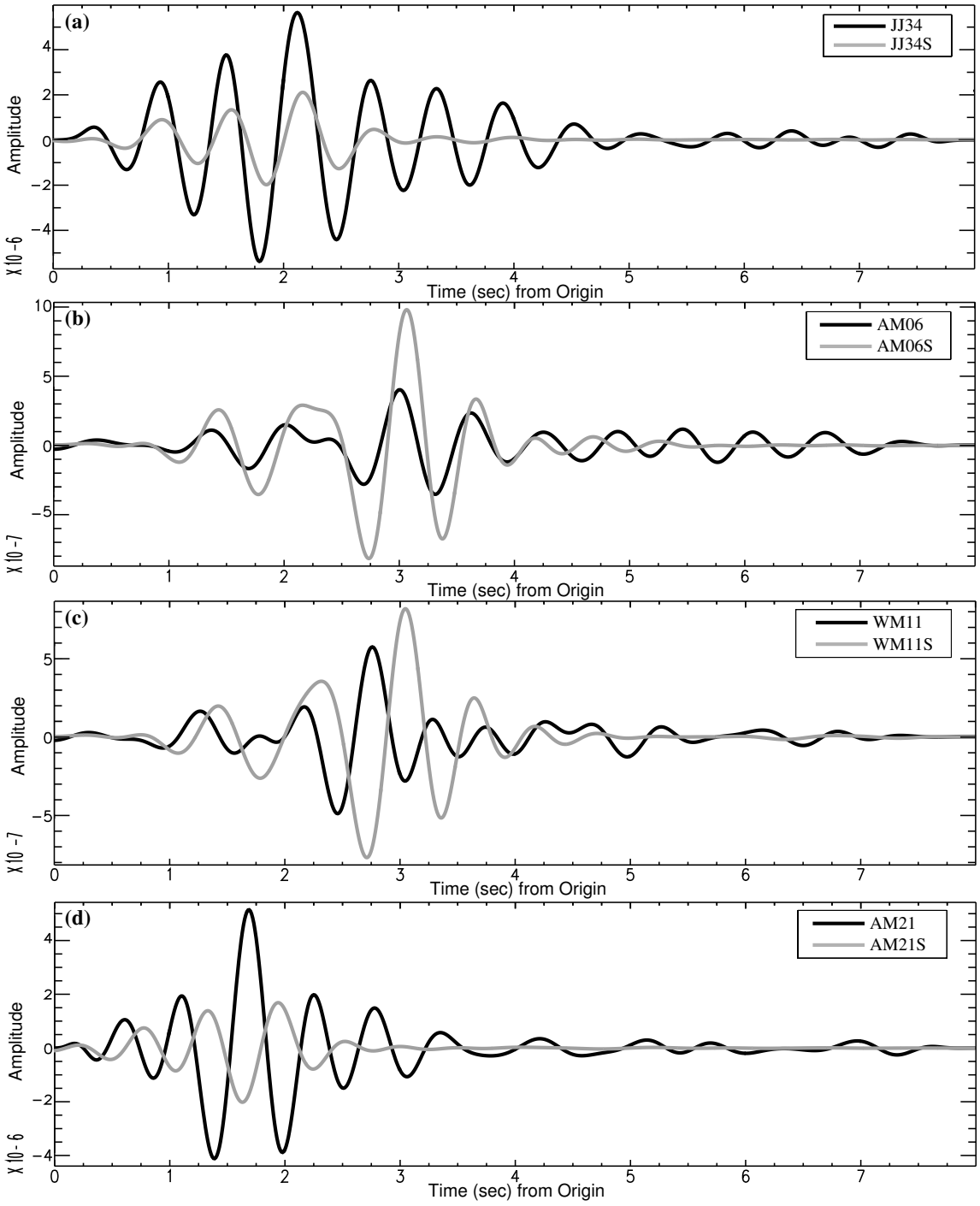

Figure 26. Observed vs. synthetic seismograms for shots 4 & 5 3-D velocity model. Comparison of shot 5 recordings (black) and synthetic waveforms (grey) for a NW (a), SE (b), NE (c), and N (d) Texan station are shown. All signals have been bandpass filtered between 0.5 and 2 Hz.

VIII. Discussion

The regional geology of the Goldstream Valley is comprised of the 1200 m thick metasedimentary Fairbanks schist unit, overlain by 10 m to >100 m of Quaternary surficial deposits of unconsolidated sand, gravel, and glacial loess (Figure 27; *Combellick and Bundtzen*, 1996; *Foster et al.,* 1994; *Robinson et al.,* 1990; *Wilson et al.,* 1998). As has already been noted, this area of central Alaska is also transected by several high angle northeast trending faults (Figure 27; *Newberry et al.,* 1996; *Robinson et al.,* 1990). The relationships between the mapped geology and the seismic results of this study are discussed in terms of each Texan region (i.e. NW, N, NE, and SE) in the following.

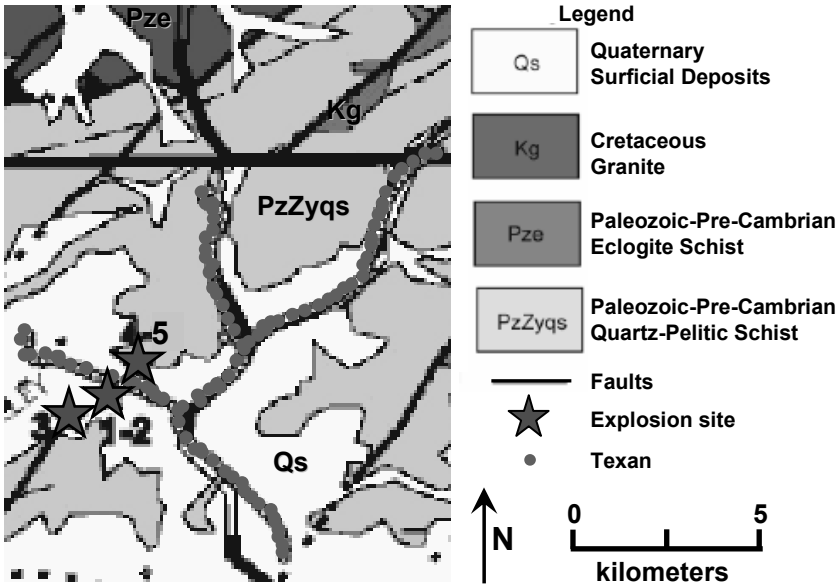

Figure 27. Local geologic map of the Goldstream Valley. Northeast-trending faults are indicated, along with explosion sites and Texan locations. The NW, N, NE, and SE Texan regions are depicted in Figures 28-31, respectively. Modified from *Bonner and Leidig* (2007). Original map from *Wilson et al.* (1998).

The NW region is located completely within the valley and is therefore dominated by the Quaternary deposits at the surface, with minimal quartz-pelitic schist bedrock

exposure (Figure 28). Two northeast trending faults are visible in this region; one to the southwest of shot site 3 (solid line) and one below the surface (dashed line) near the bend in the seismic line (Figure 28). The 1-D velocity model results for this region for all shot groups reveal P- and S-wave velocities of 2.75-2.92 km/s and 1.18-1.39 km/s, respectively, for the upper 60 m (Tables 3-5). At this shallow depth, the mapped lithology is the unconsolidated Quaternary deposits. The measured S-wave velocities are consistent with the known velocity range for this lithology, while the measured P-wave velocities meet or exceed the high end of the known velocity range (Table 7). These high P-wave velocities indicate the possible presence of fractured bedrock near the base of this upper layer. The Poisson ratio (σ) values calculated for this upper layer range from 0.328 to 0.402 (Tables 3-5), indicating soft, poorly consolidated material, which is consistent with the mapped Quaternary deposits and possibility of fractured bedrock. At depths of 60 m to 400 m, P-wave velocities of 3.81-3.98 km/s and average S-wave velocities of 1.50-1.64 km/s are found (Tables 3-5). In this depth range, the mapped lithology grades

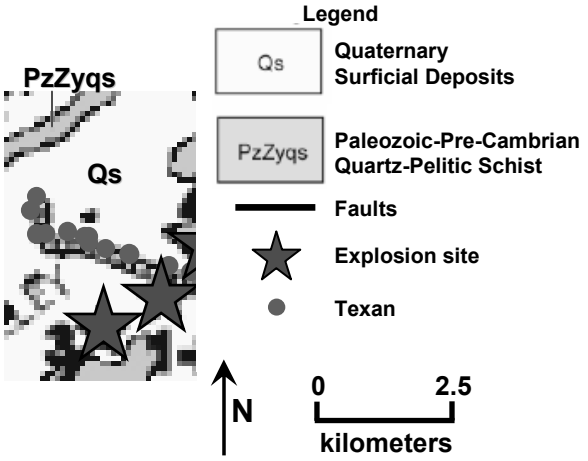

Figure 28. Local geologic map for NW region. Northeast-trending faults are indicated, along with explosion sites and Texan locations. Refer to Figure 27 for view of all regions. Modified from *Bonner and Leidig* (2007). Original map from *Wilson et al.* (1998).

Table 7. Typical Velocities for Regional Rock Types

Rock Type	α, km/s	β, km/s	Pressure measured at, MPa	Approx. depth, km*	Source
mica-qtz schist	5.35	3.06	10	0.35	*Brocher et al.,* 2004
	6.27 ± 0.31	3.53 ± 0.23	200	7	*Christensen,* 1996
	6.16 ± 0.35		140	5	*Christensen and Mooney,* 1995
	4.25 - 5.77	2.73 - 3.51	10	0.35	*Brocher et al.,* 1991
	5.70		1	0.04	*Birch*, 1960
pelitic schist	6.33	3.52 - 3.92	150	5.3	*Takanashi et al.,* 2001
(amphibolite)	6.43 - 6.98	3.61 - 3.96	600	21	*Christensen,* 1996
		3.20	10	0.35	*Christensen,* 1966
	5.50 - 5.80		10	0.35	*Christensen,* 1965
pelitic schist (greenschist)	6.32	3.57	500	17.5	*Christensen,* 1996
mica-quartzite	4.40	2.75	10	0.35	*Brocher et al.,* 2004
		3.50	10	0.35	*Christensen,* 1966
	5.20		10	0.35	*Christensen,* 1965
quartzite	5.96 ± 0.07	4.04 ± 0.05	200	7	*Christensen,* 1996
	5.89 ± 0.08		140	5	*Christensen and Mooney,* 1995
		3.60	10	0.35	*Christensen,* 1966
	5.50 - 5.70		10	0.35	*Christensen,* 1965
	5.60		1	0.04	*Birch*, 1960
gneiss	5.49	3.10 - 3.41	150	5.3	*Takanashi et al.,* 2001
	6.18 ± 0.19	3.55 ± 0.17	200	7	*Christensen,* 1996
	6.11 ± 0.21		140	5	*Christensen and Mooney,* 1995
		2.70 - 3.10	10	0.35	*Christensen,* 1966
	4.50 - 5.60		10	0.35	*Christensen,* 1965
	3.40 - 5.10		1	0.04	*Birch*, 1960
	5.67 - 6.06		50	1.8	*Birch*, 1960
Quaternary	2.00 ± 0.50		N/A	surficial	*Sheriff and Geldart,* 1995
glacial deposits	1.70 - 2.10	0.60 - 1.60	N/A	surficial	*Brocher et al.,* 1991
	1.85 - 2.85		N/A	surficial	*Fuis et al.,* 1991

*Depth calculated using 1 GPa = 35 km approximation

from the unconsolidated Quaternary deposits to the Fairbanks schist unit. The measured shear-wave velocities remain consistent with the known velocities for the Quaternary deposits, yet the measured P-wave velocities lie within the range of known velocities found for shallow gneiss (Table 7). As noted before, the Fairbanks schist unit is comprised mainly of interlensing pelitic schist, mica-quartz schist, micaceous quartzite,

and large gneiss dome complexes (*Foster et al.,* 1994; *Robinson et al.,* 1990; *Wilson et al.,* 1998). Additionally, *Bonner and Leidig* (2007) and *Bonner et al.* (2007) noted the presence of gneiss and schist in the valley. Therefore, the measured P-wave velocities are consistent with the known lithology in this depth range. The Poisson ratios calculated for this depth range yield average values of 0.382-0.416 (Tables 3-5). These high values indicate the presence of poorly consolidated material, which is consistent with the Quaternary deposits, but not consistent with the gneiss. It is known that an increase in σ can be the result of either an increase in P-wave velocity or a decrease in S-wave velocity (*Holbrook et al.,* 1992), so it is likely that the low S-wave velocities observed in this layer are controlling the high Poisson ratio values. At depths of 400 m to 1.0 km, P-wave velocities of 5.01-5.08 km/s and average S-wave velocities of 2.20-2.35 km/s are observed (Tables 3-5). The Fairbanks schist unit is the only mapped geologic unit present at these depths. The measured P-wave velocities are correlated with known velocities for shallow gneiss, mica-quartzite, and mica-quartz schist (Table 7), all of which are contained within the Fairbanks schist. The measured S-wave velocities are not consistent with the velocities of any of the lithologies known to be present in the Goldstream Valley. The observed shear-wave velocities are higher than those for Quaternary deposits and lower than those for gneiss, mica-quartzite, and mica-quartz schist (Table 7). It is possible that these low S-wave velocities are the result of fractured bedrock, possibly due to the two faults mapped in the NW region (Figure 28). The average Poisson ratios calculated for the depth range of 400 m to 1.0 km are 0.349-0.380 (Tables 3-5). As with the two layers above 400 m depth, the high Poisson ratio values

found for this layer indicate the presence of soft, poorly consolidated material, which is consistent with the possibility of fractured bedrock due to faulting. At depths of 1.0 km to 2.0 km, average S-wave velocities of 2.89-3.25 km/s are found (Tables 3-5). The P-wave velocity at this depth range is taken from the CRUST 2.0 reference earth model (*Laske et al.,* 2001), which yields a value of 6.00 km/s among all regions of the Goldstream Valley (Tables 3-5). The measured S-wave velocities are correlated with known velocities for mica-quartz schist, mica-quartzite, and gneiss (Table 7), all of which are present in the Fairbanks schist unit mapped at these depths. The P-wave velocity of 6.00 km/s is not interpreted in terms of lithology since this value holds for all regions and is not a local determination from the FRE data. The average calculated Poisson ratios in this lowermost layer of the 1-D velocity models range from 0.274-0.342 (Tables 3-5). These Poisson ratios are calculated using the CRUST 2.0 P-wave velocity of 6.00 km/s, which is not specific to the NW region, so interpretations of these Poisson ratio values in terms of local geology cannot be made. The high Poisson ratios observed in the three overlying layers indicate less consolidated material is present in the upper 1.0 km of the NW region. In addition to the possible presence of fractured bedrock due to faulting in the region, it is possible that the area traversed by the seismic raypaths between the sources and the NW receivers has been extensively reworked by mining due to the close proximity of the NW line of Texans to the gold mine where shots 1-3 were detonated. This reworking would result in a decrease in the consolidation of the rocks in this area, producing the higher Poisson ratios observed.

The N region is located partially within the valley, with the northernmost Texan stations located at higher elevations (Figure 29). At the surface, the geology of this region consists of Quaternary deposits in the low-lying valley and quartz-pelitic schist bedrock at higher elevations, with two northeast trending faults located north of the line of Texans (Figure 29). The 1-D velocity model results for all shot groups in this region

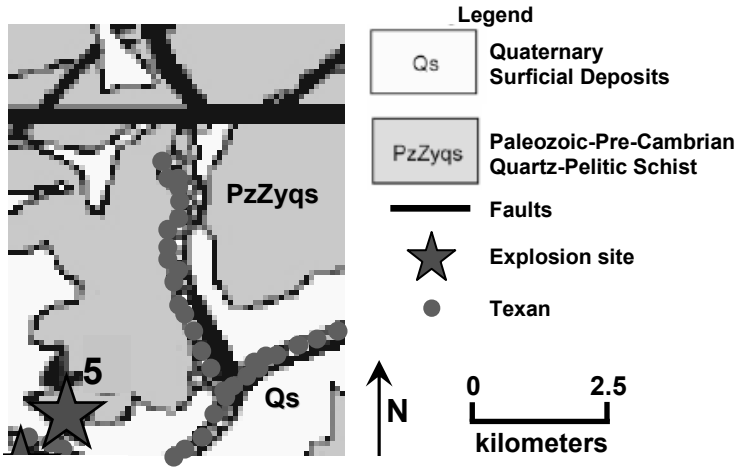

Figure 29. Local geologic map for N region. Northeast-trending faults are indicated, along with explosion sites and Texan locations. Refer to Figure 27 for view of all regions. Modified from *Bonner and Leidig* (2007). Original map from *Wilson et al.* (1998).

reveal P- and S-wave velocities of 3.18 km/s and 1.65-1.82 km/s, respectively, for the upper 100 m of the crust (Tables 3-5). Both the observed P- and S-wave velocities exceed the range of measured velocities for the Quaternary deposits known to be present to depths of up to 100 m or more (Table 7). These observed velocities are also lower than the measured velocities for all other rock types known to be present in the Goldstream Valley, but are most closely correlated with measured velocities for shallow gneiss (Table 7). The observed P- and S-wave velocities, therefore, may be the result of

interlensing Quaternary deposits and gneiss in the upper 100 m with no laterally continuous lithological boundaries. Alternatively, the observed S-wave velocities may be the result of an averaging of velocities for Quaternary deposits and underlying gneiss, as the minimum Rg wavelengths measured for the N region range from 190 km to 345 km. These minimum wavelengths indicate that the S-wave velocities determined from the inversion of Rg dispersion curves in this region are average values for the upper 190-345 km of the crust. The Poisson ratio values calculated for this upper layer range from 0.256 to 0.316 (Tables 3-5) and are indicative of mica-quartz schist and/or pelitic schist (Table 8) that may be fractured due to faulting and/or accompanied by less consolidated material, such as the Quaternary deposits. Alternatively, these Poisson ratios could also

Table 8. Typical Poisson Ratios for Regional Rock Types

Rock Type	σ	Pressure measured at, MPa	Approx. depth, km*	Source
mica-quartz schist	0.26	10	0.35	*Brocher et al.*, 2004
	0.268 ± 0.054	200	7	*Christensen*, 1996
pelitic schist (amphibolite)	0.270	600	21	*Christensen*, 1996
pelitic schist (greenschist)	0.266	500	17.5	*Christensen*, 1996
mica-quartzite	0.18-0.24	10	0.35	*Brocher et al.*, 2004
gneiss	0.21	10	0.35	*Brocher et al.*, 2004

*Depth calculated using 1 GPa = 35 km approximation

indicate the presence of interlensing Quaternary deposits and gneiss, as discussed above, with Poisson ratio values that are greater than those measured for gneiss (Table 8), but less than those expected for the poorly consolidated Quaternary deposits alone. At depths of 100 m to 300 m, a P-wave velocity of 3.86 km/s and average S-wave velocities of 2.01-2.45 km/s are found (Tables 3-5). In this depth range, the mapped geology consists entirely of the Fairbanks schist unit. The observed P-wave velocity is consistent with

known velocities for shallow gneiss, yet the observed S-wave velocities are slower than the gneiss values and not correlated with any other lithology known to be present (Table 7). These low S-wave velocities could be indicating that the gneiss in this region is highly fractured due to faulting. The Poisson ratios calculated for this depth range yield average values of 0.162 to 0.314 (Tables 3-5), which are consistent with the measured values for all rock types known to comprise the Fairbanks schist unit (Table 8), including gneiss. At depths of 300 m to 900 m, a P-wave velocity of 4.55 km/s and average S-wave velocities of 2.42-2.64 km/s are observed (Tables 3-5). The Fairbanks schist unit is the only mapped geologic unit present at these depths. The measured P-wave velocity is consistent with known velocity values for mica-quartz schist, micaceous quartzite, and gneiss (Table 7), all of which are present in the Fairbanks schist. The measured S-wave velocities are slightly lower than the known velocities for each of these lithologies (Table 7), possibly indicating that the bedrock is fractured. Average Poisson ratio values calculated for this depth range are 0.241-0.295 (Tables 3-5). These values are consistent with measurements for micaceous quartzite, mica-quartz schist, and pelitic schist (Table 8). When the Poisson ratio values are coupled with the observed P-wave velocity, it can be concluded that the lithology in this depth range is likely mica-quartz schist and/or micaceous quartzite. At depths of 900 m to 2.0 km, average S-wave velocities of 3.21-3.33 km/s are found, while the P-wave velocity is 6.00 km/s (from CRUST 2.0) (Tables 3-5). As was noted for the NW region, this P-wave velocity is not interpreted in terms of lithology since this value holds for all regions and is not a local determination from the FRE data. The observed S-wave velocities are correlated with measurements for mica-

quartz schist, amphibolite grade pelitic schist, mica-quartzite, and gneiss (Table 7). The average calculated Poisson ratios in this lowermost layer of the 1-D velocity models range from 0.274-0.294 (Tables 3-5). These Poisson ratios are calculated using the CRUST 2.0 P-wave velocity of 6.00 km/s, which is not specific to the N region, so interpretations of these Poisson ratio values in terms of local geology cannot be made.

The NE region is located mostly within the valley, with the northernmost third of the Texan stations located at higher elevations (Figure 30). The surficial geology of this region consists primarily of unconsolidated Quaternary deposits in the valley and quartz-pelitic schist bedrock exposed at the higher elevations (Figure 30). Two northeast trending faults are also present in the region; one to the northwest and one to the southeast of the NE line of Texans (Figure 30). The 1-D velocity model results for this region for all shot groups reveal P- and S-wave velocities of 3.09-3.17 km/s and 1.80-1.86 km/s, respectively, for the upper 70 m (Tables 3-5). At this shallow depth, the

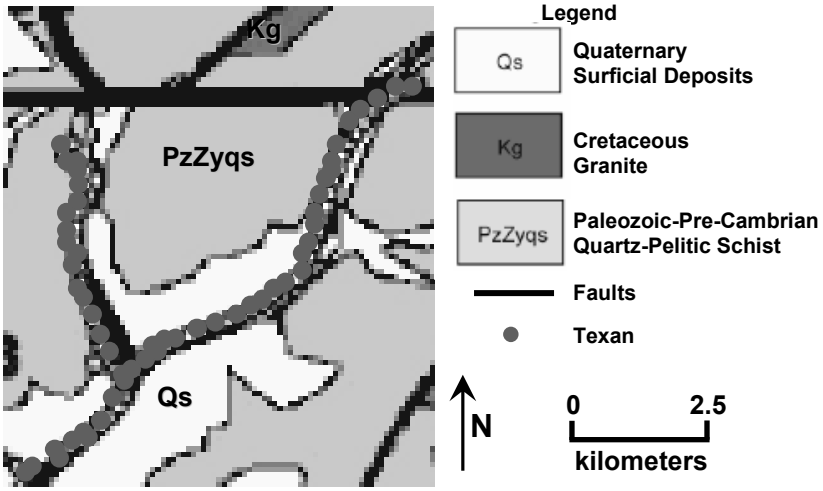

Figure 30. Local geologic map for NE region. Northeast-trending faults are indicated, along with explosion sites and Texan locations. Refer to Figure 27 for view of all regions. Modified from *Bonner and Leidig* (2007). Original map from *Wilson et al.* (1998).

mapped lithology is the Quaternary deposits. Both the measured P- and S-wave velocities exceed the range of known velocities for Quarternary deposits and are lower than the measured velocities for any other rock type known to be present in the Goldstream Valley, but are closest to the known velocities for shallow gneiss (Table 7). As with the upper layer in the N region, these observed velocities could indicate the presence of interlensing Quaternary deposits and gneiss with no laterally continuous lithological boundaries. Alternatively, the observed S-wave velocities may be the result of an averaging of velocities for Quaternary deposits and underlying gneiss, as the minimum Rg wavelengths measured for the NE region range from 186 km to 398 km. These minimum wavelengths indicate that the S-wave velocities determined from the inversion of Rg dispersion curves in this region are average values for the upper 186-398 km of the crust. The Poisson ratio values calculated for this upper layer range from 0.216 to 0.289 (Tables 3-5) and are consistent with measurements for all rock types known to be present in the Fairbanks schist unit (Table 8), but are lower than would be expected for unconsolidated Quarternary deposits. These Poisson values support the idea of interlensing Quaternary deposits and gneiss. At depths of 70 m to 300 m, P-wave velocities of 3.68-3.76 km/s and average S-wave velocities of 2.13-2.23 km/s are found (Tables 3-5). In this depth range, the mapped lithology grades from the unconsolidated Quaternary deposits to the Fairbanks schist unit. The observed P-wave velocities are consistent with known values for shallow gneiss, while the observed S-wave velocities are uncorrelated with measured values for any lithology known to be present, but lie between the measured velocities for Quaternary deposits and those for gneiss (Table 7).

These low S-wave velocities could be indicating that the gneiss in this region is highly fractured due to faulting. The Poisson ratios calculated for this depth range yield average values of 0.203 to 0.237 (Tables 3-5), which are consistent with measurements for gneiss and mica-quartzite lithologies (Table 8). Based on the observed velocities and calculated Poisson ratios, it can be concluded that the dominant lithology in this depth range is gneiss. At depths of 300 m to 900 m, P-wave velocities of 5.51-5.57 km/s and average S-wave velocities of 2.59-2.76 km/s are observed (Tables 3-5). The Fairbanks schist unit is only the mapped lithology at depths below 300 m. The measured P-wave velocities are correlated with known velocities for mica-quartz schist, amphibolite grade pelitic schist, quartzite, and gneiss (Table 7). The measured S-wave velocities are consistent with known values for mica-quartz schist, mica-quartzite, and gneiss (Table 7). Average Poisson ratio values for this depth range are 0.335-0.356 (Tables 3-5), which exceed all measurements for lithologies known to be present in the Fairbanks schist (Table 8). These Poisson ratios are very high for bedrock, but the combined P- and S-wave velocities indicate the presence of mica-quartz schist and/or gneiss in this layer. It is possible that these high Poisson ratios are the result of fractured mica-quartz schist and/or gneiss. At depths of 900 m to 2.0 km, average S-wave velocities of 3.28-3.36 km/s are found, while the P-wave velocity is 6.00 km/s (from CRUST 2.0) (Tables 3-5). As was noted for the NW and N regions, this P-wave velocity is not interpreted in terms of lithology since this value holds for all regions and is not a local determination from the FRE data. The observed S-wave velocities are consistent with measurements for mica-quartz schist, amphibolite grade pelitic schist, mica-quartzite, and gneiss (Table 7). The

average calculated Poisson ratios in this lowermost layer of the 1-D velocity models range from 0.268-0.282 (Tables 3-5). These Poisson ratios are calculated using the CRUST 2.0 P-wave velocity of 6.00 km/s, which is not specific to the NE region, so interpretations of these Poisson ratio values in terms of local geology cannot be made.

The SE region is located entirely within the valley, with a surficial geology dominated by unconsolidated Quaternary deposits (Figure 31). Minimal quartz-pelitic schist bedrock exposure is present in the region, along with a subsurface (dotted line) northeast trending fault located at the southeastern end of the Texan line (Figure 31). The 1-D velocity model results for this region for all shot groups reveal P- and S-wave

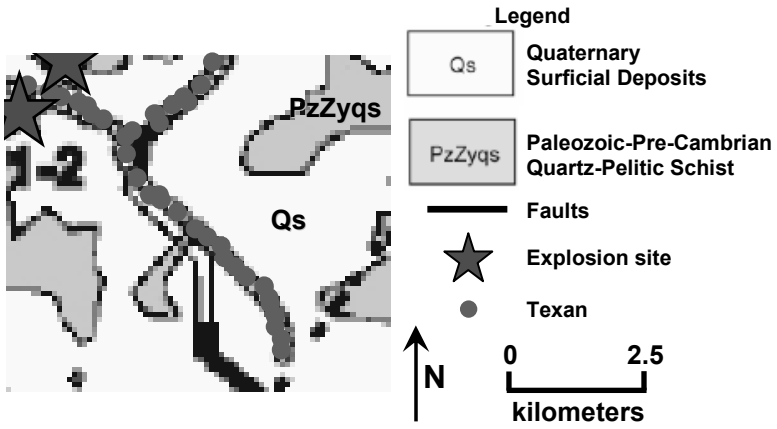

Figure 31. Local geologic map for SE region. Northeast-trending faults are indicated, along with explosion sites and Texan locations. Refer to Figure 27 for view of all regions. Modified from *Bonner and Leidig* (2007). Original map from *Wilson et al.* (1998).

velocities of 2.92-3.31 km/s and 1.55-1.64 km/s, respectively, for the upper 50 m (Tables 3-5). At this shallow depth, the mapped lithology is the Quaternary deposits. The measured P-wave velocities exceed the range of known velocities for Quaternary deposits and are lower than the known velocities for any other lithology present in the Goldstream

Valley (Table 7). The measured S-wave velocities, however, are correlated with known values for Quaternary deposits (Table 7). The calculated Poisson ratios for this upper layer yield values ranging from 0.293 to 0.330 (Tables 3-5), which exceed all measurements for Fairbanks schist lithologies (Table 8), indicating softer, less consolidated material, such as the Quaternary deposits. At depths of 50 m to 300 m, average P- and S-wave velocities of 3.60-4.03 km/s and 1.76-2.23 km/s, respectively, are found (Tables 3-5). In this depth range, the mapped lithology grades from the unconsolidated Quaternary deposits to the Fairbanks schist unit. The observed P-wave velocities are consistent with known values for gneiss, while the observed S-wave velocities are higher than those expected for Quaternary deposits and lower than those for gneiss (Table 7). It is possible that these S-wave velocities are indicating the gradational change in lithologies from Quaternary deposits at shallower depths to gneiss at greater depths. The average Poisson ratio values for this depth range are 0.286-0.380 (Tables 3-5). These Poisson ratios surpass the measurements for all lithologies of the Fairbanks schist unit (Table 8) and are consistent with Quaternary deposits or highly fractured bedrock. At depths of 300 m to 1.0 km, average P- and S-wave velocities of 4.81-4.91 km/s and 2.40-2.72 km/s, respectively, are found (Tables 3-5). Below 300 m depth, the only mapped lithology is the Fairbanks schist unit. Both the measured P- and S-wave velocities are consistent with known velocities for mica-quartz schist, mica-quartzite, and gneiss (Table 7). The Poisson ratios calculated for this layer yield average values of 0.286-0.336 (Tables 3-5), which again exceed measurements for Fairbanks schist unit lithologies (Table 8) and could indicate the presence of highly fractured bedrock. At

depths of 1.0 km to 2.0 km, average S-wave velocities of 3.24-3.32 km/s are found, while the P-wave velocity is 6.00 km/s (from CRUST 2.0) (Tables 3-5). As was noted for the other three regions, this P-wave velocity is not interpreted in terms of lithology since this value holds for all regions and is not a local determination from the FRE data. The measured S-wave velocities are consistent with known velocities for mica-quartz schist, amphibolite grade pelitic schist, mica-quartzite, and gneiss (Table 7). The average calculated Poisson ratios in this lowermost layer of the 1-D velocity models range from 0.276-0.290 (Tables 3-5). These Poisson ratios are calculated using the CRUST 2.0 P-wave velocity of 6.00 km/s, which is not specific to the SE region, so interpretations of these Poisson ratio values in terms of local geology cannot be made.

IX. Conclusions

The high density spatial distribution of sources and receivers deployed by WGC for the FRE yielded extensive information about the seismic structure of the upper crust in the Goldstream Valley. This information was used to generate simple refraction models of the upper 0.5+ km and 1-D and 3-D velocity models to a depth of 2 km. Overall, the models created for the shot groups with more than one source (i.e. shots 1 & 2 and shots 4 & 5) provide more consistent results than the models created using only shot 3 data. With two sources, the amount of data doubles, leading to more support for the resultant velocity measurements. In terms of the regional 1-D velocity models, the NE region appears to be the best modeled region, with synthetic waveforms that most accurately match observed data.

The high Poisson ratios, low P-wave velocities, and low Rg group velocities seen for the NW region lead to the conclusion that the lithologies of this region are characterized by poorly consolidated material, which may be the result of reworking from mining or fractured bedrock from faults in the region. The low Poisson ratios and high velocities seen for the NE region, on the other hand, indicate the presence of hard rock, such as mica-quartz schist, pelitic schist, and/or gneiss. Low Poisson ratios are also found in the N region, with values typical of gneiss, mica-quartz schist, mica-quartzite, and amphibolite grade pelitic schist.

The observed variations in P- and S-wave velocities with azimuth are shown to be the result of lateral velocity variations throughout the Goldstream Valley and not anisotropy.

The 3-D models developed in this study illustrate the variations in P- and S-wave velocity both laterally and with depth throughout this region of central Alaska. In order to improve the consistency of the amount of surface wave dispersion among the observed and synthetic waveforms generated for these models, efforts to repeat this modeling using different 1-D velocity models to create the starting block model should be completed in the future. These 1-D models should have more low velocity layers added near the surface in order to get the synthetic wave energy to spread out more and possibly reproduce the observed ringing at the tail of the recorded seismograms.

Appendix A: FRE Data

Table A1. Origin Characteristics of FRE Shots

Shot	Latitude	Longitude	Elev. (m)[1]	Date	Origin Time[2]	ANFO Wgt. (lbs)[3]	Depth (m)
1	64.94657˚	-147.69580˚	203	8/24/06	17:12:36.4	200	7
2	64.94655˚	-147.69603˚	191	8/24/06	18:24:54.66	350	7
3	64.94027˚	-147.71993˚	218	8/24/06	22:13:41.81	359	12
4	64.95389˚	-147.67982˚	353	8/26/06	21:13:28.53	200	7
5	64.95386˚	-147.67992˚	359	8/26/06	22:32:52.73	350	7

[1]Elevation recorded is that of the surface above the shot borehole
[2]Origin time based on closest available station
[3]ANFO = Ammonium Nitrate Fuel Oil

Table A2. Broadband Sensors

Station	Latitude	Longitude	Elev. (m)	Digitizer	Shots Recorded
FOX	64.95702˚	-147.61700˚	235	CMG-3T	1-5
MDR	64.99348˚	-147.73875˚	526	CMG-3T	1-5
PED	65.03315˚	-147.50205˚	795	CMG-3T	1-5
WFR	64.96564˚	-147.74331˚	391	CMG-3T	1-5
AL1	65.06530˚	-147.56440˚	404	CMG-6TD	1-5
AL2	64.94490˚	-147.86230˚	501	CMG-6TD	1-5
AL3	65.02860˚	-147.19610˚		CMG-6TD	None
AL4	64.91060˚	-147.44480˚	359	CMG-6TD	1-5
AL5	65.09930˚	-148.00430˚	436	CMG-6TD	1-5

Table A3. Broadband Recording Parameters

Parameter	WGC Value	UAF Value
Digitizer	Guralp CMG-3T	Guralp CMG-6TD
# of Channels	3	3
Resolution	24-bit	24-bit
Gain	1	
Sample Rate (per sec)	100	100
Record Mode	Continuous	Continuous

Table A4. Texan Sensors

Station	Latitude	Longitude	Elev. (m)	S/N	Shots Recorded	Regional Location
AM01	64.90609˚	-147.59180˚	284	2332	1-5	SE
AM03	64.91057˚	-147.59188˚	335	2354	1-5	SE
AM04	64.91270˚	-147.59364˚	335	2373	1-5	SE
AM05	64.91462˚	-147.59646˚	324	2323	1-5	SE
AM06	64.91626˚	-147.60014˚	313	2318	1-5	SE
AM07	64.91792˚	-147.60381˚	298	2330	1-5	SE
AM08	64.91958˚	-147.60745˚	283	2331	1-5	SE
AM09	64.92119˚	-147.61101˚	265	1978	1-5	SE
AM10	64.92301˚	-147.61502˚	246	2350	1-5	SE

Table A4. (continued)

Station	Latitude	Longitude	Elev. (m)	S/N	Shots Recorded	Regional Location
AM11	64.92452˚	-147.61899˚	239	2366	1-5	SE
AM12	64.92611˚	-147.62287˚	232	2334	1-5	SE
AM13	64.92774˚	-147.62644˚	228	2368	1-5	SE
AM14	64.92986˚	-147.63204˚	226	2353	1-5	SE
AM15	64.93138˚	-147.63660˚	222	2324	1-5	SE
AM16	64.95716˚	-147.61711˚	233	2307	1-5	NE
AM17	64.96074˚	-147.61917˚	239	2319	1-5	N
AM18	64.96256˚	-147.62270˚	243	2315	1-5	N
AM19	64.96462˚	-147.62501˚	249	2349	1-5	N
AM20	64.96687˚	-147.62653˚	260	2339	1-5	N
AM21	64.96908˚	-147.62813˚	273	2328	1-5	N
AM22	64.97123˚	-147.62966˚	278	1946	1-5	N
AM23	64.97364˚	-147.63139˚	275	2369	1-5	N
AM24	64.97582˚	-147.63340˚	279	2326	1-5	N
AM25	64.97823˚	-147.63422˚	288	2341	1-5	N
AM26	64.98032˚	-147.63557˚	293	2360	1-5	N
AM27	64.98288˚	-147.63597˚	298	2305	1-5	N
AM28	64.98482˚	-147.63556˚	305	2198	1-5	N
AM29	64.98751˚	-147.63466˚	338	2367	1-5	N
AM30	64.98967˚	-147.63302˚	348	2335	1-5	N
AM31	64.99181˚	-147.63166˚	357	2333	1-5	N
AM32	64.99435˚	-147.63157˚	378	2370	1-5	N
AM33	64.99550˚	-147.63602˚	394	2347	1-5	N
AM34	64.99706˚	-147.63993˚	406	2325	1-5	N
AM35	64.99900˚	-147.63647˚	421	2338	1-5	N
JJ01	64.95619˚	-147.61531˚	234	1955	1-5	NE
JJ02	64.95441˚	-147.61810˚	223	2343	1-5	NE
JJ03	64.95281˚	-147.62161˚	223	1968	1-5	NE
JJ04	64.95119˚	-147.62553˚	224	1944	1-5	NE
JJ05	64.94979˚	-147.62966˚	224	2290	1-5	NE
JJ06	64.94866˚	-147.63433˚	222	2271	1-5	NE
JJ07	64.94765˚	-147.63806˚	221	2316	1-5	NE
JJ08	64.94622˚	-147.64179˚	226	2306	1-5	NE
JJ09	64.93367˚	-147.64464˚	229	2356	1-5	SE
JJ10	64.93538˚	-147.64812˚	209	2359	1-5	SE
JJ11	64.93705˚	-147.65159˚	222	2378	1-5	SE
JJ12	64.93889˚	-147.65468˚	233	1965	1-5	SE
JJ13	64.94100˚	-147.65708˚	223	2355	1-5	SE
JJ14	64.94373˚	-147.65422˚	227	2345	1-5	SE
JJ15	64.94452˚	-147.65889˚	229	2357	1-5	SE
JJ16	64.94587˚	-147.66539˚	230	1970	1-5	SE
JJ17	64.94653˚	-147.67083˚	216	2090	1-5	SE
JJ18	64.94770˚	-147.67548˚	232	1947	1-5	SE
JJ19	64.94847˚	-147.68033˚	238	1963	1-5	SE
JJ20	64.94930˚	-147.68532˚	238	1987	1-5	SE
JJ21	64.95015˚	-147.69007˚	233	2344	1-5	NW
JJ22	64.95086˚	-147.69543˚	238	2302	1-5	NW
JJ23	64.95157˚	-147.70049˚	231	2289	1-5	NW
JJ24	64.95239˚	-147.70526˚	225	1979	1-5	NW

Table A4. (continued)

Station	Latitude	Longitude	Elev. (m)	S/N	Shots Recorded	Regional Location
JJ25	64.95314˚	-147.71020˚	227	2376	1-5	NW
JJ26	64.95405˚	-147.71525˚	241	1932	1-5	NW
JJ27	64.95484˚	-147.72042˚	257	2297	1-5	NW
JJ28	64.95563˚	-147.72595˚	268	2291	1-5	NW
JJ29	64.95614˚	-147.73140˚	274	2273	1-5	NW
JJ30	64.95623˚	-147.73662˚	283	2342	1-5	NW
JJ31	64.95628˚	-147.74190˚	294	1984	1-5	NW
JJ32	64.95814˚	-147.74526˚	312	2295	1-5	NW
JJ33	64.96069˚	-147.74500˚	332	1960	1-5	NW
JJ34	64.96263˚	-147.74521˚	347	2304	1-5	NW
JJ35A	64.94555˚	-147.69120˚	218	2294	1-2	NW,SE
JJ35B	64.94065˚	-147.72022˚	216	2294	3	NW,SE
JJ35C	Moved with camera			2294	4-5	NW,SE
WM01	64.96087˚	-147.61260˚	235	1949	1-5	NE
WM02	64.96240˚	-147.60861˚	240	1958	1-5	NE
WM03	64.96398˚	-147.60480˚	243	1962	1-5	NE
WM04	64.96490˚	-147.59985˚	246	2311	1-5	NE
WM05	64.96572˚	-147.59482˚	249	2382	1-5	NE
WM06	64.96656˚	-147.58990˚	254	2379	1-5	NE
WM07	64.96745˚	-147.58505˚	252	2386	1-5	NE
WM08	64.96824˚	-147.58002˚	252	2375	1-5	NE
WM09	64.96907˚	-147.57485˚	257	2299	1-5	NE
WM10	64.97001˚	-147.56994˚	260	2236	1-5	NE
WM11	64.97086˚	-147.56500˚	262	2389	1-5	NE
WM12	64.97194˚	-147.56027˚	270	2156	1-5	NE
WM13	64.97335˚	-147.55621˚	270	2177	1-5	NE
WM14	64.97470˚	-147.55176˚	271	2381	1-5	NE
WM15	64.97603˚	-147.54730˚	276	2377	1-5	NE
WM16	64.97774˚	-147.54350˚	281	2301	1-5	NE
WM17	64.97975˚	-147.54124˚	284	2336	1-5	NE
WM18	64.98194˚	-147.53999˚	287	2329	1-5	NE
WM19	64.98407˚	-147.53804˚	294	2385	1-5	NE
WM20	64.98626˚	-147.53663˚	298	2388	1-5	NE
WM21	64.98838˚	-147.53494˚	306	2383	1-5	NE
WM22	64.99054˚	-147.53346˚	310	2380	1-5	NE
WM23	64.99268˚	-147.53195˚	313	2387	1-5	NE
WM24	64.99477˚	-147.53034˚	315	2210	1-5	NE
WM25	64.99694˚	-147.52880˚	315	2200	1-5	NE
WM26	64.99895˚	-147.52635˚	319	2216	1-5	NE
WM27	65.00080˚	-147.52327˚	324	2224	1-5	NE
WM28	65.00257˚	-147.52012˚	331	2272	1-5	NE
WM29	65.00428˚	-147.51664˚	335	2242	1-5	NE
WM30	65.00573˚	-147.51259˚	337	2266	1-5	NE
WM31	65.00695˚	-147.50811˚	341	2281	1-5	NE
WM32	65.00810˚	-147.50351˚	345	2280	1-5	NE
WM33	65.00922˚	-147.49902˚	348	2278	1-5	NE

Table A5. Texan Recording Parameters

Parameter	Value
Digitizer	Reftek 125
# of Channels	1 – vertical
Resolution	24-bit
Gain	1
Sample Rate (per sec)	100
Record Mode	Time Windows
Window 1 (UTC)	2006:235:16:00 to 2006:236:01:00
Window 2 (UTC)	2006:236:16:00 to 2006:237:01:00
Window 3 (UTC)	2006:237:16:00 to 2006:238:01:00
Window 4 (UTC)	2006:238:16:00 to 2006:239:01:00
Sensor	Mark Product 4.5 Hz vertical 4" spike

Table A6. Near Source Sensors

Station	Latitude	Longitude	Elev. (m)	Ch. 1-3	Ch. 4-6	Shots Recorded
GS1	64.95124˚	-147.69367˚	238	Terra Tek[1]	L4-3D[2]	1-5
GS2	64.95449˚	-147.67783˚	366	Terra Tek	L4-3D	1-5
GS3	64.93761˚	-147.69794˚	257	Terra Tek	L4-3D	1-5
GS4	64.93853˚	-147.67283˚	210	Terra Tek	L4-3D	1-5
GS5	64.94762˚	-147.69019˚	229	Terra Tek	L4-3D	1-5
GS6	64.93891˚	-147.72799˚	215	Terra Tek	L4-3D	1-5
GS7	64.94535˚	-147.69566˚	208	Endevco[1]		1-2
GS7-shot 3	64.94035˚	-147.72032˚	207	Endevco		3
GS8A	64.94637˚	-147.69619˚	215	Endevco		1-2
GS8B	64.94627˚	-147.69577˚	211		Endevco	1-2
GS8A-shot 3	64.94025˚	-147.71964˚	207	Endevco		3
GS8B-shot 3	64.94026˚	-147.71939˚	215		Endevco	3
GS9A	64.95406˚	-147.67955˚	354	Endevco		4-6
GS9B	64.95394˚	-147.67947˚	351		Endevco	4-6

[1]Accelerometer
[2]Seismometer

Table A7. Near Source Recording Parameters

Parameter	Value
Digitizer	Reftek 72A-08
# of Channels	3 or 6
Resolution	24-bit
Gain	1
Sample Rate (per sec)	250
Record Mode	Continuous

Appendix B: Supplemental Data

Table B1. Two Layer Velocity Models from Refraction Analysis

Shots 1 & 2

Layer	NW			SE			NE			N		
	Depth to Top, km	α, km/s	β, km/s	Depth to Top, km	α, km/s	β, km/s	Depth to Top, km	α, km/s	β, km/s	Depth to Top, km	α, km/s	β, km/s
1	0	2.92	--	0	2.92	--	0	3.82	--	0	3.82	--
2	0.08	4.18	2.54	0.1	4.77	3.77	0.3	5.57	3.11	0.09	4.66	2.44

Shot 3

Layer	NW			SE			NE			N		
	Depth to Top, km	α, km/s	β, km/s	Depth to Top, km	α, km/s	β, km/s	Depth to Top, km	α, km/s	β, km/s	Depth to Top, km	α, km/s	β, km/s
1	0	2.75	1.86	0	3.56	--	0	3.89	--	0	3.89	--
2	0.1	4.09	2.19	0.3	4.70	2.54	0.5	5.64	3.28	0.05	4.75	2.55

Shots 4 & 5

Layer	NW			SE			NE			N		
	Depth to Top, km	α, km/s	β, km/s	Depth to Top, km	α, km/s	β, km/s	Depth to Top, km	α, km/s	β, km/s	Depth to Top, km	α, km/s	β, km/s
1	0	3.31	--	0	3.31	--	0	3.67	--	0	3.60	--
2	0.2	4.17	2.67	0.3	4.92	2.77	0.3	5.47	2.98	0.1	4.55	2.31

Table B2. P-wave Time-term Results

Station	Time-term, sec	Residual, sec	# Meas.	Station	Time-term, sec	Residual, sec	# Meas.
AM01	0.196	0.013	0	JJ02	0.047	0.039	3
AM03	0.183	0.007	2	JJ03	0.053	0.032	3
AM04	0.171	0.025	3	JJ04	0.065	0.027	3
AM05	0.15	0.02	3	JJ05	0.077	0.03	2
AM06	0.125	0.018	3	JJ06	0.081	0.024	2
AM07	0.125	0.026	3	JJ10	0.111	0.034	2
AM08	0.106	0.012	3	JJ11	0.099	0.028	3
AM10	0.16	0.018	3	JJ31	0.136	0.007	2
AM11	0.145	0.02	2	JJ32	0.129	0.019	3
AM12	0.143	0.027	3	JJ33	0.135	0.007	3
AM13	0.158	0.019	3	JJ34	0.137	0.015	3
AM14	0.154	0.015	2	WM01	0.032	0.011	3

Table B2. (continued)

Station	Time-term, sec	Residual, sec	# Meas.	Station	Time-term, sec	Residual, sec	# Meas.
AM15	0.142	0.042	2	WM02	0.011	0.025	3
AM16	0.063	0.02	3	WM03	0.042	0.011	2
AM17	0.042	0.033	2	WM04	0.053	0.017	3
AM18	0.032	0.02	3	WM05	0.043	0.025	2
AM19	0.039	0.025	3	WM06	0.067	0.019	3
AM20	0.029	0.024	3	WM07	0.02	0.031	3
AM21	0.037	0.021	2	WM08	0.025	0.005	2
AM22	0.039	0.021	3	WM12	0.049	0.007	2
AM23	0.057	0.002	2	WM13	0.032	0.005	2
AM24	0.05	0.014	2	WM15	0.029	0.065	2
AM25	0.047	0.014	3	WM16	0.04	0.02	2
AM26	0.034	0.001	2	WM17	0.018	0.008	2
AM27	0.074	0.003	2	WM19	0.024	0.01	2
AM28	0.07	0.018	2	WM21	0.02	0.024	2
AM29	0.064	0.014	2	WM22	0.019	0.028	3
AM30	0.082	0.015	3	WM23	0.034	0.013	3
AM31	0.079	0.01	3	WM24	0.033	0.009	2
AM32	0.074	0.011	3	WM25	0.031	0.033	2
AM33	0.081	0.01	3	WM30	0.03	0.031	2
AM34	0.129	0.019	2	WM31	0.03	0.025	2
AM35	0.067	0.015	3	WM32	0.023	0.03	2
JJ01	0.041	0.067	2	WM33	0.013	0.038	2

Table B3. S-wave Time-term Results

Station	Time-term, sec	Residual, sec	# Meas.	Station	Time-term, sec	Residual, sec	# Meas.
AM01	0.241	0.427	1	JJ02	0.112	0.168	3
AM03	0.359	0.348	2	JJ03	0.077	0.096	3
AM04	0.165	0.28	3	JJ04	0.112	0.103	3
AM05	0.128	0.316	2	JJ05	0.158	0.122	2
AM06	0.069	0.186	3	JJ06	0.143	0.158	2
AM07	0.096	0.083	2	JJ10	0.197	0.143	2
AM08	0.13	0.064	3	JJ11	0.162	0.057	3
AM10	0.188	0.159	3	JJ31	0.133	0.048	2
AM11	0.105	0.188	2	JJ32	0.133	0.096	3
AM12	0.099	0.093	3	JJ33	0.082	0.047	3
AM13	0.125	0.099	3	JJ34	0.184	0.045	3
AM15	0.15	0.125	2	WM01	0.072	0.109	3
AM16	0.181	0.06	3	WM02	0.146	0.048	3
AM17	0.162	0.006	2	WM03	0.12	0.037	2
AM18	0.079	0.166	3	WM04	0.052	0.24	2
AM19	0.099	0.122	3	WM05	0.086	0.071	2
AM20	0.178	0.132	3	WM06	0.081	0.041	3

Table B3. (continued)

Station	Time-term, sec	Residual, sec	# Meas.	Station	Time-term, sec	Residual, sec	# Meas.
AM21	0.168	0.18	2	WM07	0.147	0.062	3
AM22	0.131	0.224	3	WM08	0.142	0.162	2
AM23	0.189	0.263	2	WM13	0.222	0.142	2
AM24	0.199	0.189	2	WM15	0.058	0.443	2
AM25	0.093	0.265	3	WM16	0.137	0.093	2
AM26	0.109	0.186	2	WM17	0.122	0.137	2
AM27	0.178	0.109	2	WM19	0.143	0.122	2
AM28	0.146	0.026	2	WM21	0.136	0.18	2
AM29	0.177	0.292	2	WM22	0.208	0.26	3
AM30	0.176	0.118	3	WM23	0.183	0.417	3
AM31	0.188	0.076	3	WM24	0.225	0.365	2
AM32	0.075	0.231	3	WM25	0.253	0.45	2
AM33	0.112	0.062	3	WM30	0.253	0.506	2
AM34	0.206	0.112	2	WM31	0.302	0.506	2
AM35	0.154	0.199	3	WM32	0.367	0.605	2
JJ01	0.095	0.111	2	WM33	0.427	0.734	2

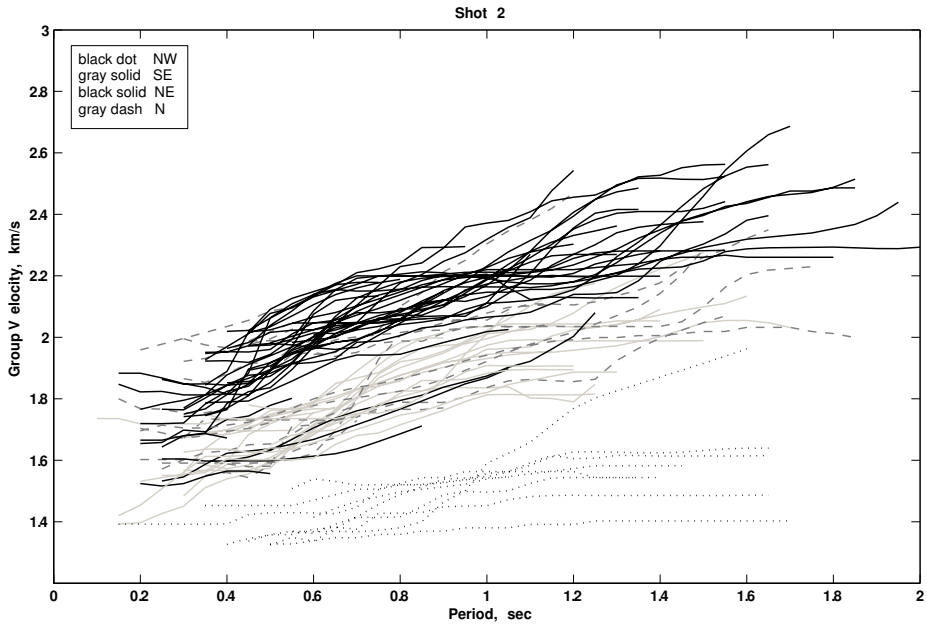

Figure B1. Rg dispersion curves for shot 2. Results are shown by region: NW (black dotted lines), SE (gray solid lines), NE (black solid lines), and N (gray dashed lines). The fastest group velocities are found for the NE data, while the slowest group velocities are seen in the NW data.

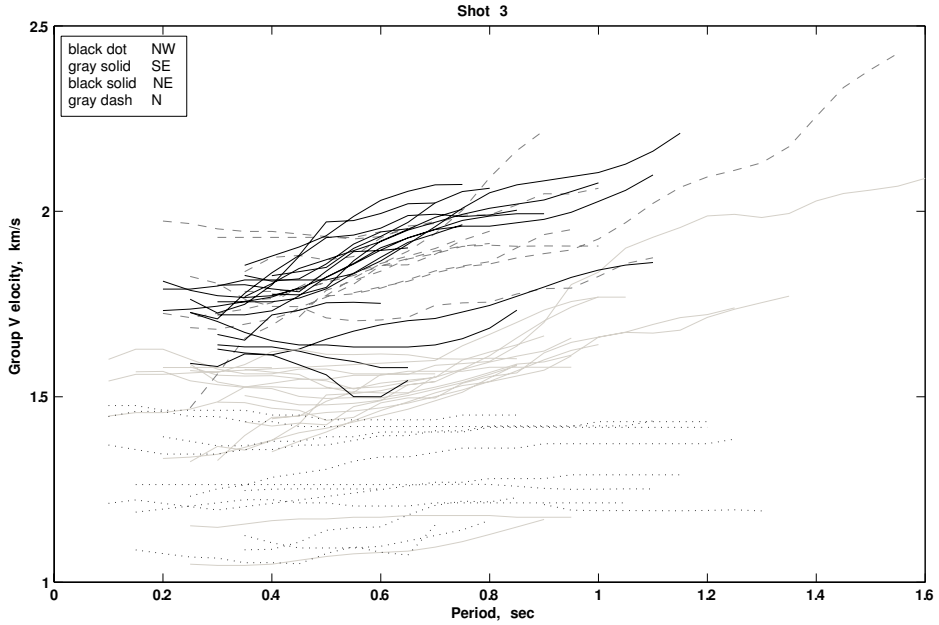

Figure B2. Rg dispersion curves for shot 3. Results are shown by region: NW (black dotted lines), SE (gray solid lines), NE (black solid lines), and N (gray dashed lines). The fastest group velocities are found for the NE and N data, while the slowest group velocities are seen in the NW data.

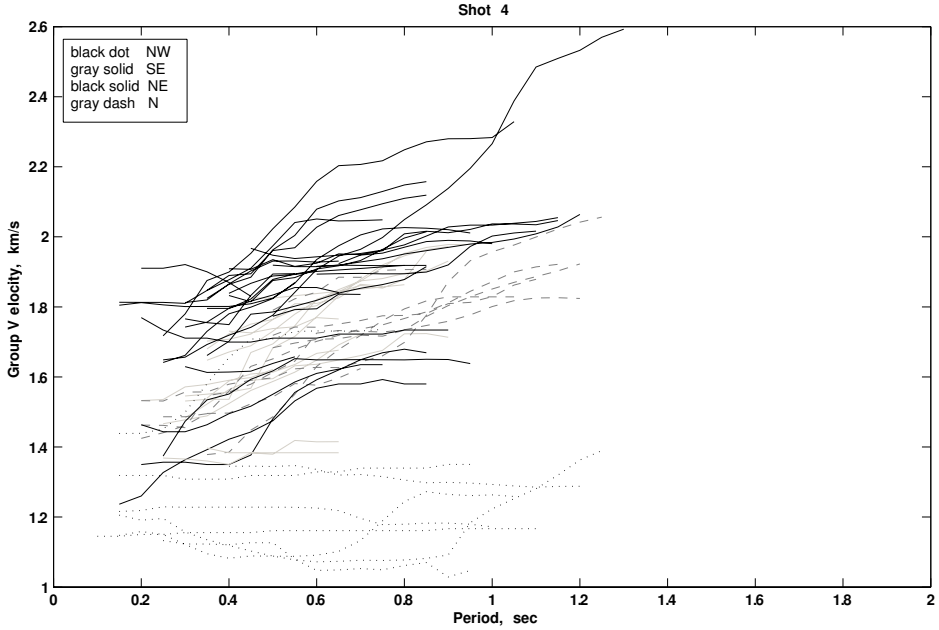

Figure B3. Rg dispersion curves for shot 4. Results are shown by region: NW (black dotted lines), SE (gray solid lines), NE (black solid lines), and N (gray dashed lines). The fastest group velocities are found for the NE data, while the slowest group velocities are seen in the NW data.

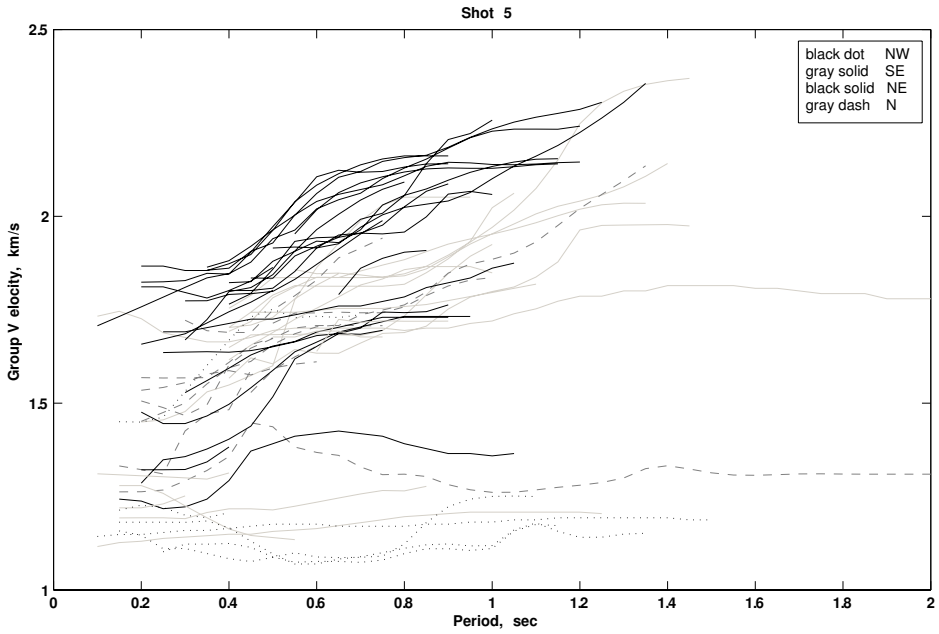

Figure B4. Rg dispersion curves for shot 5. Results are shown by region: NW (black dotted lines), SE (gray solid lines), NE (black solid lines), and N (gray dashed lines). The fastest group velocities are found for the NE data, while the slowest group velocities are seen in the NW data.

Table B4. Inversion Starting Model for Shots 1 & 2

Depth to Top (km)	Layer thickness (km)	α (km/s)	β (km/s)[1]	ρ (g/cm^3)[2]
0	0.1	2.98	1.72[1]	2.36[2]
0.1	0.1	3.92	2.27	2.53
0.2	0.1	3.92	2.27	2.53
0.3	0.1	3.92	2.27	2.53
0.4	0.1	5.16	2.98	2.71
0.5	0.2	5.16	2.98	2.71
0.7	0.2	5.16	2.98	2.71
0.9	0.2	6.00[3]	3.47	2.82
1.1	0.5	6.00	3.47	2.82
1.6	0.5	6.00	3.47	2.82
2.1	0.5	6.00	3.47	2.82
2.6	0.5	6.00	3.47	2.82
3.1	1	6.00	3.47	2.82
4.1	1	6.00	3.47	2.82
5.1	1	6.00	3.47	2.82
6.1	1	6.00	3.47	2.82
7.1	1	6.00	3.47	2.82
8.1	1	6.00	3.47	2.82
9.1	1	6.00	3.47	2.82
10.1	10.9	6.60	3.82	2.88
21	12	7.20	4.16	2.95
32	0	8.00	4.62	3.03

Table B4. (continued)

[1]S-wave velocities calculated from P-wave velocities using $V_P/V_S = 1.73$.
[2]Density calculated using Gardner's Rule: $\rho = 0.32\alpha^{.25}$, where α is in m/s (*Gardner et al.,* 1974).
[3]P-wave velocities from this point down are taken from CRUST2.0 (*Laske et al.,* 2001).

Table B5. Inversion Starting Model for Shot 3

Depth to Top (km)	Layer thickness (km)	α (km/s)	β (km/s)[1]	ρ (g/cm^3)[2]
0	0.1	3.10	1.79	2.39
0.1	0.1	3.89	2.25	2.53
0.2	0.1	3.89	2.25	2.53
0.3	0.1	3.89	2.25	2.53
0.4	0.1	5.09	2.94	2.70
0.5	0.2	5.09	2.94	2.70
0.7	0.2	5.09	2.94	2.70
0.9	0.2	6.00[3]	3.47	2.82
1.1	0.5	6.00	3.47	2.82
1.6	0.5	6.00	3.47	2.82
2.1	0.5	6.00	3.47	2.82
2.6	0.5	6.00	3.47	2.82
3.1	1	6.00	3.47	2.82
4.1	1	6.00	3.47	2.82
5.1	1	6.00	3.47	2.82
6.1	1	6.00	3.47	2.82
7.1	1	6.00	3.47	2.82
8.1	1	6.00	3.47	2.82
9.1	1	6.00	3.47	2.82
10.1	10.9	6.60	3.82	2.88
21	12	7.20	4.16	2.95
32	0	8.00	4.62	3.03

[1]S-wave velocities calculated from P-wave velocities using $V_P/V_S = 1.73$.
[2]Density calculated using Gardner's Rule: $\rho = 0.32\alpha^{.25}$, where α is in m/s (*Gardner et al.,* 1974).
[3]P-wave velocities from this point down are taken from CRUST2.0 (*Laske et al.,* 2001).

Table B6. Inversion Starting Model for Shots 4 & 5

Depth to Top (km)	Layer thickness (km)	α (km/s)	β (km/s)[1]	ρ (g/cm^3)[2]
0	0.1	2.75	1.59	2.32
0.1	0.1	3.81	2.20	2.51
0.2	0.1	3.81	2.20	2.51
0.3	0.1	3.81	2.20	2.51
0.4	0.1	3.81	2.20	2.51
0.5	0.2	5.08	2.94	2.70
0.7	0.2	5.08	2.94	2.70
0.9	0.2	5.08	2.94	2.70
1.1	0.5	6.00[3]	3.47	2.82
1.6	0.5	6.00	3.47	2.82

Table B6. (continued)

Depth to Top (km)	Layer thickness (km)	α (km/s)	β (km/s)[1]	ρ (g/cm^3)[2]
2.1	0.5	6.00	3.47	2.82
2.6	0.5	6.00	3.47	2.82
3.1	1	6.00	3.47	2.82
4.1	1	6.00	3.47	2.82
5.1	1	6.00	3.47	2.82
6.1	1	6.00	3.47	2.82
7.1	1	6.00	3.47	2.82
8.1	1	6.00	3.47	2.82
9.1	1	6.00	3.47	2.82
10.1	10.9	6.60	3.82	2.88
21	12	7.20	4.16	2.95
32	0	8.00	4.62	3.03

[1]S-wave velocities calculated from P-wave velocities using $V_P/V_S = 1.73$.
[2]Density calculated using Gardner's Rule: $\rho = 0.32\alpha^{25}$, where α is in m/s (*Gardner et al.,* 1974).
[3]P-wave velocities from this point down are taken from CRUST2.0 (*Laske et al.,* 2001).

Table B7. WPP Starting Model for Shot 2

Base (all regions)

Depth to Top, m	α, m/s	β, m/s	ρ, kg/m^3
0	3028	1592	2374
60	3908	2211	2530
330	5010	2722	2692
1000	6000	3519	2816
10020	Bottom of model		

NW Region

Depth to Top, m	α, m/s	β, m/s	ρ, kg/m^3
0	2920	1181	2352
58	3980	1944	2542
406	5010	2291	2692
1100	6000	3559	2816
10020	Bottom of model		

SE Region

Depth to Top, m	α, m/s	β, m/s	ρ, kg/m^3
0	2920	1555	2352
36	4030	2117	2550
318	4910	2778	2679
1100	6000	3539	2816
10020	Bottom of model		

NE Region

Depth to Top, m	α, m/s	β, m/s	ρ, kg/m^3
0	3090	1815	2386
50	3760	2430	2506
279	5570	2954	2764
900	6000	3488	2816
10020	Bottom of model		

N Region

Depth to Top, m	α, m/s	β, m/s	ρ, kg/m^3
0	3180	1816	2403
96	3860	2355	2522
318	4550	2864	2628
900	6000	3490	2816
10020	Bottom of model		

Table B8. WPP Starting Model for Shot 3

Base (all regions)

Depth to Top, m	α, m/s	β, m/s	ρ, kg/m^3
0	2985	1644	2365
60	3865	2136	2523
337	5028	2659	2695
1000	6000	3513	2816
10020	Bottom of model		

NW Region

Depth to Top, m	α, m/s	β, m/s	ρ, kg/m^3
0	2750	1388	2317
59	3810	1716	2514
431	5080	2559	2702
1100	6000	3559	2816
10020	Bottom of model		

SE Region

Depth to Top, m	α, m/s	β, m/s	ρ, kg/m^3
0	2920	1578	2352
36	4030	1967	2550
318	4910	2640	2679
1100	6000	3528	2816
10020	Bottom of model		

NE Region

Depth to Top, m	α, m/s	β, m/s	ρ, kg/m^3
0	3090	1856	2386
50	3760	2432	2506
279	5570	2748	2764
900	6000	3488	2816
10020	Bottom of model		

N Region

Depth to Top, m	α, m/s	β, m/s	ρ, kg/m^3
0	3180	1753	2403
96	3860	2429	2522
318	4550	2691	2628
900	6000	3476	2816
10020	Bottom of model		

Table B9. WPP Starting Model for Shot 5

Base (all regions)

Depth to Top, m	α, m/s	β, m/s	ρ, kg/m^3
0	3145	1648	2396
107	3928	2013	2533
384	5073	2644	2701
1000	6000	3530	2816
10020	Bottom of model		

NW Region

Depth to Top, m	α, m/s	β, m/s	ρ, kg/m^3
0	2920	1333	2352
58	3980	1783	2542
406	5010	2374	2692
1100	6000	3600	2816
10020	Bottom of model		

SE Region

Depth to Top, m	α, m/s	β, m/s	ρ, kg/m^3
0	3310	1808	2427
206	4190	2363	2575
493	5220	2943	2720
1100	6000	3533	2816
10020	Bottom of model		

Table B9. (continued)

NE Region				N Region			
Depth to Top, m	α, m/s	β, m/s	ρ, kg/m^3	Depth to Top, m	α, m/s	β, m/s	ρ, kg/m^3
0	3170	1804	2401	0	3180	1648	2403
69	3680	2251	2492	96	3860	2007	2522
319	5510	2843	2757	318	4550	2716	2628
900	6000	3498	2816	900	6000	3487	2816
10020	Bottom of model			10020	Bottom of model		

References

Appelö, D., N. A. Petersson, B. Sjögreen, K. McCandless, and A. J. Rodgers, User's guide to the Wave Propagation Program (WPP) version 1.1, *Lawrence Livermore National Laboratory*, Technical Report SM-230257, 2007.

Beghoul, N. and M. Barazangi, Azimuthal anisotropy of velocity in the mantle lid beneath the Basin and Range province, *Nature*, **348**, 536-538, 1990.

Berry, M. J., and G. F. West, An interpretation of the first-arrival data of the Lake Superior experiment by the time-term method, *Bulletin of the Seismological Society of America*, **56** (1), 141-171, 1966.

Birch, F., The velocity of compressional waves in rocks to 10 kilobars, Part 1, *Journal of Geophysical Research*, **65** (4), 1083-1102, 1960.

Bonner, J. and M. Leidig, Development of an upper crustal attenuation model for the Goldstream Valley region of central Alaska: Quicklook report, Weston Geophysical Corporation (unpublished), 4 July 2007.

Bonner, J. L., R. J. Martin, III, and M. Leidig, Possible effects of frozen rock on explosive coupling, Quarterly scientific report no. 11, prepared for Air Force Research Laboratory, reporting period 28 January 2007-28 April 2007.

Brocher, T. M., G. S. Fuis, W. J. Lutter, N. I. Christensen, and N. A. Ratchkovski, Seismic velocity models for the Denali fault zone along the Richardson highway, Alaska, *Bulletin of the Seismological Society of America*, **94** (6B), S85-S106, 2004.

Brocher, T. M., W. J. Nokleberg, N. I. Christensen, W. J. Lutter, E. L. Geist, M. A. Fisher, Seismic reflection/refraction mapping of faulting and regional dips in the eastern Alaska Range, *Journal of Geophysical Research*, **96** (B6), 10233-10249, 1991.

Christensen, N. I., Poisson's ratio and crustal seismology, *Journal of Geophysical Research,* **101** (B2), 3139-3156, 1996.

Christensen, N. I., Shear wave velocities in metamorphic rocks at pressures to 10 kilobars, *Journal of Geophysical Research*, **71** (14), 3549-3556, 1966.

Christensen, N. I., Compressional wave velocities in metamorphic rocks at pressures to 10 kilobars, *Journal of Geophysical Research,* **70** (24), 6147-6164, 1965.

Christensen, N. I. and W. D. Mooney, Seismic velocity structure and composition of the continental crust: A global view, *Journal of Geophysical Research*, **100** (B7), 9761-9788, 1995.

Combellick, R. A. and T. K. Bundtzen, Preliminary derivative geologic-materials map of the Fairbanks Mining District, Alaska, *Alaska Division of Geological and Geophysical Surveys*, Public Data File 96-17, 1996.

Dziewonski, A., S. Bloch, and M. Landisman, A technique for the analysis of transient seismic signals, *Bulletin of the Seismological Society of America*, **59** (1), 427-444, 1969.

Foster, H. L., T. E. C. Keith, W. D. Menzie, Geology of the Yukon-Tanana area of east central Alaska, in G. Plafker and H. C. Berg, eds., *The Geology of North America vol. G-1, The Geology of Alaska,* Boulder, Colorado: The Geological Society of America, 205-240, 1994.

Fuis, G. S., E. L. Ambos, W. D. Mooney, N. I. Christensen, and E. Geist, Crustal structure of accreted terranes in southern Alaska, Chugach Mountains and Copper River Basin, from seismic refraction results, *Journal of Geophysical Research*, **96** (B3), 4187-4227, 1991.

Gardner, G. H. F., L. W. Gardner, and A. R. Gregory, Formation velocity and density—The diagnostic basics for stratigraphic traps, *Geophysics*, **39** (6), 770-780, 1974.

Goldstein, P., D. Dodge, M. Firpo, L. Minner, SAC2000: Signal processing and analysis tools for seismologists and engineers, Invited contribution to W. H. K. Lee, H. Kanamori, P. C. Jennings, and C. Kisslinger, eds., *The IASPEI International Handbook of Earthquake and Engineering Seismology*, London: Academic Press, 2003.

Herak, M., M. Živčić, and D. Herak, Azimuthal anisotropy of the P-wave velocity in the hypocentral volume of the Krn Mt. (Slovenia) earthquake sequence, *Journal of Applied Geophysics*, **54**, 257-264, 2003.

Herrmann, R. B., Computer programs in seismology, Version 3.30, St. Louis University, http://mnw.eas.slu.edu/People/RBHerrmann/CPS330.html, last accessed May 2007, 2004.

Holbrook, W. S., W. D. Mooney, and N. I. Christensen, The seismic velocity structure of the deep continental crust, in D. M. Fountain, R. Arculus, and R. Kay, eds., *Lower Continental Crust*, Amsterdam: Elsevier, 1-43, 1992.

Laske, G., G. Masters, and C. Reif, CRUST 2.0, Reference Earth Model web site: http://mahi.ucsd.edu/Gabi/rem.html, last accessed March 2008, 2001.

Leidig, M., J. Bonner, R. Martin, S. Dougherty, K. Murphy, Effects of frozen rock on explosive coupling, in *Proceedings of the 29th Monitoring Research Review: Ground-Based Nuclear Explosion Monitoring Technologies*, 612-621, 2007.

Leidig, M., J. L. Bonner, J. Britton, A. Ferris, J. F. Lewkowicz, V. Romanovsky, D. May, J. Reeves, W. Zamora, and M. Johnson, Explosion coupling in frozen and unfrozen rock: Quicklook Report, Weston Geophysical Corporation, prepared for Air Force Research Laboratory, 2006a.

Leidig, M., V. Romanovsky, R. Hansen, R. Martin, R. Grove, J. Bonner, and J. Lewkowicz, Possible effects of frozen rock on explosive coupling, in *Proceedings of the 28th Seismic Research Review: Ground-Based Nuclear Explosion Monitoring Technologies*, 618-624, 2006b.

Lokmer, I. and M. Herak, Anisotropy of P-wave velocity in the upper crust of the central external Dinarides, *Studia Geophysica et Geodætica*, **43**, 345-356, 1999.

Newberry, R. J., T. K. Bundtzen, K. H. Clautice, R. A. Combellick, T. Douglas, G. M. Laird, S. A. Liss, D. S. Pinney, R. R. Reifenstuhl, and D. N. Solie, Preliminary geologic map of the Fairbanks Mining District, Alaska, *Alaska Division of Geological and Geophysical Surveys*, Public Data File 96-16, 1996.

Robinson, M. S., T. E. Smith, and P. A. Metz, Bedrock geology of the Fairbanks Mining District, *Alaska Division of Geological and Geophysical Surveys*, Professional Report 106, 1990.

Sammis, C. and R. Biegel, Seismic radiation from explosions in frozen crystalline rock, in *Proceedings of the 27th Seismic Research Review: Ground-Based Nuclear Explosion Monitoring Technologies*, vol. 1, 642-652, 2005.

Sheriff, R. E. and L. P. Geldart, *Exploration Seismology*, 2nd ed., New York: Cambridge University Press, 1995.

Stein, S. and M. Wysession, *An Introduction to Seismology, Earthquakes, and Earth Structure*, Malden, MA: Blackwell Publishing, 2003.

Takanashi, M., O. Nishizawa, K. Kanagawa, and K. Yasunaga, Laboratory measurements of elastic anisotropy parameters for the exposed crustal rocks from the Hidaka Metamorphic Belt, Central Hokkaido, Japan, *Geophysical Journal International*, **145**, 33-47, 2001.

Wilson, F. H., J. H. Dover, D. C. Bradley, F. R. Weber, T. K. Bundtzen, and P. J. Haeussler, Geologic map of central (interior) Alaska: Northeastern region, *U. S. Geological Survey*, Open-file report 98-133, 1998.